uOttawa

L'Université canadienne
Canada's university

FACULTÉ DES ÉTUDES SUPÉRIEURES ET POSTOCTORALES

uOttawa

L'Université canadienne
Canada's university

FACULTY OF GRADUATE AND POSDOCTORAL STUDIES

Jin Fu

AUTEUR DE LA THÈSE / AUTHOR OF THESIS

M.A.Sc. (Mechanical Engineering)

GRADE / DEGREE

Department of Mechanical Engineering

FACULTÉ, ÉCOLE, DÉPARTEMENT / FACULTY, SCHOOL, DEPARTMENT

Development of Polymeric Foam Materials with Improved Mechanical and Acoustic Properties

TITRE DE LA THÈSE / TITLE OF THESIS

H. Naguib

DIRECTEUR (DIRECTRICE) DE LA THÈSE / THESIS SUPERVISOR

CO-DIRECTEUR (CO-DIRECTRICE) DE LA THÈSE / THESIS CO-SUPERVISOR

EXAMINATEURS (EXAMINATRICES) DE LA THÈSE / THESIS EXAMINERS

M. Dubé

M. Munro

Gary W. Slater

LE DOYEN DE LA FACULTÉ DES ÉTUDES SUPÉRIEURES ET POSTDOCTORALES /
DEAN OF THE FACULTY OF GRADUATE AND POSTDOCORAL STUDIES

Development of Polymeric Foam Materials with Improved Mechanical and Acoustic Properties

Jin Fu

A thesis submitted to the Faculty of Graduate and Postdoctoral Studies
in partial fulfillment of the requirements for the degree of

MASTER OF APPLIED SCIENCE

in Mechanical Engineering

Ottawa-Carleton Institute for Mechanical and Aerospace Engineering
University of Ottawa
Ottawa, Canada

September 2005

Your file Votre référence
ISBN: 0-494-11273-5
Our file Notre référence
ISBN: 0-494-11273-5

Abstract

This thesis addresses the processing, morphology, mechanical properties, and acoustic properties of new polymeric foam materials. A batch foaming process, a rotational mold foaming process and a constrained mold foaming process were designed and applied in the producing of polymeric foams. Microcellular closed cell polymethyl-methacrylate (PMMA) foams were produced using the batch foaming process. The foam morphologies and mechanical properties such as elastic modulus, tensile strength and elongation at break were investigated by varying the foaming parameters. The PMMA microcellular foam showed superior mechanical properties in tensile strength and elongation at break over conventional foams. Nanoclay was used as reinforcement filler and a nucleation agent for PMMA in the batch foaming process. The nanoclay affected the foaming behavior and enhanced the mechanical properties of the microcellular PMMA foams. The PMMA nanocomposite foam with 0.5 wt % nanoclay exhibited optimized mechanical properties. Fine celled Polypropylene (PP) and low density Polyethylene (LDPE) foams were also produced using the rotational mold foaming. The processing parameters such as the particle sizes and processing time were important parameters in this process. The obtained PP foam exhibited a greatly improved energy absorption capacity. Opened cell PMMA foams were produced using a particulate leaching/gas foaming method for acoustic absorption applications. The foam morphology i.e. porosity and cell sizes were independently controlled by altering the processing settings. Consequently, the acoustic performance of the foams was manipulated.

Finite element analysis was then employed to predict the macroscopic properties of polymeric foams correlated to their microstructure. The predicted elastic responses of both opened cell and closed cell foams showed great agreement with experimental results.

Acknowledgements

I would like to give my sincere thanks to my research advisor, **Dr. Hani E. Naguib**, for his encouragement and guidance to me during the entire course of this research project. Not only did he lead me into the research field of polymeric foam using his knowledge and experience, but also he provided me confidence to finish this work.

I am grateful to acknowledge the other members in our group, i.e. **Mr. Allan Manninnen, Mr. Choonghee Jo, Ms. Xiaojia Hu, Ms. Josee Peron, Mr. Andrew Edgerton, Mr. Aaron Price** and **Dr. Florent Goldberg**, for their discussion and friendship during this work.

Also, I wish to thank **Mr. John Perrins** and **Mr. Leo Denner**, from the workshop of the mechanical department in University of Ottawa, for their helping on realizing my design.

I wish to express my gratitude to AUTO21 funded by the Networks of Centers of Excellence of Canada program for supporting this research work.

Finally, I thank my family – my parents and my wife, **Yuan Dong**, for their understanding, love, and moral support.

Table of Contents

List of Tables

List of Figures

Nomenclature

Latin Letters

A	=	area
C	=	solubility
c	=	specific heat
C_0	=	concentration of gas molecules
C_0'	=	concentration of gas molecules in solution after heterogeneous nucleation
C_1	=	concentration of heterogeneous nucleation sites
D	=	diffusion coefficient
D_s	=	diameter
D_0	=	diffusion coefficient constant
E	=	Young's modulus
E_a	=	activation energy for diffusion of a gas in a polymer
F	=	force
f_0	=	frequency factor for homogeneous nucleation
f_1	=	frequency factor for homogeneous nucleation
H	=	Henry constant
h	=	convection heat transfer coefficient
I	=	moment of inertia

J = moment of inertia

k = Boltzmann's constant

K = bulk modulus

L = thickness

m = mass

N = nucleation rate

N_c = cell density

N_{het} = heterogeneous nucleation rate

N_{hom}' = modified homogeneous nucleation rate

P = pressure

P_r = power

R = gas constant

$S(\theta)$ = wetting angle geometric factor

T = temperature

t = time

T_∞ = oven temperature

t_c = width of the square cross section

T_r = torque

V = volume

Greek Letters

γ = surface energy

ΔG_{het}^{*} = change in free energy needed to create a critical heterogeneous nucleation

ΔG_{hom}^{**} = free energy required for homogeneous nucleation

ΔL = deflection

ΔP = change in gas saturation pressure

ΔU = change in potential energy

ε = strain

ρ = density

σ = stress at yield

σ = stress

Φ = fraction of solid in the cell struts

φ = expansion ratio

ω = angular velocity

Subscripts

b = bending

c = compression

f = foam

g = glass transition

m = mold

p = polymer

Chapter 1: Introduction

1.1 Foam Materials

The term *foam* discussed in this article is a sort of composite material consisting of at least two phases: solid and gas bubbles dispersed throughout the solid matrix. Foam is also referred to as a cellular solid. Sponge, wood, cork, and coral are some examples of nature's foams. Human-made foam materials such as light-weight brick, seating cushion materials, heat isolation materials, sound absorption materials, and some foods are widely used.

There are several important reasons that make foam materials so popular in both nature and the human world. The first reason is their mechanical properties. Foam materials have high stiffness-weight and strength-weight ratios. This gives foam applications in light-weight structural materials such as man-made light-weight bricks and animal bones. The second reason for its popularity is its energy absorption and management capacity. Foam absorbs impacts, vibrations, and sounds. Foams can also be used as thermal and acoustic insulation media. Car bumpers, shock absorbers, and noise control parts are usually made of foam materials. Foam absorbs not only energy, but also liquids and solids, which is the third reason for its popularity. This feature makes it useful in cleaning and drug delivery applications. The fourth reason that foam materials are so widely used is that their reduced hardness and modulus make them very desirable in the applications that require soft materials. Some other interesting properties such as increased electric capacitance and

decreased electric conductivity give foam materials many further potential applications. Of course, along with all these advantages come foam's reduced weight and material cost.

Foams are classified using several different methods. The most commonly used one is based on the cell structure of the foam. Opened cell foams are characterized as foams whose cells are interconnected with each other allowing gas to move from one cell to another. Closed cell foams, on the other hand, are foams that have an isolated cell structure. It should be noted that most foams in reality are partially opened or closed. Closed cell foams are commonly employed in structural material applications and opened cell foams are frequently used for acoustic absorption and filtering.

Foams are also classified by the cell size and cell density. Conventional foams usually have a cell size greater than 300 μm and a cell density less than 10^6 cells/cm^3. Fine celled foams have a cell size between 10 μm and 300 μm, and a cell density between 10^6 cells/cm^3 and 10^9 cells/cm^3. Microcellular foams are usually defined as foams having average cell sizes in the order of 10 μm and cell densities in the order of 10^9 to 10^{15} cells/cm^3 [1]. Microcellular foams have attracted great interest in recent decades and will be discussed in detail later.

Almost any solid material can be used to make foam. Although ceramic and metal foams are produced, polymer foams are the most widespread [2]. All the foams discussed in this study are made of polymers.

1.2 Microcellular Foams

Microcellular foam technology was first developed at the Massachusetts Institute of

Technology (MIT) in the 1980s [3]. This technology uses a high pressure, inorganic, physical blowing agent to create small gas bubbles on the order of 10 μm in size in polymer matrices. A batch gas foaming approach was developed for the microcellular foaming process based on this idea. This method was then modified into a continuous process in order to increase productivity [4, 5]. Generally, in these gas foaming processes, polymer samples are placed in a highly pressurized container with a non-reactive gas (such as carbon dioxide or nitrogen) to saturate the polymers. A pressurized container at room temperature or an extruder at high temperature may be used. After a uniform, single-phased polymer/gas solution is ready, the pressure is quickly released. The sudden jump in pressure and/or temperature caused cell nucleation and cell growth, thus resulting in foams with cell sizes in the order of micrometers [3 , 6-10].

Compared to unfoamed polymers and conventional foams, microcellular foams have better properties such as high impact strength [9, 11], high toughness [10], high stiffness-weight ratio [12], high fatigue life [13], high thermal stability [14], low dielectric constant [15], as well as reduced material weight and cost. Therefore, microcellular foams have great potential for applications such as packaging, insulation, and for structural parts and components in the automotive and aircraft industries.

Since the cell sizes of microcellular foam are small, the size of the critical flaws pre-existing in the polymers may be larger than the cell size. According to the Griffith crack hypothesis [16], as the bubbles decrease in size, the stress concentration around the bubbles also decreases. Therefore, the strength of the foamed materials will not notably diminish if the

cell sizes in the foam become very small. Greater mechanical properties with a reduced material weight can be obtained using a microcellular foaming procedure.

1.3 Polymer/Clay Nanocomposite

Polymer materials have been filled with nanometer-scaled, layered silicates in order to obtain superior mechanical properties [17-26], increased flame-retardance [27-29], reduced gas permeability [30-35], and better thermal resistance [36-38]. The effects of the filler on the composite materials depend on its size, aspect ratio, hybrid morphology, and dispersion quality. Generally, layered silicate fillers have a thickness on the order of 1 nm, along with a high aspect ratio of between 10:1 and 1000:1. Nanometer-scaled silicate pellets with such high aspect ratios tend to make a good reinforcement and improve the mechanical properties of the polymer [39].

Polymer/Clay Nanocomposites (PCNs) are of particular interest because the nanometer-scaled filler can be used as a nucleation agent in the gas foaming processes. The interfaces between the fillers and the polymer are potential nucleation sites where heterogeneous nucleation can be induced. Since the size of the filler is on the order of nanometers, the sizes of the cells nucleated by nanoclay can be very small as well, making nanoclay a very desirable filler in microcellular foam processing.

1.4 Problem Statement and Objectives

The main objective of this research is the processing and characterization of polymeric

foams with optimized mechanical properties and acoustic absorption properties. In the progress of this research, it was achieved by several short-term objectives that are described below.

Different applications require different processing technologies. The first short-term objective is to achieve processing designs for the polymeric foams that can be used in mechanical and acoustic applications. A batch foam process will be designed to investigate the correlation between the processing parameters, foam morphologies and mechanical properties of closed cell microcellular PMMA foams. A rotational mold foaming process will be designed to produce low cost polymeric foams with an enhanced energy absorption capacity. Modification is required on the batch foaming process to produce opened cell foams and to control their geometry.

In order to apply the microcellular polymer foams in industrial applications, it is of importance to link mechanical and acoustic properties to the processing parameters. A good knowledge of the micro-level foam morphology is helpful in revealing these relationships. Thus, the second of the objectives of this study is to investigate the effect of the processing parameters such as foaming time, foaming temperature, and saturation pressure on morphology and the mechanical properties. The mechanical properties of PMMA/montmorillonite clay nanocomposite, the effects of the nanoclay on the foam processing, and the mechanical properties of the nanocomposite microcellular foams produced using subcritical CO_2 gas foaming are to be studied. The results will help engineers to optimize their designs by altering the processing parameters to obtain preferred

mechanical properties for their specific applications.

The rotation mold foaming process has advantages over the batch foaming process, such as higher productivity, controlled part geometries and lower cost. However, the knowledge on making foam parts using rotational molding is still limited. The third objective of this study is thus to further investigate a foam making process using rotational molding. The foam morphology and mechanical properties of the products made by this process will also be studied.

Foams with closed cells are very poor sound absorbers because the fluid within the foam cells cannot move and dissipate energy. Opened cell structures are thus required to enhance the acoustic absorption capacity. The fourth objective of this thesis is to modify the existing process technology to produce open celled foams and to study their acoustic absorption properties.

Finally, in order to investigate the relationship between the microstructure of foams and their macroscopic properties, a computer simulation will be developed to model the mechanical behavior of foams with complex geometrical structures. This simulation will be developed using the Finite Element Method (FEM).

1.5 Organization of the Thesis

This thesis is comprised of nine chapters. In Chapter 1, a brief introduction to the foam materials and their properties is described. Chapter 2 provides a literature review and technical background to the relevant topics, such as the principle of gas foaming technology,

current existing foam processing technologies, polymer/clay nanocomposite foams, and the mechanical and acoustic properties of foams. Chapter 3 presents the design of the processes used in this study. In Chapter 4, the experimental results of processing and characterization of PMMA microcellular foams are presented. The effects of nanoclay on the foam are also discussed in this chapter. The rotational mold foaming process and the properties of the foam made using this process are studied in Chapter 5. In Chapter 6, the experimental results of processing opened cell foams and their acoustic properties are reported. In Chapter 7, finite element analysis is used to predict the elastic response of polymeric foams. Chapter 8 summarizes the conclusions throughout this study and Chapter 9 provides recommendations for future works. The calculation of material charge and the detailed mechanical drawings of the rotational mold foaming process are provided in Appendices.

Chapter 2: Background and Literature Survey

2.1 Introduction

In this chapter, a literature review and technical background on the processing and characterization of polymeric foam is provided. The subjects included in this chapter are: the principle of gas foaming technology, current research progress of existing foam processing technologies such as batch foaming process and rotational mold foaming process, polymer/clay nanocomposite foam, and the mechanical and acoustic properties of polymeric foams.

2.2 Principle of Gas Foaming Technology

Generally, there are several important steps during the gas foaming process: Formation of gas/polymer solution, cell nucleation, cell growth, and cell stabilization [4, 5]. The following sections describe each step in detail.

2.2.1 Formation of gas/polymer solution

Formation of gas/polymer solution is a fundamental step of the gas foaming process. A polymer is able to absorb non-reactive gas, such as CO_2 and N_2. In foam processing, these gases are called physical blowing agents (PBA). The gas absorption behavior can be

described by two parameters: solubility and diffusivity. Solubility denotes the maximum concentration of the gas in the polymer. The solubility can be described by Henry's law:

$$C = H \cdot P \tag{2.1}$$

where P is pressure, C is solubility of the gas in the polymer and H is the Henry constant, which is dependant on the temperature. While diffusivity denotes how fast the gas can enter or disperse out of the polymer. The diffusivity can be described by an Arrhenius relationship that is given by:

$$D = D_0 \exp\left(-E_a / RT\right) \tag{2.2}$$

where D is the diffusivity, D_0 is the diffusion coefficient constant, E_a is the activation energy for diffusion of a gas in a polymer, R is the gas constant, and T is the absolute temperature. Generally, a higher solubility of gas in a polymer is more ideal for foaming because there is more gas available for cell nucleation and growth. A higher diffusivity is sought in this step because of a shorten saturation time and better productivity. However, it may not be good for cell growth, which will be discussed later.

Based on the equations above, one can see that both the solubility and diffusivity are highly dependant on the pressure and temperature. A lower temperature generally results in a higher solubility, which is desirable. However, a decreased temperature decreases the diffusivity of gas in polymer, which thereby reduces the productivity. In order to improve the productivity, higher gas pressure gas is commonly used to increase the diffusivity.

Recently it was reported that other factors can also affect the gas solubility and diffusivity in polymer. A. Manninen et al. [40] studied the effect of nanoclay on the kinetics

of CO_2 gas in PMMA. It was found that diffusivity increased with a higher nanoclay concentration while the solubility remained unchanged by the presence of nanoclay. Handa et al. [51, 52] reported that the diffusivity of highly pressurized CO_2 in PMMA at a lower temperature may be higher than that at a higher temperature because of the shifting of the glass transition temperature (T_g). The change in crystallinity of a semi-crystalline polymer was also found to change the solubility of gas in a polymer [41].

2.2.2 Cell Nucleation

After a gas/polymer solution has been prepared, the pressure is dropped and/or the temperature increased dramatically. The solubility consequently decreases according to Henry's law. The resulting thermodynamic instability induces large number of cell nucleations because the gas tends to escape out of the polymer matrix. Cell nucleation is of great importance in the foaming process because it determines the morphology of the final foam product.

Classic nucleation theory is commonly used to explain the cell nucleation of gas foaming [6, 7, 42]. This theory classifies the cell nucleation into two different types: homogeneous nucleation and heterogeneous nucleation. Homogeneous nucleation occurs when there are no other objects in the one phase gas/polymer solution to cause nucleation. The homogeneous nucleation rate is given by:

$$N_{hom} = f_0 C_0 \exp\left(-\Delta G_{hom}^{**} / kT\right) \tag{2.3}$$

where f_0 is the frequency factor for homogeneous nucleation; C_0 is the concentration of gas

molecules; ΔG_{hom}^{**} is the free energy required for homogeneous nucleation; k is Boltzmann's constant; T is the temperature in Kelvin. ΔG_{hom}^{**} is given by:

$$\Delta G_{hom}^{**} = \frac{16\pi}{3\Delta P^2}\gamma^3 - \Delta U \tag{2.4}$$

where γ is the surface energy of the polymer; ΔP is gas saturation pressure; and ΔU is the change in potential energy of the system.

Heterogeneous nucleation occurs at the interfaces between the polymer/gas solution and another phase, such as a solid additive. The heterogeneous nucleation rate is given by:

$$N_{het} = f_1 C_1 \exp\left(-\Delta G_{het}^{*} / kT\right) \tag{2.5}$$

where f_1 is the frequency factor for homogeneous nucleation; C_1 is the concentration of heterogeneous nucleation sites; ΔG_{het}* is the change in free energy required to create a critical heterogeneous nucleation; k is Boltzmann's constant; and T is the temperature in Kelvin. The term ΔG_{het}^{*} is given by:

$$\Delta G_{het}^{*} = \frac{16\pi}{3\Delta P^2}\gamma^3 S(\theta) \tag{2.6}$$

where γ is the surface energy of the polymer; ΔP is gas saturation pressure; and $S(\theta)$ is wetting angle geometric factor.

The homogeneous nucleation and the heterogeneous nucleation are not exclusive to each other. The mixed model describes the nucleation rate by:

$$N = N_{hom}^{'} + N_{het} \tag{2.7}$$

where N is the nucleation rate of both two nucleation; $N_{hom}^{'}$ is the modified homogeneous nucleation rate; and N_{het} is the heterogeneous nucleation rate. Modified homogeneous nucleation rate $N_{hom}^{'}$ can be given by:

$$N'_{hom} = f_0 C'_0 \exp\left(-\Delta G^{**}_{hom} / kT\right) \tag{2.8}$$

where C_0' is the concentration of gas molecules in solution after heterogeneous nucleation has occurred.

The free energy required to create heterogeneous nucleation is generally much lower than the free energy required for homogeneous nucleation. Therefore, additives such as talc or nanoclay can decrease the energy required to create bubbles and therefore promote the cell nucleation.

2.2.3 Cell Growth

Once nucleation has occurred, either homogeneous or heterogeneous, the difference between the gas pressures inside and outside the bubble drives bubble growth. Young and Suh [43] proposed a basic model to describe the cell growth during the process of gas foaming. Ramesh [44] presented a numerical and experimental study of cell growth in microcellular foaming process by modifying an existing single cell model. More models were derived for cell growth in viscous Newtonian fluids [45, 46], and in viscoelastic fluids [46-48]. The cell growth rate mostly depends on the following issues: the diffusivity of the blowing gas, pressure of the polymer melt, the concentration of dissolved blowing gas in the melt polymer, the cell size, the permeation rate of the blowing agent through the polymer phase, and the melt strength and elasticity of the surrounding molten polymer [12]. Cell nucleation and cell growth consumes some of the gas dissolved in the polymer matrix; the rest of the gas is diffused to the environment. By carefully selecting the processing

conditions such temperature, pressures and time, the cell growth can be manipulated.

2.2.4 Cell Stabilization

As the cells grow, they become more and more close to each other. A cell wall is the solid polymer between two gas bubbles. The cell walls are stretched thinner and thinner, as a result of the pressure inside the bubbles driving cell growth. When the pressure is high enough to rupture the cell wall, the two adjacent bubbles becomes a single larger bubble. This transformation is referred to as *cell coalescence* [67]. As described above, cell coalescence coarsens the average cell sizes. However, a finer cell structure is generally required for better mechanical properties and thermal isolation properties, therefore, cell coalescence should be avoided. Decreasing the flexibility of the polymer by cooling down the polymer is a common way to prevent cell coalescence. When the temperature drops below the glass transition temperature (T_g) or the crystallization temperature (T_c), the foam morphology is fixed. For the cases which require rapid temperature drop, water cooling is used; otherwise, air cooling is applied.

2.3 Review of Foam Processing Technologies

2.3.1 Batch Foaming

A two-stage batch approach was developed for the microcellular foaming process [6-10, 42, 49]. In the first stage, polymer samples are placed in a high pressure container with a non-reactive gas (such as CO_2 or N_2) at room temperature to saturate the polymer samples. In

the second stage, the pressure is released and the samples are then quickly heated to a temperature high enough to soften the polymer. The sudden jump in temperature causes cell nucleation and growth which produces foam with cell sizes on the order of micrometers.

Based on the aforementioned work, some improvements were investigated recently. Supercritical carbon dioxide ($scCO_2$) was used as a blowing agent to process microcellular PMMA foam. This method makes use of the dropping of glass transition temperature of polymers in high pressure CO_2 [50]. A low temperature foam process was developed to produce PMMA foams with ultra low cell size and high cell density taking advantage of the retrograde vitrification in the PMMA-CO_2 system [51, 52].

Since the microcellular foaming technology was introduced, it has been applied to a lot of different polymers. For example, amorphous polymers such as polystyrene (PS) [7, 53-56], PMMA [50, 57, 58], polycarbonate (PC) [1] and so on were successfully used to produce microcellular foams. Recently, some semi-crystalline polymers such as poly(ethylene terephthalate) (PET) [59-61], polypropylene (PP) [62] polybutylene (PB) and PE [63] were converted to microcellular foams.

2.3.2 Rotational Foam Molding

The conventional rotational molding process can be modified for polymer foam processing. The basic principle of rotational foam molding is similar to the batch process, which includes cell nucleation, cell growth and cell stabilization. Instead of a physical blowing agent (PBA), a chemical blowing agent (CBA) is commonly used in rotational foam

molding. CBA is characterized as a sort of thermally unstable chemical that can generate gas under elevated temperature in foam processing.

Although the rotational molding technique has been in use for more than thirty years, the research efforts in the rotational molding of foamed parts remain limited. Liu and Tsai completed a basic study of molding polyethylene foams by powder [64, 65]. Liu et al. studied the rotational molding process of low density LLDPE foams and the effects of processing parameters such as the amount of blowing agent and the processing temperature [66]. Pop-ilev et al. processed Polypropylene foam with a rotational molding setup by controlling the melt strength of the polymer [67].

2.4 Polymer/Clay Nanocomposite

2.4.1 Processing

Polymers have been filled with reinforce compounds such as glass fiber or carbon fiber to improve their mechanical properties. Generally, the interfaces between reinforcement and polymer matrix always contain imperfections. If the reinforcement reaches molecular or atomic level, the interfaces are enhanced and a dramatically improved reinforcement is expected to be obtained [68]. Therefore, layered silicon clays with a thickness on the order of one nanometer become a promising filler reinforcement to improve the properties of polymers. Unfortunately, a well dispersed polymer/clay nanocomposite is not easy to be produced. The nanometer scaled clays tend to agglomerate together instead of dispersing evenly in the polymer matrix due to their large surface area. Also, layered silicates usually

contain hydrated Na^+ or K^+ ions [69]. Ion-exchange reactions with cationic surfactants were applied to convert the normally hydrophilic silicate surfaces to organophilic ones in order to facilitate layered silicon clays compatible to most polymers [70].

Efforts were made to obtain improved dispersion and structure of polymer/clay nanocomposites. The preparation methods are classified into three different groups according to Ray and Okamoto [70]: Intercalation from solution, in situ intercalative polymerization method and Melt intercalation method. Intercalation from solution involves a solvent such as water, chloroform, or toluene. This method requires that the polymer should be dissolvable by the solvent selected; and the layered silicate clay is swellable in the solvent. The layered silicate and polymer solution are mixed and then the solvent is removed. The polymer chains intercalate between the silicate layers and the polymer/clay nanocomposites are obtained. In in-situ intercalative polymerization method, layered silicate is swollen in the liquid monomer or a monomer solution before polymerization. Melt intercalation method involves mixing the molten polymer with layered silicate clay, usually under high shear stress.

2.4.2 Properties of Nanocomposites

Various properties of polymer/layered silicate nanocomposites were reviewed by Ray and Okamoto [70]. The polymer/clay nanocomposites (PCNs) provide improvements on mechanical properties, heat distortion temperature, thermal stability, fire retardant properties, gas barrier properties, ionic conductivity, optical transparency, biodegradability of

biodegradable polymers-based nanocomposites and other properties. PMMA/Clay nanocomposite was synthesized using a range of different methods. D. C. Lee and L. W. Jang [71] prepared a PMMA-Clay hybrid composite by in-situ polymerization method using MMA monomer and Na+-montmorillonite. Substantial improvements in the thermal stability and tensile properties of the products were obtained. PMMA/montmorillonite (MMT) nanocomposites were synthesized by Qu et al. [72] using a technique called bulk polymerization. The tensile responses of the obtained nanocomposite were greatly improved. The optimized tensile strength and impact strength was obtained from PMMA namocomposite with 0.6 wt. % MMT. PMMA/MMT nanocomposites were also synthesized via in situ polymerization method by other researchers [73-76]. In comparison with pure PMMA, the thermal stability, glass transition temperature, and mechanical properties of the polymer are enhanced by the presence of the nanometer scale fillers. Most of these PMMA nanocomposites present intercalated morphologies. The dispersion of nanoclay particles in PMMA was prepared using the melt-blending technique by Park and Jana [77]. In their study, epoxy was employed to aid the dispersion and to utilize the convenience of melt-blending methods without degradation of polymers in order to obtain a fully exfoliated morphology.

2.4.3 Polymer/Clay Nanocomposite Foam

In the gas foam processing method mentioned above, a very small amount of well dispersed nanoclay will generate a large number of heterogeneous nucleation sites. Therefore, the nanoclay is expected to facilitate the foaming process. Polystyrene (PS) and PMMA

nanocomposite foams by Zeng et al. [78], polycarbonate (PC) nanocomposite foam by Mitsunaga et al. [79], and Polypropylene (PP) nanocomposites foam by Nam et al. [80] were processed using a batch foaming method. Low Density Polyethylene (LDPE) nanocomposite foam by Wang et al. [81], metallocene polyethylene (mPE) nanocomposite foam by Guo et al. [82], and PS nanocomposite foam by Han et al. [83] were processed using an extruder. These works indicates that nanoclay greatly changes the morphologies of these nanocomposite foams. The addition of a small amount of nanoclay considerably reduces the cell size while increases cell density.

2.5 Mechanical Properties of Foams

Mechanical properties of traditional foams have been studied extensively. The mechanical properties of foam depend on the properties of the material from which it is made, their relative density and their geometric structure. Both experimental and theoretical approaches were utilized to reveal the property-structural relationship of various foam materials. Recently, computer simulations such as finite element analysis have been of great interest as they can solve the mechanical response of materials with complex geometry. Despite appreciable progress, no theoretical model has been found to accurately describe the mechanical response with consideration of all the factors that affect the mechanical properties. Previous results on the mechanical properties of foam were reviewed by Hilyard [84, 85] and Gibson and Ashby[104]. One of the most widely accepted models was proposed by Gibson and Ashby[104]. In their models, the relative modulus and strength of

the foams were expressed as functions of the relative density. For instance, the relative modulus and yield strength under compression of opened cell foams were given respectively by:

$$\frac{E_f}{E_p} \approx \left(\frac{\rho_f}{\rho_p}\right)^2 \tag{3.1}$$

and

$$\frac{\sigma_f}{\sigma_p} \approx 0.23\left(\Phi\frac{\rho_f}{\rho_p}\right)^{3/2}\left(1+\left(\frac{\rho_f}{\rho_p}\right)^{1/2}\right) \tag{3.2}$$

where E_f is Young's modulus of the foam; E_p is Young's modulus of the unfoamed solid; σ_f is the stress at yield of the foam; σ_p is the stress at yield of the unfoamed solid; ρ_f is the foam density; ρ_p is the unfoamed solid density and Φ is fraction of solid in the cell struts.

The mechanical properties of microcellular foams processed with the gas foaming process were the topic recently of great interest to the research community. Tensile behavior of microcellular polycarbonate foams was investigated by Kumar et al. [1]. Microcellular polyvinyl chloride (PVC) foams were studied by Matuana et al. [9]. Sun et al. [86, 87] examined the mechanical properties of polysulfone, polyethersulfone and polyphenylsulfone microcellular foams. However, the mechanical properties of those microcellular foams have not been extensively studied. Most of these research tried to relate the mechanical properties of the foams with their relative density without looking at the effect of processing parameters.

2.6 Acoustic Properties of Foams

Sound can be considered as a wave phenomenon. A sound wave is "a longitudinal wave where particles of the medium are temporarily displaced in a direction parallel to energy transport and then return to their original position" [88].

Cellular foam material can be used as an acoustic absorber. The mechanism for reducing sound depends on the sound source. If the sound source is within a room, then sound should be absorbed. Sound waves should be insulated if they are coming from outside then to keep sound out. The structure needs to be isolated from the vibration source if it is being transmitted through the structure. Cellular and porous solids can be good absorbing media and they can help isolation. However, they are not very good at insulation against sound [89].

The foams with closed cell structures do not absorb sound at all. The reason is that the fluid within the pores cannot move and dissipate energy. To enhance acoustic absorption it is necessary to allow air motion within the foamed spaces [90]. Therefore, for acoustic absorption applications, opened cell foam is desired.

T.J. Lu et al investigated the use of semi-opened cell metal foams for sound absorption. The foams were processed with a negative-pressure infiltration method, using preform made of soluble spherical particles. An analytical model was developed to quantitatively study the dependence of pore connectivity on the processing parameters including infiltration pressure, particle size, wetting angle and surface tension of the molten alloy [91].

Allard [92] has shown that porous materials can be well described with the help of the Biot theory [93, 94] and has given an excellent review of several models and experimental research that describe sound propagation in air-saturated porous media. When excited by acoustic waves, frames of these materials behave approximately as acoustically rigid over a wide range of frequencies. The porous material can be then replaced on the macroscopic scale by an equivalent fluid of density $\tilde{\rho}(\omega)$ and bulk modulus $\tilde{K}(\omega)$ that occupies a proportion ϕ of the volume of the porous material. In the fluid equivalent model of Johnson-Allard [92], these quantities depends on five geometrical properties of the porous medium: the airflow resistivity σ ($N.s.m^{-4}$), open porosity ϕ (%), tortuosity as defined by Johnson, α_∞ [95], and the viscous and thermal characteristic lengths Λ(μm) and Λ'(μm). The knowledge of these parameters and their measurements are important since they determine the acoustic performance of the porous material and also predict its acoustic response in various industrial applications. These five parameters are usually called geometrical properties of the porous material since they depend only on the internal geometry of the porous network of the material.

Chapter 3: Processing Design

3.1 Introduction

In this chapter several foam processes i.e. batch foaming, rotational mold foaming and constrained foaming are designed for processing different foam materials that would be used in further experiments.

As descried in the previous chapters, high pressure physical blowing agents such as CO_2 and N_2 can be used to produce foams with cell sizes on the order of micrometer level. In order to study the foaming procedure of this process and the effects of various processing parameters on the resultant foam product, a foaming system which can easily and accurately control the gas pressure, foaming time and foaming temperature is required. A batch foaming setup is designed to meet these requirements.

Rotational molding can be modified and applied to foam producing using a chemical blowing agent (CBA), which was introduced in the previous chapter. In comparison with the batch processing method, rotational mold foaming offers many advantages such as a wide range of part size, a good surface finish, being able to handle multilayered parts with complex geometry, and a higher productivity. Since there is no high pressure gas involved in rotational mold foaming process, which decreases both the cost and the safety risk, this process is attractive to industry manufacturing. A rotational mold foaming setup is designed for studying this process.

The geometry of samples produced by batch foaming is generally in thin sheet form to ensure an acceptable saturation time. If the aspect ratio (the length to width ratio) of the sheet is large, the samples tend to deform during the foaming process due to inherent small imperfection and non-uniformity of the samples. As a result the foamed samples become distorted, which is undesirable for industrial applications and experiments. As explained in the follow sections, a constrained foaming process is designed to suppress this distortion and obtain foamed materials with desired geometries.

3.2 Design of the Batch Foaming Process

The batch foaming process include several steps including formation of gas/polymer solution, cell nucleation, cell growth and cell stabilization, as described in the last Chapter. The schematic illustration in Figure 1 describes the batch foaming process.

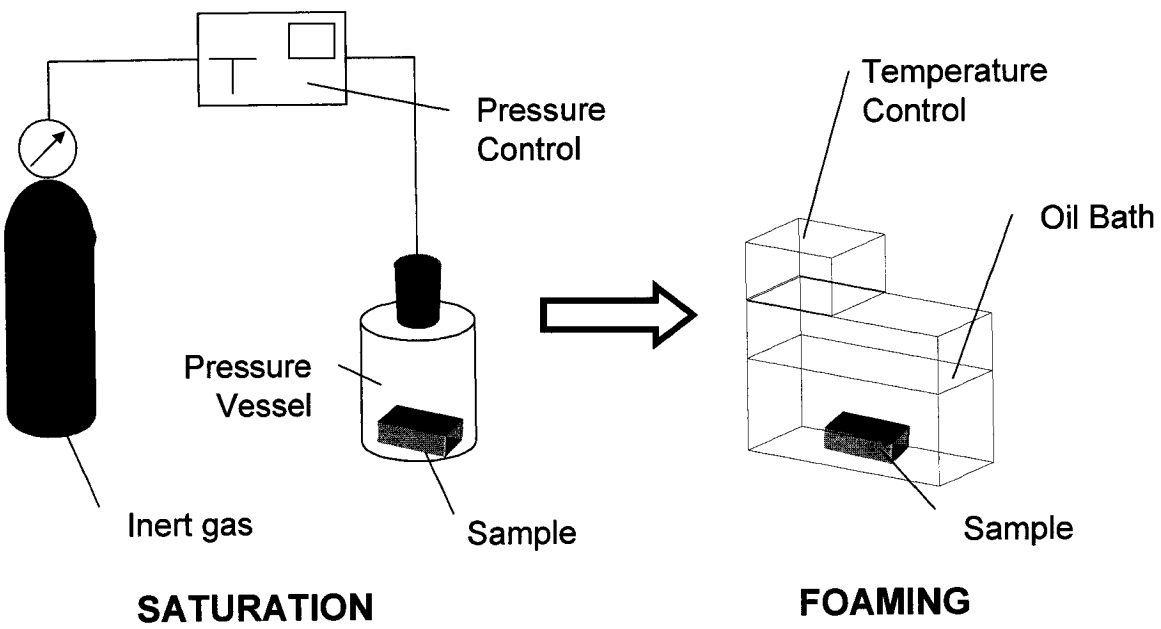

Figure 1 Schematic illustration of batch foaming process

3.2.1 Gas/Polymer Solution Formation

An equilibrium polymer-gas solution requires a source of high-pressure gas. As shown in Figure 1, the physical hardware selected to supply high-pressure gas was a compressed CO_2 cylinder. CO_2 cylinders were available in standard 6.14 MPa and high-pressure 15.86 MPa product formats. A VCR fitting assembly supplied by Swagelok was used to contain the polymer and gas during the saturation step. The requirement for the pressurize subsystem includes the gas pressure control, gas pressure motoring, and fast and slow pressure releasing.

It is necessary to adjust the pressure to the containment device in order to control the gas concentration in the polymer samples. A pressure regulator was installed between the gas cylinder and the pressure vessel to satisfy this requirement. It is important to know the pressure in the vessel to control the gas solubility in the polymer. A pressure transducer and indicator was installed in serial with the pressure regulator. Subjecting the saturated polymer to a rapid pressure drop is necessary to inducing nucleation. This strategy for nucleating cells is particularly useful when the saturated plastic is highly plasticized. This rapid pressure drop can was accomplished by opening the threaded VCR end plug. Slowly reducing the pressure inside the saturating vessel is sometimes necessary. This is always required when a large volume vessel is depressurized. A needle valve was installed to slowly release the high-pressure gas to the atmosphere.

The saturation time, which depends on both the gas diffusivity and the polymer

thickness, can be estimated using the initial slope method given by [96]:

$$t = \frac{\pi h^2}{16D} \tag{3.1}$$

where t is the saturation time, h is the sample thickness and D is the diffusion coefficient, which can be obtained from literature or experimentally.

3.2.2 Cell Nucleation and Growth

Cell nucleation and cell growth were induced by thermal instability. Thermal instability requires that the polymer/solution is in a super-saturated state, which can be achieved by a decrease in pressure or increase in temperature or both. In practice, when the sample was fully saturated, it was removed from the pressure vessel and submerged in a hot bath with accurate temperature control to induce cell nucleation and growth. The liquid in the hot bath can be water or oil, depending on whether the required temperature exceeds 100 °C. The required foaming temperature is different for each particular polymer, which is usually determined by the plasticizing temperature. It should be noted that some polymers can be highly plasticized at room temperature when a great amount of gas is dissolved in the sample due to the shift of glass transition temperature (T_g). In these cases, the cell nucleation starts right after the pressure is released, and submerging the sample in the hot bath becomes optional depending on the required foam morphology.

3.3.3 Cell Stabilization

In order to obtain polymeric foam with small cell sizes, the coalescence of the cells

should be restrained. A cold bath containing a mixture of water and ice was used to meet this requirement. When the foam had expanded to a desired volume, the samples were immersed into ice water to stabilize the foam structure. According to Henry's Law described in the previous chapter, the gas solubility at low temperature is much higher than that in a hot bath. The polymer/gas system returned to thermodynamic stable state. The suddenly dropped temperature also increased the viscosity of the polymer and the cell growth stopped immediately. After the sample was exposed to ambient pressure and temperature, a stable foam structure was obtained.

After the cell stabilization, the residual gas in the polymer will eventually diffuse out of the polymer. Before testing of the foamed sample, it should be air dried for several days after the foaming experiment.

3.3 Design of the Rotational Mold Foaming Process

In this section, the design of a uniaxial rotational mold foaming setup for polymeric foam processing is conveyed. An axiomatic design [97] approach was applied to create a conceptual design. SolidWorks CAD software was used to generate the three-dimensional models and two-dimensional drawings of the required parts.

3.3.2 Conceptual Design

3.3.2.1 Parent Level Conceptual Design

The objective of this design is: starting with a traditional rotational molding setup,

produce foamed polymer materials with various geometries. Although using a different approach, the proposed rotational mold foaming process still consists of the same steps as the gas foaming method: mixing, cell nucleation, cell growth, and cell stabilization. Therefore, the parent level functional requirements (FRs) for the product are defined as:

FR_1 = Nucleate cells

FR_2 = Grow cells

FR_3 = Stabilize cells

FR_4 = Control part geometry

In order to satisfy these function requirements, four designing parameters are proposed:

DP1 = Material parameters

DP2 = Heating device

DP3 = Cooling device

DP4 = Mold geometry

In order to map the FRs in the functional domain to the DPs in the physical domain, a design matrix [A] was proposed in form of:

$$[A] = \begin{bmatrix} A_{11} & A_{12} & \cdots & A_{1n} \\ A_{21} & A_{22} & \cdots & A_{2n} \\ \vdots & \vdots & & \vdots \\ A_{m1} & A_{m2} & \cdots & A_{mn} \end{bmatrix} \tag{3.2}$$

where m is the number of FRs and n is the number of DPs

The links of the FRs vector and the DPs vector can be expressed as:

$$\{FR\} = [A]\{DP\} \tag{3.3}$$

This equation is called design equation [97]. In this case, the design equation becomes:

$$\begin{Bmatrix} \text{Cell Nucleation} \\ \text{Cell Growth} \\ \text{Foam Structure Stablizing} \\ \text{Part Geometry} \end{Bmatrix} = [A] \times \begin{Bmatrix} \text{Material Parameters} \\ \text{Heating Device} \\ \text{Cooling Device} \\ \text{Mold Design} \end{Bmatrix} \tag{3.4}$$

The FR_1, cell nucleation, relies on two DPs. The first DP is the material parameters, such as the melting point of the polymer, decomposition temperature of the blowing agent, and the particle sizes of the materials. The decomposition temperature of the blowing agent should be higher than the melting temperature of polymer. The particle size affects both the uniformity of the polymer-CBA solution and the nucleation site. The second DP that affects FR_1 is the heating device. The temperature of the mold should be increased gradually from room temperature to the melting temperature, and then to the decomposition temperature.

FR_2, cell growth, can be controlled by the mold temperature. The viscosity of the polymer, which increases with an increased temperature, is an important parameter to control the cell grows. The activity of the gas generated by the CBAs is also affected by the mold temperature. Therefore, a controllable heating device is required to manipulate the cell growth.

FP_3, Foam structure stabilization, should be achieved by a cooling device. Oversized cells will deteriorate the mechanical properties and thermal isolation properties. Consequently, the cell growth should be controlled. By cooling the mold to a temperature below the melting temperature of the polymer, the foam structure is stabilized. Water cooling and air cooling are to be used during the process to achieve the cooling of the mold.

The FP_4, Part geometry, can be readily realized by the mold design. The geometry of the resultant part should take the shape of the inside surface of the mold. In this study, a cylinder mold is selected in order to simplify the problem.

Based on the discussion above, the design equation (3.3) can be expressed as:

$$\begin{bmatrix} \text{Cell Nucleation} \\ \text{Cell Growth} \\ \text{Foam Structure Stablizing} \\ \text{Part Geometry} \end{bmatrix} = \begin{bmatrix} A_{11} & A_{12} & 0 & 0 \\ 0 & A_{22} & 0 & 0 \\ 0 & 0 & A_{33} & 0 \\ 0 & 0 & 0 & A_{44} \end{bmatrix} \times \begin{bmatrix} \text{Material Parameters} \\ \text{Heating Device} \\ \text{Cooling Device} \\ \text{Mold Design} \end{bmatrix} \tag{3.5}$$

In this design equation, the design matrix is triangular. Therefore, this design is a decoupled design.

3.3.2.2 Decomposition of Function Requirements

Foam cell should nucleate from very small and uniformly distributed nucleation sites. Note that high pressure is not required for rotational molding. The solubility of gas in polymer can be described by Henry's law. According to Henry's law given by Equation (2.1), the solubility is proportional to the pressure. At atmospheric temperature, there is little gas dissolved in the polymer matrix. As a result, most of the cell nucleation initials from the CBA particles. Fine CBA particle sizes are required because large CBA particles result in a coarse foam structure.

It is imperative that the CBA decomposition should be taken place after a liquid layer of polymer was formed. The temperature profile of polymer-CBA mixture should gradually increase from the melting point of the polymer to the decomposition temperature. A heavy

duty oven with feedback control is employed as the heating device.

The FR_1 cell nucleation can be further decomposed into second level function requirements:

FR_{11} = Polymer/CBA mixture formation

FR_{12} = Plastication

The following second level DPs are defined to satisfy the second level FRs:

DP_{11} = Grinding Particles

DP_{12} = Oven Temperature Control

Therefore, the second level design equation can be written as:

$$\begin{bmatrix} FR_{11} \\ FR_{12} \end{bmatrix} = \begin{bmatrix} (A_1)_{11} & 0 \\ 0 & (A_1)_{22} \end{bmatrix} \bullet \begin{bmatrix} DP_{11} \\ DP_{12} \end{bmatrix} \tag{3.6}$$

In this design equation, the design matrix is diagonal, which means that the function requirements can be independently satisfied.

3.3.3 Rotational Mold Foaming System Design

Figure 2 shows a schematic of the proposed rotational mold foaming setup. The equipment consists of a cylindrical mold, a motor, a hollow shaft, an oven, a temperature controller, a thermocouple, a water cooling device, and a moveable worktable. The thermocouple is located within the hollow shaft to measure the temperature in the mold during rotational foam molding. To simplify the process, a uniaxial rotational motion was employed. The design of each part in this setup was performed according to the analysis of

the functional requirements and design parameters. The detailed designs of each part are shown in the Appendix B of this thesis in term of mechanical part drawings.

3.3.3.1 Mold

The mold was constructed form aluminum to ensure good thermal conductivity. The mold consists of three pieces: upper mold, bottom mold and a cover to facilitate the removal of the foamed material. The geometry of the inner surface is determined according to the application requirement. In this research, cylinder mold shape was used to investigate the rotational mold foaming process. A three dimensional view of the mold is shown in Figure 3. A detailed part drawing of the mold is in the appendix.

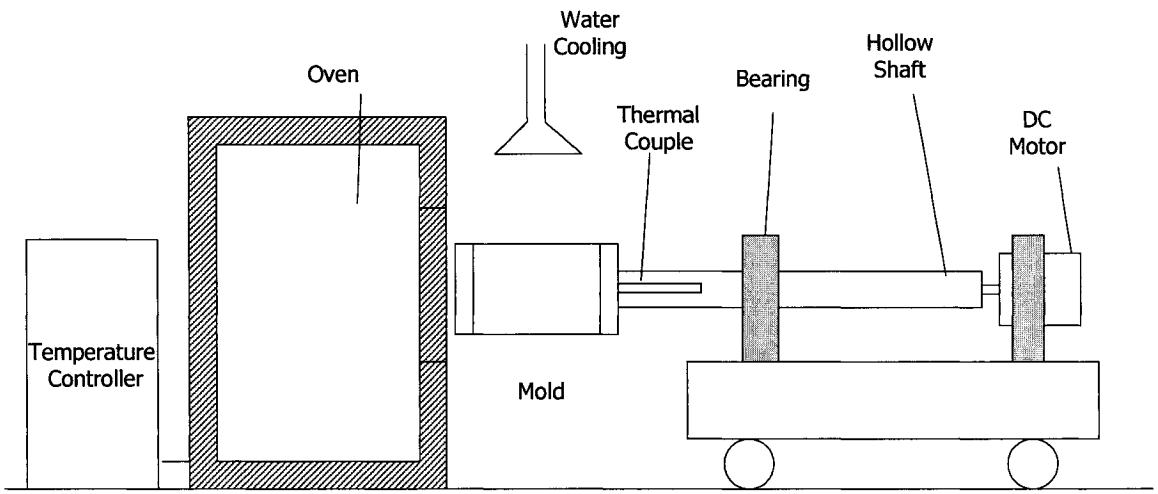

(a)

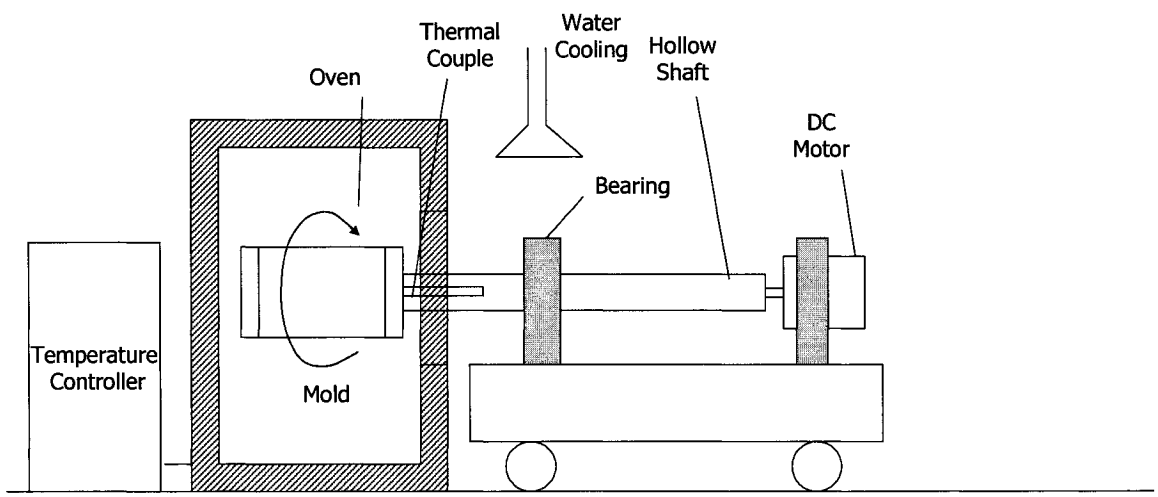

(b)

Figure 2 Prototype of the rotational mold foaming setup (a). before and after the process and (b). during the process

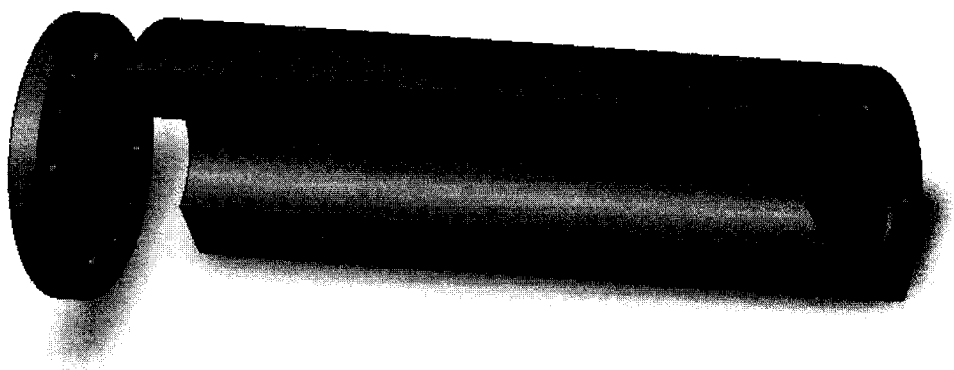

Figure 3 Three-dimensional image of the mold

3.3.3.2 Power Train

The requirement for the design of the power train subsystem is to be able to accelerate the mold from rest to 60 rpm within one second. First of all, the mechanics of the load should be analyzed. The load includes both friction and inertia. Assuming the bearing is well lubricated, the friction of this system was neglected. Inertia, which is the resistance of an object to acceleration, was calculated by analyzing the mechanical linkage system that is to be moved [98]. In this case, the sum of moments of inertia of all the rotating parts J can be obtained from the three-dimensional part models in CAD software:

$$J = 6.5449\times10^{-5}\, g\bullet m^2 \tag{3.7}$$

Once the mechanics of the application have been analyzed, and the inertia of the load were known, the next step was to determine the required torque levels. Then, a motor can be selected to deliver the required torque. If friction and inertia are not properly determined, the motion control system will either take too long to position the load, or it will be unnecessarily costly. As previously mentioned, the requirement of the speed control is to be able to reach 60 rpm from 0 rpm with 1 second. The torque required can be calculated:

$$T_r = J\times\dot{\omega} = J\times\frac{2\pi\omega}{t} = 4.11\times10^{-3}\, N\cdot M \tag{3.8}$$

where T_r is the torque required, J is the moment of inertia, ω is the angular velocity, t is the time requirement. The required motor power can be calculated as:

$$P_r = T_r\bullet\omega = 2.58\times10^{-5}\, KW \tag{3.9}$$

The motor was selected to have a continuous torque of 11.2×10^{-3} N·M, which was

greater than the required torque and met the design requirement. A DC power supply with controllable voltage was used to drive the DC motor. By controlling the voltage of the DC motor, the rotation speed of the mold could be adjusted.

3.3.3.3 Heating and Cooling

The heating procedure of the rotational mold foaming is a transient heat transfer problem. The outer surface of the mold is heated by the high temperature of the air in the oven. Convection is the primary means of heating the oven. By assuming the oven temperature is constant, the inside temperature of the oven can be evaluated using lumped heat capacity:

$$\frac{dT}{dt} = \frac{-h}{\rho cL}\left[T_{(t)} - T_{\infty}\right] \tag{3.10}$$

where ρ is the density of the mold material, c is the specific heat of the mold material, L is the mold wall thickness, h is the convection heat transfer coefficient, T is the instant temperature of the mold inner surface, T_{∞} is the oven temperature. The solution of this differential equation is given as:

$$T_{(t)} = T_{\infty} - (T_{\infty} - T_0)\exp(-\frac{h}{\rho cL}t) \tag{3.11}$$

where T_0 is the initial temperature, i.e. room temperature. In this case, L = 15 mm, ρ = 2770 kg/m^3, and c = 875 J/kg·K. Based on the mold design, the convection heat transfer coefficient of the surface of the aluminum mold was given as 25 W/m^{2}K. The room temperature is 23°C (296K). If the oven temperature is set, the theoretical inner temperature

of the mold can be determined as a function of time and is plotted in Figure 4.

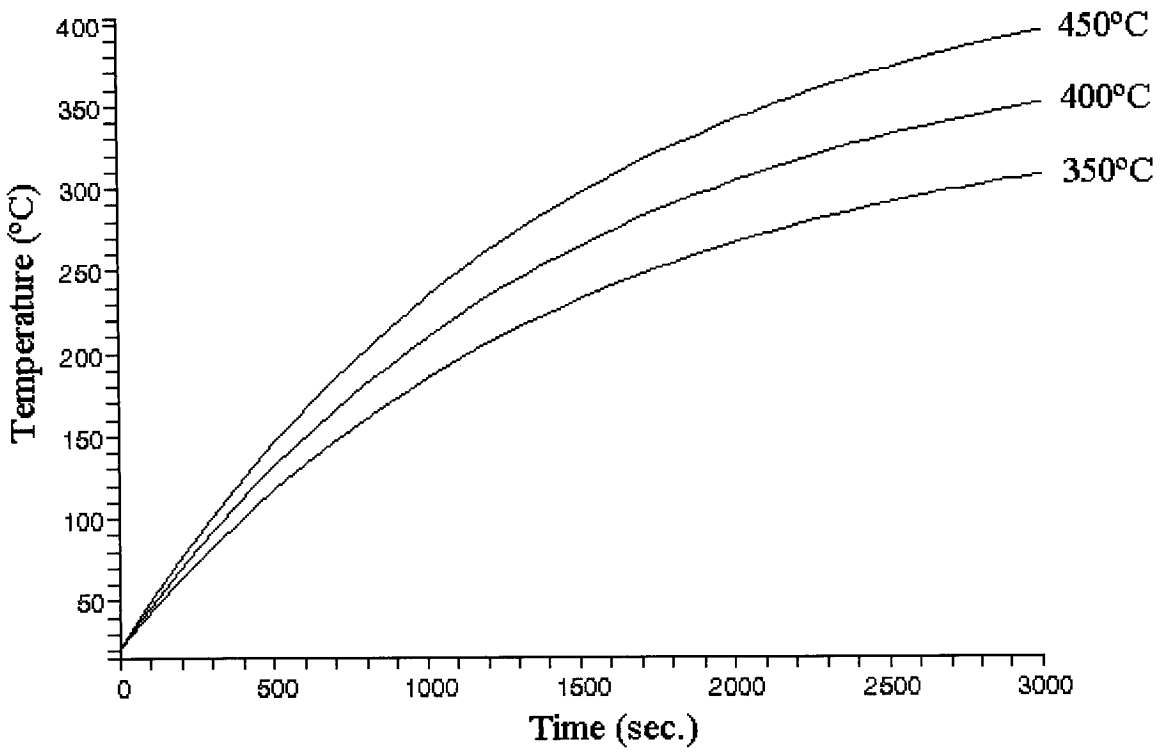

Figure 4 Time dependence of the mold temperature for different oven temperatures form 350 °C to 450 °C

The temperature reaches 200 °C after approximately 1500 seconds (25 minutes). Therefore, if the decomposition temperature of the selected CBAs is 200 °C, the heating time should be at least 25 minutes. If a different CBA is used, or a different oven temperature is selected, the heating time can be reestimated using Equation (3.11). It should be noted that this calculation did not consider the heat required to melt the polymer and decompose the CBA. Therefore, the actual processing time should be slightly longer than the calculated value.

After the desired foam morphology is obtained, the mold is removed from the oven. A water cooling system is used by spraying cold water on the surface of the mold. When the interior of the mold drops to a temperature below the melting temperature, the foam structure is fixed and the foamed part is ready to be extracted from the mold.

3.3.3.4 Temperature Monitoring

A temperature monitoring system was employed in order to monitor the temperature profile of the mold as a function of time during the foaming process. A thermocouple was inserted within the hollow shaft, such that the tip of the thermocouple is inserted in the vent hole of mold. The wire leads of the thermocouple are connected to a digital meter to display the temperature of the mold. Since the hollow shaft is rotating during the process, a special device is required to meet this requirement. Two copper rings and one plastic ring were implemented here: the plastic ring act as an electrical isolator used to isolate the hollow shaft and the copper rings. Two holes are drilled in the plastic ring at the position of the two copper

rings. The two wires pass through the holes and are soldered to the two copper rings respectively. Two electrical brushes contact the outer side of the copper rings on one end and are connected to the digital meter. While the process is running, the thermocouple, plastic ring, and copper rings move with the hollow shaft while the brushes remain stationary. Therefore, the signal of the thermocouple was delivered outside of the hollow shaft and the temperature of the mold could be effectively monitored.

3.3.3.5 Other Parts

A moveable worktable was designed to support the rotational mold foaming setup. The hollow shaft was connected to a DC motor by a clutch. They were supported by a bearing on the hollow shaft and a bracket on the DC motor. The bearing and bracket were fixed to the moveable worktable. A pair of rails under the moveable worktable were used to facilitate the linear motion of the mold. The mechanical drawings of all these parts are included in the Appendix B. A pictorial view of the rotational foam mold setup is shown in Figure 5.

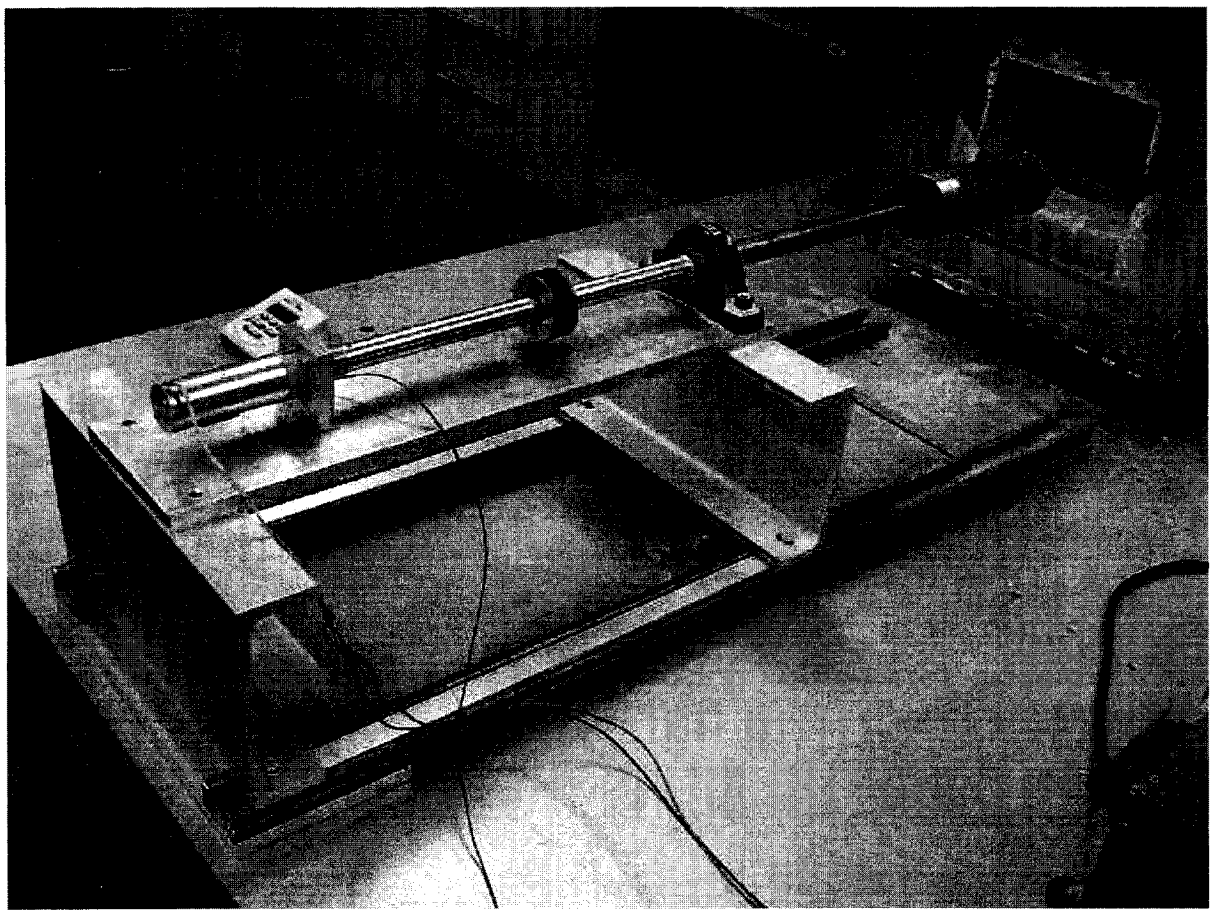

Figure 5 Rotational mold foaming machine

3.5 Design of the Constrained Mold Foaming Process

In the batch foaming process, the polymer samples expanded freely within the hot bath. To avoid an excessively long saturation time, a thin polymer sheet was commonly used. However, when the aspect ratio (the ratio of the length to the thickness) of the polymer sheet is large, the obtained samples were usually distorted. Since the samples were plasticized during the foaming procedure, any imperfection inside the polymer samples or very small geometric asymmetry of the sample would induce a large deformation. A PMMA sample produced using the batch foaming setup is shown in Figure 6 (a). The deformation is undesirable for both industrial applications and research experiments and should therefore be suppressed. It can be achieved by constraining the expansion of the polymer/gas system during the foaming process [99].

A constrained mold foaming, which is a modification of the batch foaming process, was designed as shown in Figure 7. Unlike the batch foaming process in which the polymer is foamed freely in a liquid bath, an aluminum mold was designed to constrain the mold foaming process. The geometry of the mold was designed according to the requirements of different applications. The mold was preheated in a hydraulic press before foaming. The temperature of the press was preset to the foaming temperature of the foaming process. A saturated sample was removed from the pressure vessel and immediately put in the mold. The mold was then closed to heat the sample and induce cell nucleation and growth. Since the expansion of the sample was under the constraint of the mold, the sample took the mold

geometry. After the press was cooled, the mold was reopened and the foamed part with desired geometry was obtained. Figure 6 (b) shows a foamed sheet produced by the constrained mold foaming process.

It should be noted that the mass of the polymer sample should be carefully selected. The expansion ratio of the sample should be obtained by batch foaming process experiment before using the constrained mold foaming. The mass of the polymer required can be calculated by:

$$m_p = \frac{V_m \rho_p}{\varphi} \tag{3.12}$$

where m_p is the mass of the polymer required, V_m is the volume of the mold, ρ_p is the density of polymer, and φ is the expansion ratio as determined by the batch foaming process.

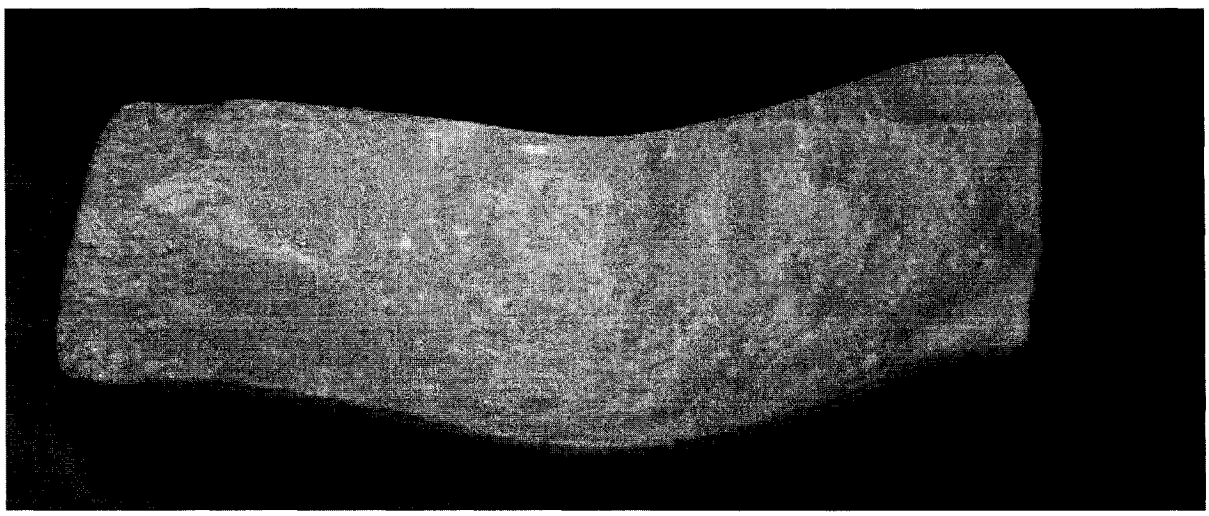

(a)

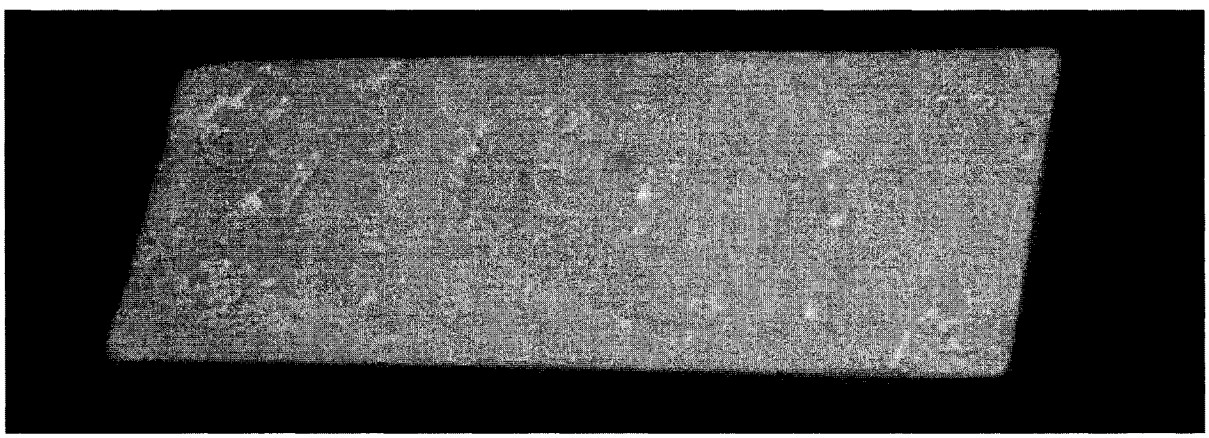

(b)

Figure 6 The foamed PMMA samples using CO_2 as blowing agent: (a) unconstrained and (b) constrained.

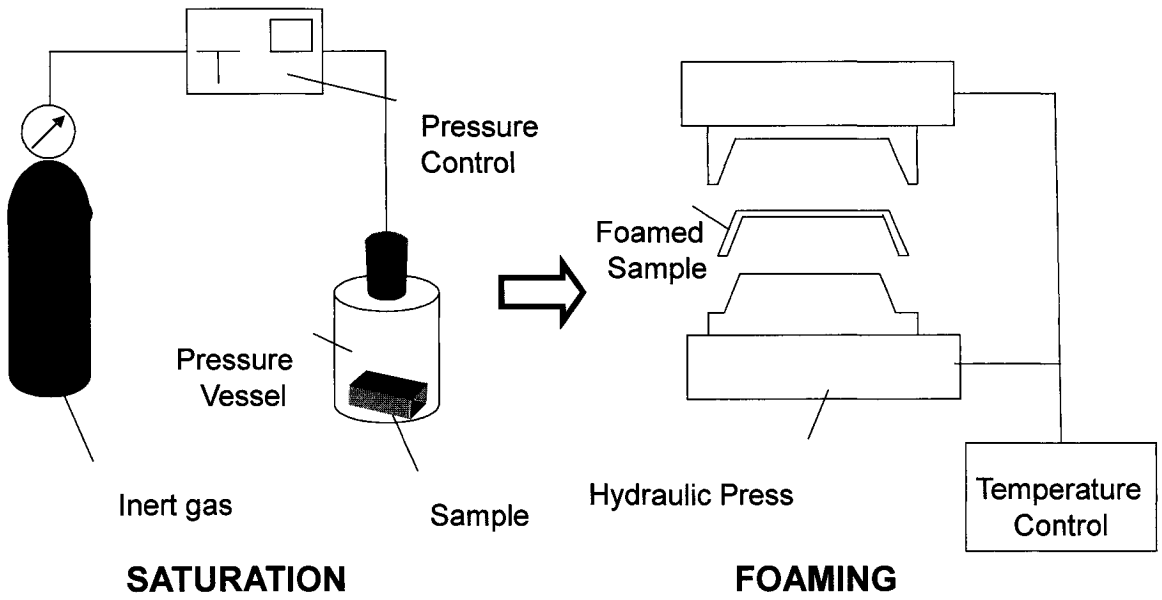

Figure 7 The constrained mold foaming process

Chapter 4: Processing, Characterization, and Mechanical Properties of PMMA Microcellular and Nanocomposite Foam

4.1 Introduction

PMMA is selected as the polymer used in this study. PMMA is a thermoplastic acrylic plastic which is defined by the following chemical notation:

$$-[CH_2-C(CH_3)(COOH_3)]-_x$$

PMMA has many characteristic properties such as high hardness, stiffness and strength, high heat distortion temperature, good electrical and dielectric properties at low frequencies, high weathering resistance and clear to opaque transparency [100]. It is widely used as an alternative of traditional glass, an important biomedical material, and a structural material.

The purpose of this chapter is to investigate the relationships between the processing parameters, structures and mechanical properties of PMMA microcellular foam. The saturation pressure, foaming time and foaming temperature were the most important parameters that can control the foam structure. Therefore, their effects on the foam morphology and mechanical properties are studied. PMMA nanocomposite prepared by a solvent co-precipitation method is to be used to study the effect of nanoclay on the PMMA microcellular foams and their mechanical properties. The results are to help engineers to optimize their designs by altering the processing parameters to obtain preferred mechanical properties for their specific applications with different material weight requirements.

4.2 Experimental

4.2.1 Experimental Materials

PMMA with a M_w=108,500 and a M_n=56,700 was supplied by Canus Plastics. The samples were dried at a temperature of 90 °C for at least 24 hours in a vacuum oven before usage. PMMA resins were hot compression molded into 1.5 mm thick panels with a hydraulic heated press supplied by Carver, Inc for 4 minutes using 5 tons of force. The temperature of the hot pressing plates was 180 °C. Rectangular strips were obtained from the model with dimensions of 6 mm × 50 mm. The blowing agent used was carbon dioxide (CO_2) and was obtained from Praxair, Inc.

The organically modified montmorillonite clay, Cloisite 20A (C20A) from Southern Clay Products Inc, was used for the synthesis of polymer/clay nanocomposite material. This material was prepared by an ion exchange reaction involving the inorganic sodium cations of natural montmorillonite and an organic modifier dimethyl dehydrogenated tallow quaternary ammonium. The modifier concentration in the organoclay was reported by the manufacturer to be 95 meq per 100 g clay and had a layer spacing of 24.2 Å. Analytical reagents methanol and toluene was supplied by Fisher Scientific.

4.2.2 Polymer Nanocomposite

PMMA Nanocomposites with Cloisite 20A contents of 0.5 wt. %, 1 wt. %, and 2 wt. % were prepared using a solvent co-precipitation method. In this method, dispersions of 0.4 wt.

% Cloisite 20A in toluene and solutions of 10 wt. % PMMA in toluene were prepared. After being stored at room temperature for three days, the organoclay dispersions were sonicated in an ultrasonic bath, model FS140 supplied by Fisher Scientific, for 1 hour. The sonicated materials were then added to the PMMA toluene solution while stirring with a magnetic stirrer for 10 minutes. The mixtures were then precipitated in methanol/toluene (20:1 volume parts) with vigorous stirring. The resultant PMMA/Clay precipitate was then washed another two times with methanol/toluene (10:1 volume parts), dried at room temperature for 2 days and finally under vacuum at 90 °C for 3 days [101]. In order to make a comparison, PMMA nanocomposite materials with 0 wt. %, 0.5 wt. %, 1 wt. %, and 2 wt. % C20A organoclay were prepared using a dry blending method. In this case, different amounts of organoclay and PMMA powder were combined in a bottle and mixed by shaking. The resulting PMMA/Clay powders prepared with both methods were then compression molded in aluminum molds with the hydraulic heated press for 4 minutes using 5 tons of force. The temperature of the hot pressing plates was 180 °C. Rectangular strips were obtained from the molds with dimensions of 6 mm × 50 mm × 1.5 mm.

4.2.3 Processing of Microcellular Foams

The foaming experiments were performed in a two stage batch process. In the first stage, the polymer samples were saturated in a high pressure CO_2 bath at a pressure of 3.8 – 5.8 MPa (550 – 840 psi) and at room temperature (21°C-23°C). The saturation time, which varied from 1 day to 2 weeks, was calculated according to the diffusion coefficient of the carbon dioxide in

PMMA [52] and PMMA nanocomposite [101]. In the second stage, the saturated samples were put in a water bath with selected temperature for 5 – 20 seconds. The rapid change in temperature and pressure induced cell nucleation and cell growth. Afterwards, the samples were put in cold water to fix the foam morphology.

4.2.4 Sample Characterization

The samples were air dried for 7 days before testing. The foam density was measured by a buoyancy method using a density determination kit supplied by Denver Instrument. The gravity of the solid was measured in distilled water and in the air. The Archimedean principle was applied for determining the specific gravity of the foams. The relative foam density is defined as the ratio of the foam density and the unfoamed polymer density. The expansion ratio is defined as the ratio of the unfoamed polymer density to the foam density.

The cell structures of these foams were characterized with an optical microscope. The samples were cooled in liquid nitrogen before being fractured to produce a surface with minimum plastic deformation. ImageJ software by National Institutes of Health (NIH), US was used to analyze the average cell size and cell density. The cell density was calculated as the number of cells per unit volume with respect to the unfoamed polymer. The number of cells, n, in a defined area, A, was determined with the help of ImageJ software, and the cell density was then calculated as [102]:

$$N_c = \left(n/A\right)^{3/2} \times \frac{\rho_p}{\rho_f} \tag{3.13}$$

where N_c was the cell density, ρ_f was the density of the foam and ρ_p was the density of the unfoamed polymer.

Intercalated morphology was found in the PMMA nanocomposite using Wide-angle X-ray diffraction (XRD) analysis and scanning electron microscopy (SEM). The solubility and diffusivity of subcritical CO_2 gas in PMMA nanocomposites ware characterized using an in situ gravimetric method. The glass transition temperature (T_g) of the nanocomposites at atmospheric pressure and under high pressure CO_2 was tested using conventional DSC and high-pressure DSC. The foam structures of the nanocomposite foams were characterized using SEM. These results were reported in previous publications of our group [40, 101].

4.2.5 Mechanical Testing

The tensile mechanical properties were tested with an Instron 4202 machine with a 10 KN load cell at room temperature. Rectangular strip samples with a thickness ranges from 1.5 mm to 3 mm, depending on the expansion ratio of the sample, were used for tensile testing. The crosshead speed of testing was 1.0 mm/min. The strain was calculated from the displacement of the crosshead. The elastic moduli were obtained by calculating the slope of the stress-strain curves at the initial linear portions. The experimental results of tensile strength and elongation at break were also reported. A minimum of five specimens were tested for each sample. The average data were reported in this paper.

4.3 Results and Discussions

Closed cell foams with microcellular level cell sizes were obtained. Under microscopic observation, very thin integral skins with a thickness of approximately 5-20 μm are observed on the surface of the samples. Table 1 indicates the processing conditions and morphologies of the specimen used in this study. A detailed discussion on the effect of foaming time, saturation pressure and foaming temperature follows.

Table 1: Processing conditions and foam morphologies of specimens

Saturation Pressure (Mpa)	Foaming Time (Seconds)	Foaming Temperature (°C)	Average Cell Size (μm)	Cell Density (Cells/cm^3)	Relative Foam Density
3.8	10	60	7.6	3.38E+08	0.72
4.5	10	60	8.4	4.31E+08	0.66
5.2	10	60	9.2	5.46E+08	0.55
5.8	10	60	8.8	1.28E+09	0.44
5.8	5	60	8.9	7.20E+08	0.54
5.8	15	60	13.5	4.98E+08	0.41
5.8	20	60	15.0	4.94E+08	0.38
5.8	10	40	9.1	6.60E+08	0.64
5.8	10	80	11.1	1.34E+09	0.35
5.8	10	100	11.7	2.07E+09	0.23

4.3.1 Effect of Saturation Pressure

To study the effect of pressure on foam morphology, the foaming time was fixed at 10 seconds and foaming temperature was fixed at 60 °C. Figure 8 shows that the cell density increased as the saturation pressure increased from 3.8 MPa to 5.8 MPa. The error bars show the standard deviations. The increased cell density can be contributed to the increased amount of gas in the polymer-gas system. The increased amount of gas in turn increased the number of nucleation sites and therefore increased the cell density. A higher pressure provides a higher solubility of CO_2 in the PMMA matrix [52]. In addition, the dissolved CO_2 in the PMMA samples decreased the glass transition temperature. When the pressure increased from 5.2 MPa to 5.8 MPa, the PMMA-CO_2 system changed from glassy states into rubbery states at room temperature in accordance with to the experimental data from the literature. It further increased the solubility of CO_2 in the PMMA matrix [52]. The increased cell density confirmed that the solubility of gas is a very pivotal factor in controlling foam nucleation. The saturation pressure was selected to be 5.8MPa for the other experiments as the cell density was much higher than that at other pressures. The effect of pressure on the average cell size was relatively small within the pressure range of this study. It is reported that the cell size decrease with increasing pressure for microcellular PMMA [50] and polystyrene (PS) [103] foams. However, the foaming process used in the literatures was pressure-quench method in supercritical CO_2 and the pressure ranges are different from those used in this study.

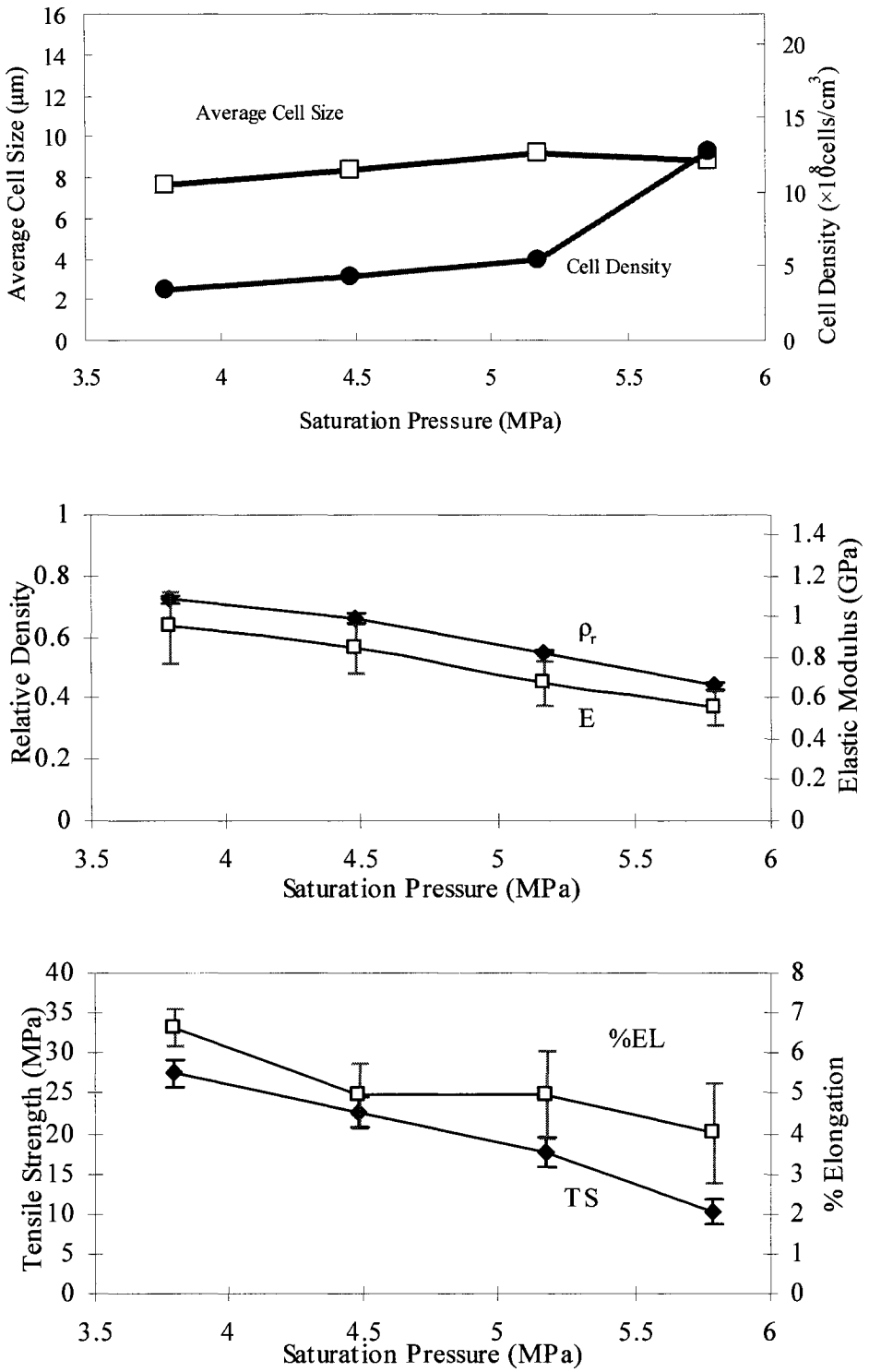

Figure 8 Effects of saturation pressure on PMMA foams: (a). Average cell size and cell density, (b). Relative density and elastic modulus, (c). Tensile strength and elongation at break.

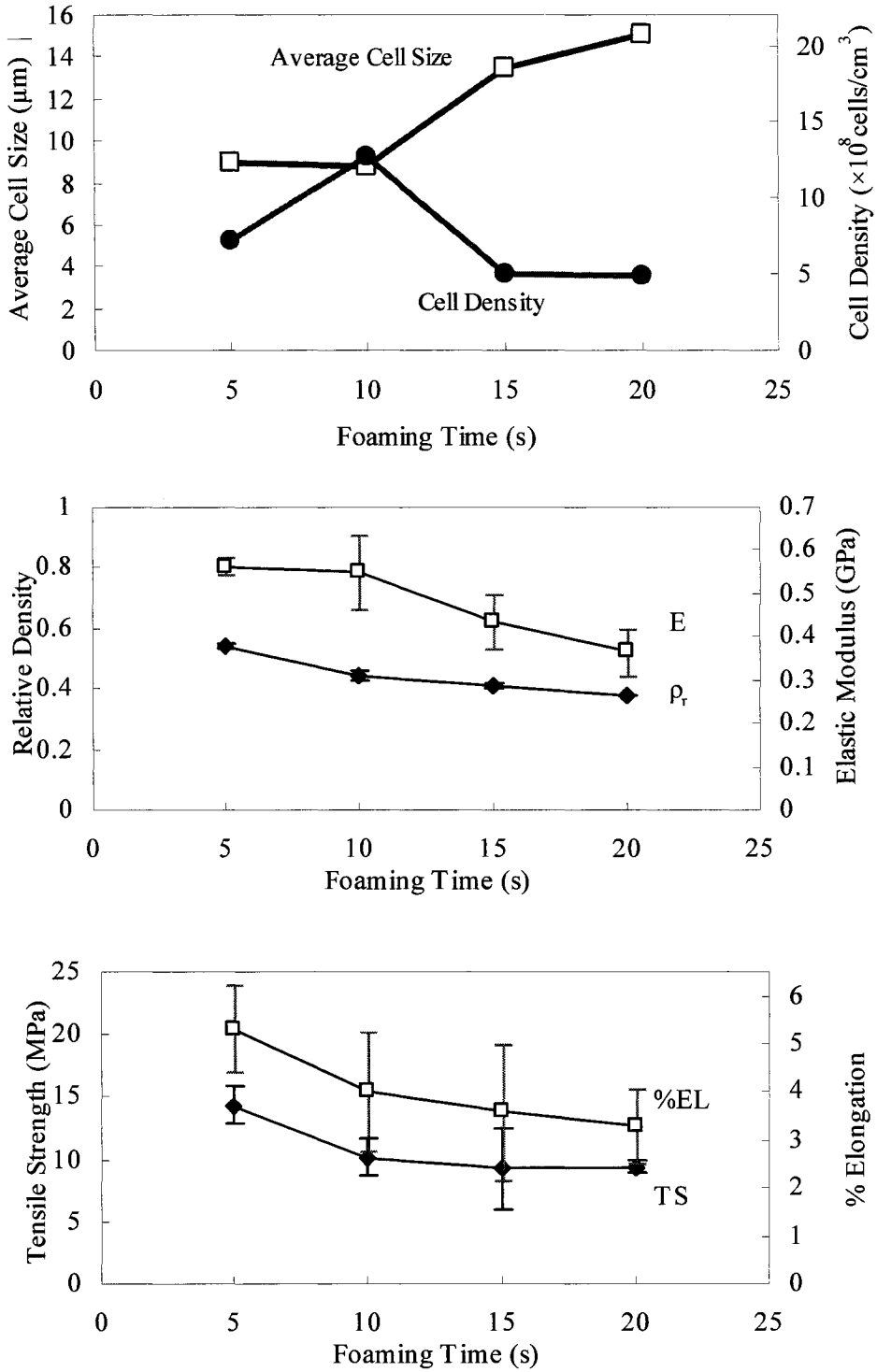

Figure 9 Effects of foaming time on PMMA foams: (a). Average cell size and cell density, (b). Relative density and elastic modulus, (c). Tensile strength and elongation at break

From the plots in Figure 8 it can be observed that the relative density decreased with an increase in the saturation pressure. The increased CO_2 content resulted in a higher nucleation rate, causing the density to decrease. The elastic modulus, tensile strength and the elongation at break of PMMA foam decreased with the increase in the saturation pressure. From Figure 8 it can be noted that when the saturation pressure was as low as 3.8 MPa, the elongation at break was higher than that in the unfoamed PMMA. At 4.5 MPa and 5.2 MPa, the elongation at break was very close to that of the unfoamed PMMA with reduced density. The increasing elongation at break of some foamed PMMA samples possibly results from the small bubbles blunting the crack tips which increased the energy needed to propagate the crack. From the plots in Figure 8, it can be concluded that a higher pressure translates to a lower foam density; however, the modulus, strength and elongation at break decreased.

4.3.2 Effect of Foaming Time

The effect of foaming time on the morphologies and mechanical properties of PMMA foams are presented in Figure 9. The error bars show the standard deviations. To study the effect of foaming time, the foaming temperature was fixed at 60 °C and the saturation pressure was fixed at 5.8 MPa.

The average cell size did not change notably when the foaming time was increased from 5 seconds to 10 seconds. However, average cell size increased rapidly for the foaming times longer than 10 seconds. Cell density increased from 5 second to 10 second and decreased for longer foaming times, as shown in Figure 9. These two curves suggest that the cell nucleation

was dominant early in the foaming procedure. After a certain time, the cell nucleation rate decreased because of the decreased concentration of CO_2 in the polymer matrix which agrees with the classical nucleation theory [6]. The cells kept growing and some of the cells met each other. Some of the cells coalesced forming large bubbles. The cell growth and cell coalescence increased the average cell size and decreased the cell density. In order to get a foam structure with a fine cell size, foaming time should be carefully controlled and cell coalescence should be avoided. The foaming time was selected as 10 seconds in other experiments as the largest cell density was obtained at that foaming time.

The relative density of PMMA foam decreases with increasing foaming times. Meanwhile, the mechanical properties such as elastic modulus, tensile strength and elongation at break all decreased with increasing foaming time. Lower relative density, which means a greater expansion, is generally desirable because the weight of the material become lighter. In reducing the density of the material by increasing the foaming time, careful consideration needs to be taken in verifying the effect on the mechanical properties of the final foamed material.

4.3.3 Effect of Foaming Temperature

Figure 10 shows the plots of the average cell size, cell density, relative foam density, elastic modulus, tensile strength and elongation of PMMA foams as functions of the foaming temperature. The error bars show the standard deviations. All the other conditions such as saturation pressure and foaming time were kept constant. The saturation pressure was 5.8 MPa

and the foaming time was 10 seconds.

The cell density increased dramatically when the foaming temperature increased from 40 °C to 100 °C. The average cell size also increased with the increase in foaming temperature, as shown in Figure 10. The increased cell density should account for a lower viscosity of the PMMA-CO_2 system and higher activity of CO_2 at a relatively high temperature. The increased average cell size suggests that higher temperatures promote cell growth and cell coalescence.

As a consequence of increasing cell density and cell size, the relative density of PMMA foam decreases dramatically. The relative density dropped from 0.75 to 0.23 when the foaming temperature decreased from 40 °C to 100 °C. On the other hand, the elastic modulus and the tensile strength decreased rapidly when the foaming temperature was increased. The elongation at break did not notably drop when the foaming temperature decreased from 40 °C to 60 °C. When the foaming temperature is higher than 60 °C, the foams became very weak and the elongation at break was very small.

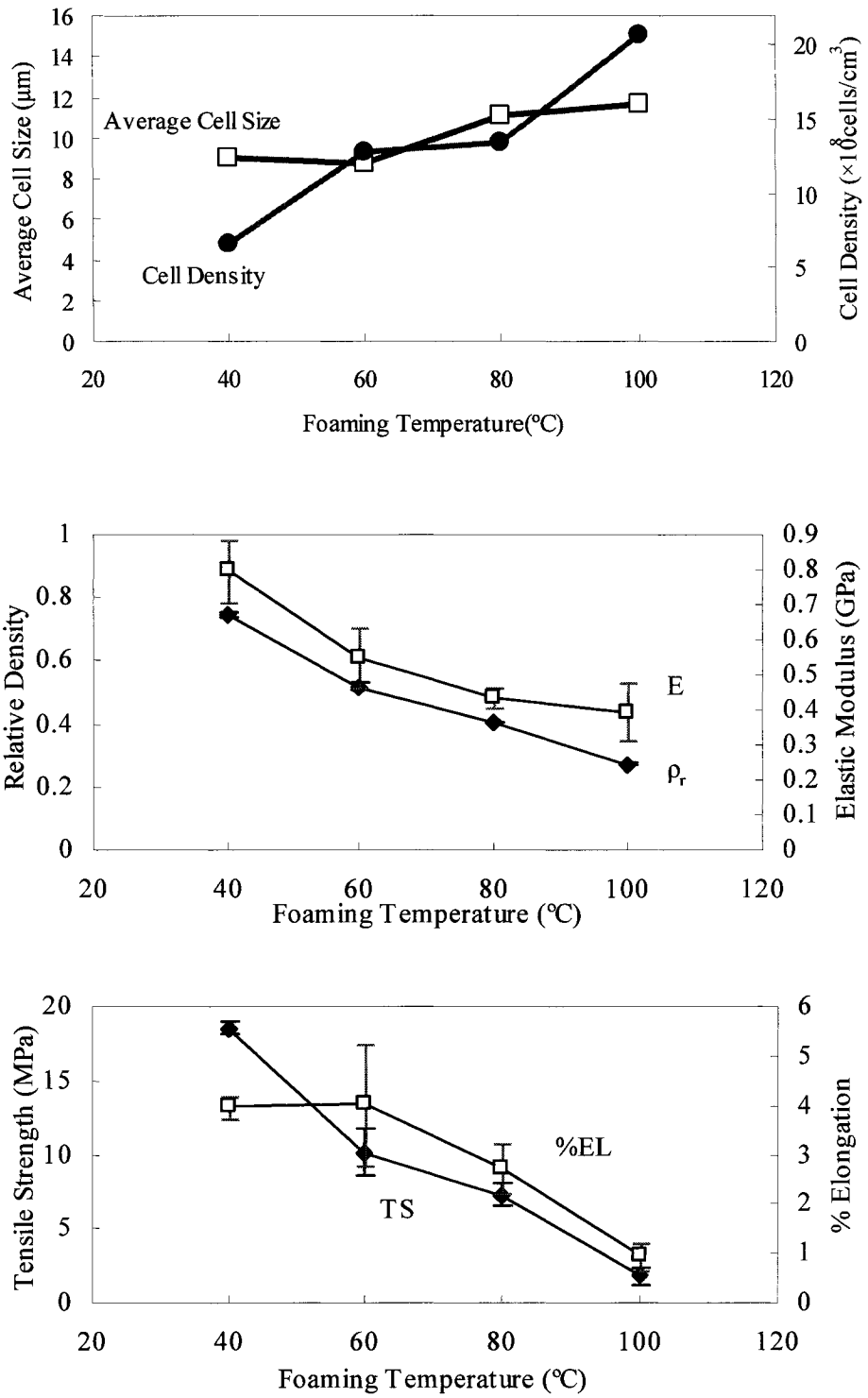

Figure 10 Effects of foaming temperature on PMMA foams: (a). Average cell size and cell density, (b). Relative density and elastic modulus, (c). Tensile strength and elongation at break

4.3.4 Relative Foam Density and Mechanical Properties

The structure-mechanical properties relationship of conventional foam has been studied intensively. Most of these studies attempt to relate the mechanical properties to the relative density. Gibson and Ashby suggested that the tensile elastic modulus and tensile strength for closed cell foam could be predicted by the equation (3.14) and equation (3.15) [104]:

$$\frac{E_f}{E_p} \approx \Phi^2 \left(\frac{\rho_f}{\rho_p}\right)^2 + (1-\Phi)\frac{\rho_f}{\rho_p} \tag{3.14}$$

$$\frac{\sigma_f}{\sigma_p} \approx 0.2\left(\Phi\frac{\rho_f}{\rho_p}\right)^{3/2} + (1-\Phi)\left(\frac{\rho_f}{\rho_p}\right) \tag{3.15}$$

where E_f is Young's modulus of the foam; E_p is Young's modulus of the unfoamed solid; σ_f is the stress at yield of the foam; σ_p is the stress at yield of the unfoamed solid; ρ_f is the foam density; ρ_p is the unfoamed solid density; Φ is the fraction of solid in the cell struts. These two equations can be used as the mechanical properties data of conventional foams.

Engineering stress-strain curves for different foaming conditions are presented in Figure 11. The elastic modulus, tensile strength and the elongation at break of the microcellular foams are plotted on Figure 12 against the relative density. Equations (3.14) and (3.15) are plotted as dash lines. The elastic modulus of PMMA foam was found to be closely related to the relative density. The experimental data in this study fits Equation (3.14) (Φ=0.8) very well.

The curve of Equation (3.15) is close to the experimental data points in the low density region for PMMA foams while it underestimated the foam's tensile strength when the relative

density was higher than 0.5. The predicted values by Equation (3.15) are considerably lower than the experimental values. Since Equation (3.15) was based on conventional foams, which have larger cell sizes, the theoretical value underestimated the performance of microcellular foams. The theoretical values are closer to the experimental values in the low density region since generally cell sizes are larger in the low density region than in high density region. In order to predict the tensile strength of microcellular foam, an empirical formula was proposed according to the experimental data of this:

$$\frac{\sigma_f}{\sigma_p} \approx \left(\frac{\rho_f}{\rho_p}\right)^2 \tag{3.16}$$

This formula is plotted with solid lines in Figure 12. It fits the experimental data very well.

The elongation at break of foam obtained in this study generally increased with increasing the relative density, as shown in Figure 12. The curve plotted in solid line was to show the trend. It should be noted that the elongation at break for some foamed materials was greater than the unfoamed counterpart, which was different with the curves of elastic modulus and strength versus relative density. The increased elongation at break should attribute to the fact that the small cells blunted the crack tips and increased the energy required to break the material. Therefore, it is possible to find an optimized point for ductility by controlling the foaming conditions in the foaming process. We found no theoretical model in the literature to fit the experimental data of the elongation at break. Further research is required to investigate the fracture behaviors of microcellular foams.

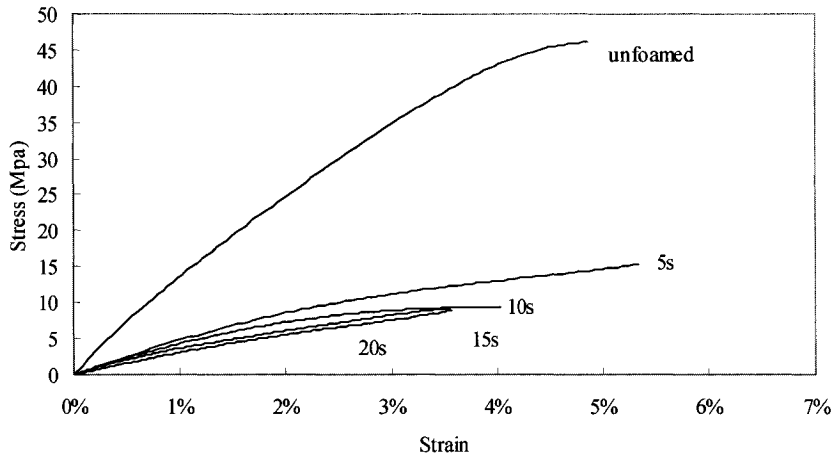

(a)

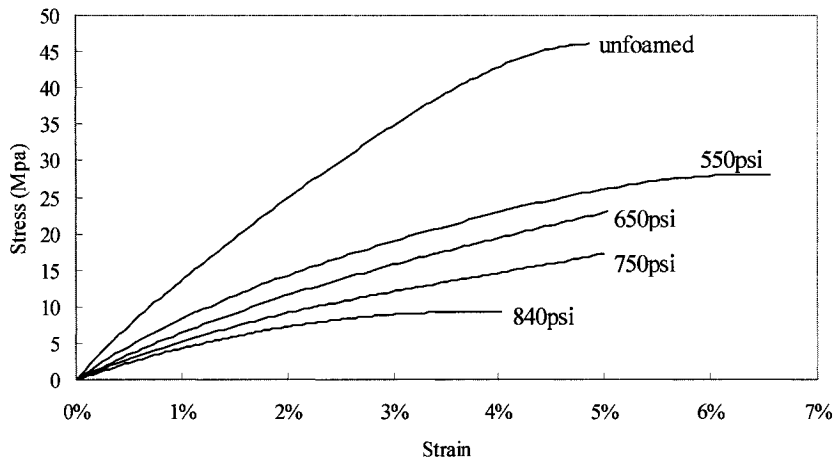

(b)

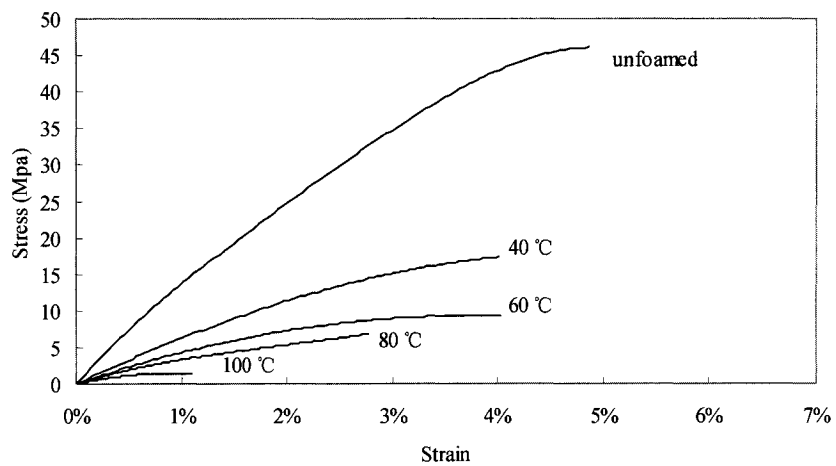

(c)

Figure 11 Engineering stress-strain curves for tensile test of PMMA foams: (a). Effect of foaming time, (b). Effect of saturation pressure, (c). Effect of foaming temperature

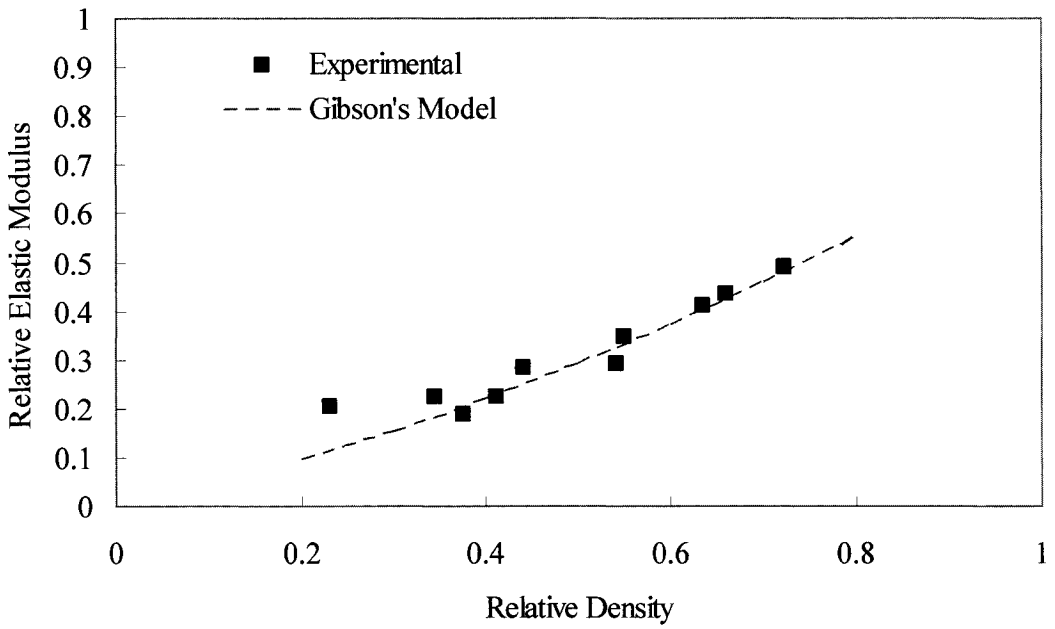
Experimental
Gibson's Model
Relative Elastic Modulus
Relative Density
0
0.1
0.2
0.3
0.4
0.5
0.6
0.7
0.8
0.9
1
0
0.2
0.4
0.6
0.8
1

(a)

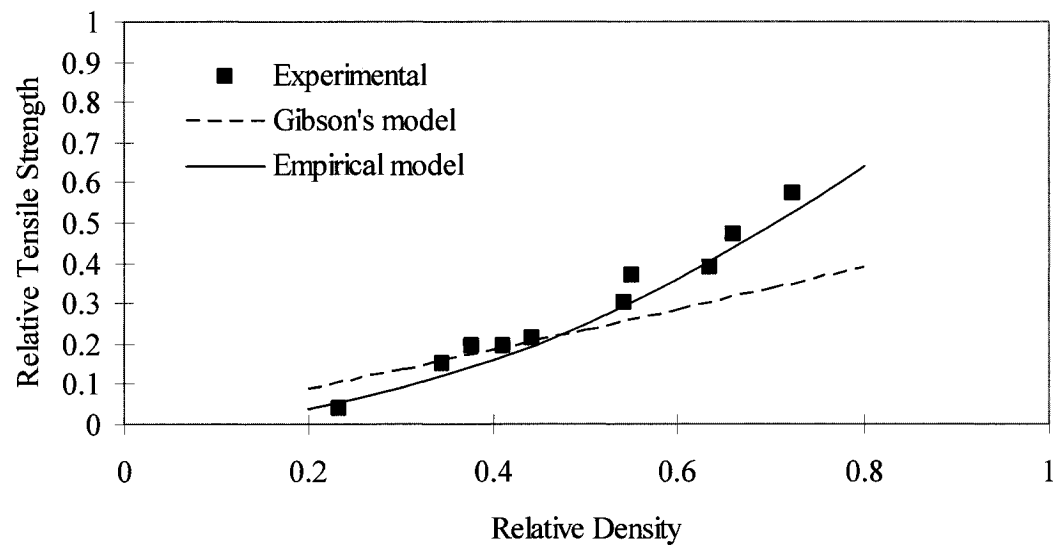
Experimental
Gibson's model
Empirical model
Relative Tensile Strength
Relative Density
0
0.1
0.2
0.3
0.4
0.5
0.6
0.7
0.8
0.9
1
0
0.2
0.4
0.6
0.8
1

(b)

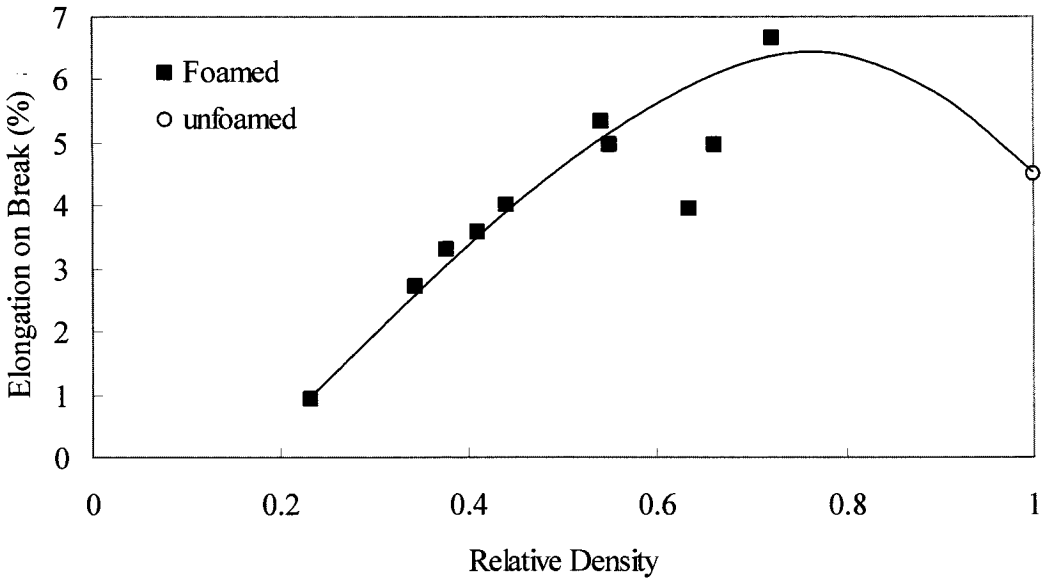

(c)

Figure 12 Plots of the mechanical properties of PMMA foams against relative density: (a). Relative elastic modulus against relative density, (b). Relative tensile strength against relative density, (c). Elongation at break against relative density

4.3.5 Mechanical Properties of the Unfoamed PMMA Nanocomposites

Representative engineering stress-strain curves for the unfoamed PMMA nanocomposites, with nano clay content of 0.5 wt. %, 1 wt. % and 2 wt. % made by solvent co-precipitation method, are presented in Figure 13 together with the stress-strain curve of pure PMMA as a reference. Figure 14 shows the average value of elastic modulus, tensile strength and the elongation at break. The error bars denote the standard deviations. For the samples with clay loading of 0.5 wt. %, the mechanical properties of the PMMA nanocomposites were enhanced significantly. The tensile strength and the elongation at break increased 54% and 97% respectively. An increase of 25% in elastic modulus was also obtained. That indicates the interacted C20A nanoclay was acting as a good reinforcement in the polymer matrix. However, the tensile mechanical properties of the PMMA nanocomposites with 1 wt. % and 2 wt. % clay load were not greatly improved. The elastic modulus dropped down gradually with increased load of nano clay. For the samples possessing 1 wt. % and 2 wt. % of Cloisite 20A, the tensile strength and the elongation at break of the PMMA nanocomposites were close to the pure PMMA samples. The decreased mechanical properties of those nanocomposites are possibly due to the excessive nano particle clay that was not well dispersed in the polymer. The agglomerated nanoclay may have created stress concentrations in the polymer matrix and therefore decreased the tensile strength and elongation at break; the poor bonding between the polymer chain and the agglomerations of the nanoclay decreased the elastic modulus.

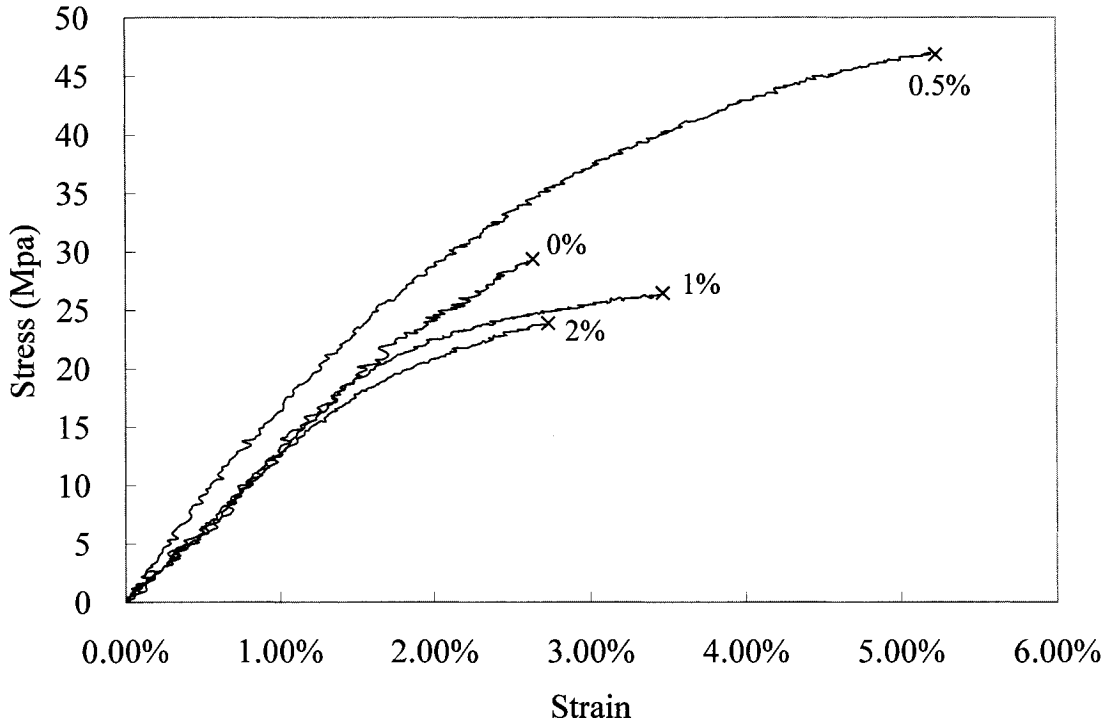

Figure 13 Engineering stress-strain curves of PMMA nanocomposite with the nanoclay content of 0.5 wt. %, 1 wt. %, 2 wt. %, and pure PMMA

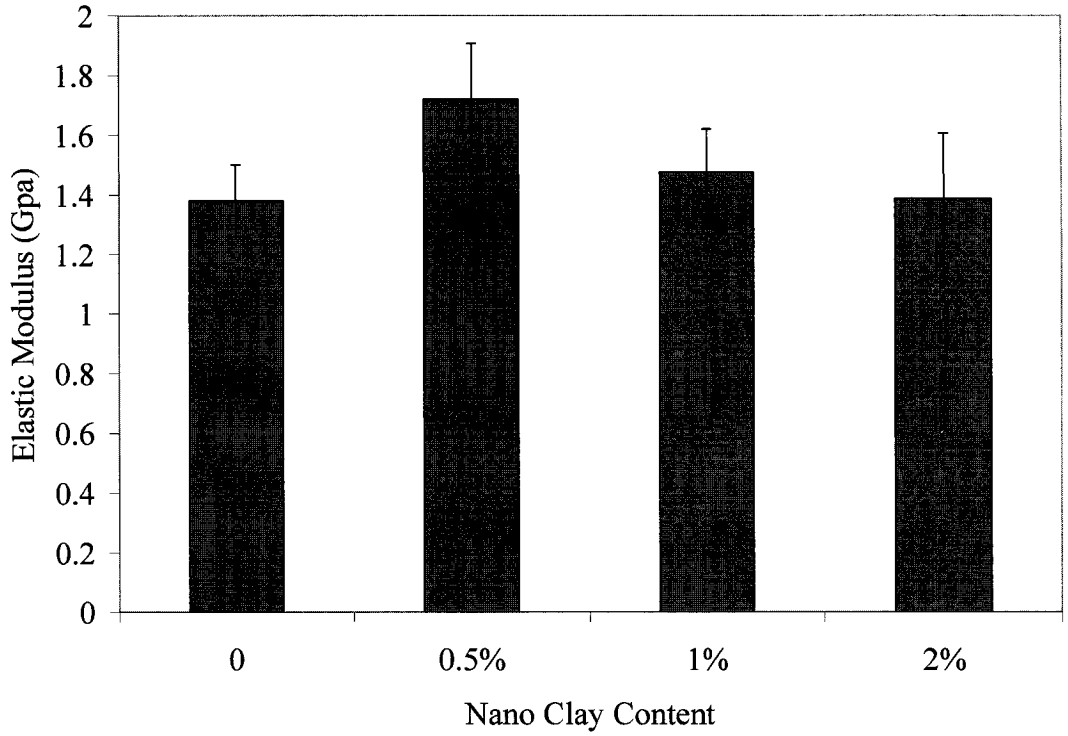
Elastic Modulus (Gpa)
2
1.8
1.6
1.4
1.2
1
0.8
0.6
0.4
0.2
0
0
0.5%
1%
2%
Nano Clay Content

(a)

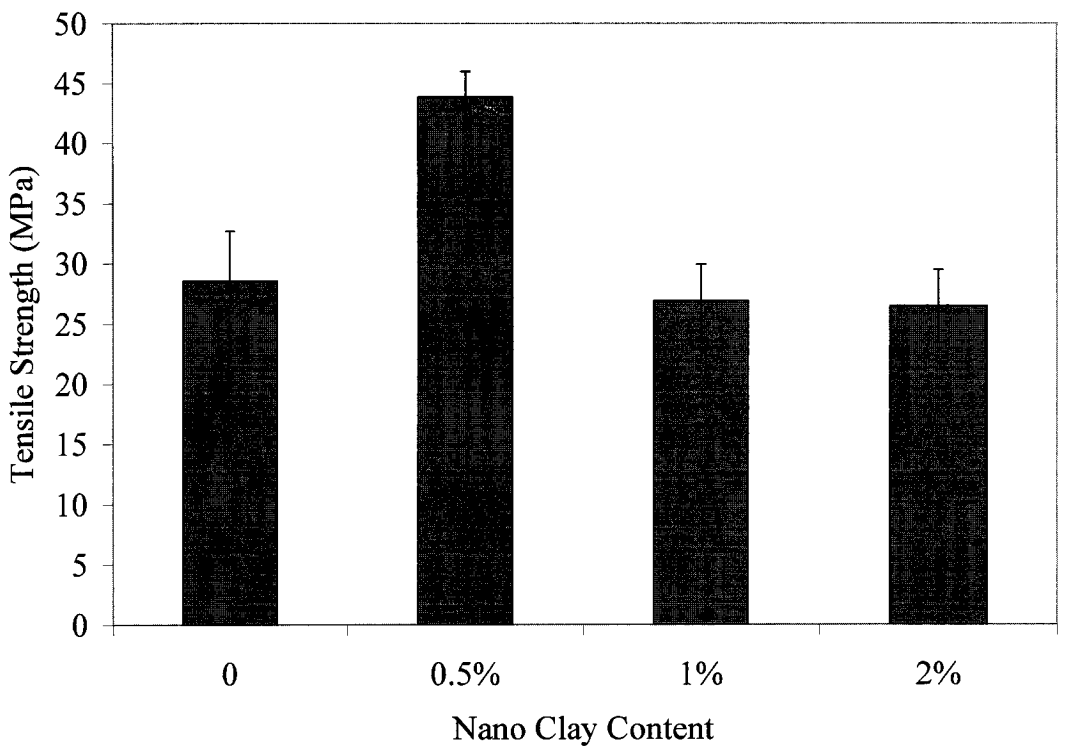
Tensile Strength (MPa)
50
45
40
35
30
25
20
15
10
5
0
0
0.5%
1%
2%
Nano Clay Content

(b)

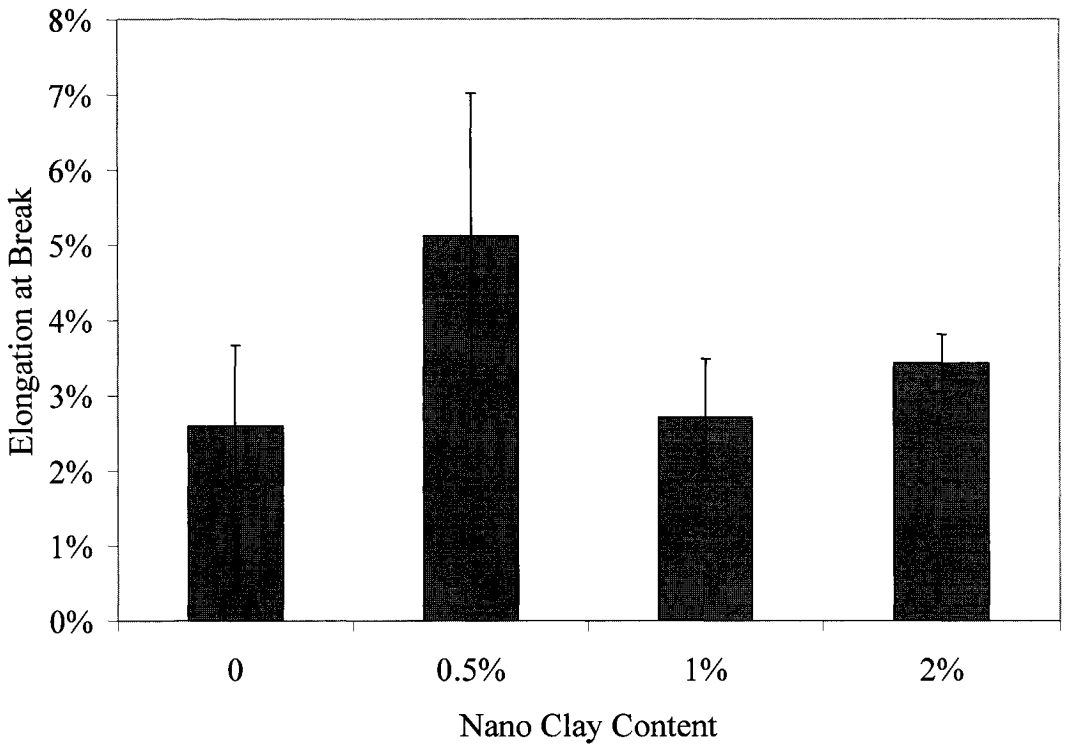

(c)

Figure 14 Mechanical properties of the PMMA nanocomposites with different nano clay content from 0 wt. % to 2 wt. %. (a) tensile elastic modulus, (b) tensile strength, (c) elongation at break

In order to confirm this hypothesis, the mechanical properties of dry blended PMMA and Cloisite 20A were examined. The dry blending method produced nanocomposites with agglomerated clay domain and poor nano clay dispersion [40]. Visually, the samples made with dry blending method were white and translucent. This was entirely different with the highly transparent samples appearing slight brown in color. The mechanical properties were deteriorated because of the existence of the nanoclay agglomeration in the polymer. As shown in Table 2, the mechanical property values of the PMMA nanocomposites made by the dry blending method were quite close to the results of the samples made by the solvent co-precipitation method with 1 wt. % and 2 wt. % nanoclay. This result supported the hypothesis that the decreased mechanical properties of the PMMA nanocomposites with 1 wt. % and 2 wt. % nanoclay, made by solvent co-precipitation method, are due to the bad dispersion of nanoclay.

Table 2: Mechanical properties of the unfoamed PMMA nanocomposite made by Solvent Co-precipitation method and Dry Blinding method

	Pure PMMA	Solvent Co-precipitation			Dry blending		
		0.50%	1%	2%	0.50%	1%	2%
Elastic modulus (GPa)	1.35	1.72	1.48	1.39	1.28	1.26	1.24
Tensile Strength (MPa)	28.54	43.84	26.88	26.45	27.40	32.09	27.94
Elongation at break	2.60%	5.12%	2.71%	3.43%	2.41%	3.33%	2.44%

4.3.6 Effect of the Nanoclay on PMMA Foaming Processing

Closed cell foams with microcellular level cell size were produced using subcritical CO_2 gas foaming. The foam morphologies of these PMMA nanocomposite foams were reported in a previous paper [40]. In this study, the mechanical properties of the PMMA nanocomposite foams with different foam densities were investigated. It was reported that the foam density relies on the processing conditions such as foaming time, foaming temperature, and saturation pressure. The density of PMMA foam decreases with increased foaming time, foaming temperature and saturation pressure [105]. The PMMA/Clay nanocomposites are expected to have a similar foaming behavior. In order to control the density of nanocomposite foams, the foaming times were selected from five to twenty seconds. Meanwhile, all the other processing conditions were fixed constants as mentioned in the experimental section.

The foam densities of the PMMA nanocomposite foams were plotted as functions of foaming time in Figure 3. The densities of nanocomposite foams, with different nanoclay content, decreased with an increased foaming time in the foaming time range of five to twenty second, as expected. For the foaming time of five seconds, the foam density decreased while increasing the load of nanoclay weight percentage. In other words, lighter material was obtained, which is generally desirable. The increased foam expansion is reasonable because the nanoclay created a large amount of heterogeneous nucleation sites and therefore increased the cell density. The foam density decreased with increased foaming time for all the samples with different nanoclay weight percentages. However, we can clearly see that the density of

nanocomposite foams with 2 wt. % nanoclay tended to be higher relative to the samples with 1 wt. % and 0.5 wt. % nanoclay with increased foaming time. The increased density of the PMMA nanocomposite with 2 wt. % nanoclay can be explained by the increased diffusivity of CO_2 gas in the nanocomposite. The diffusivity of the PMMA nanocomposite made with the solvent co-precipitation method increases with increased nanoclay content due to the low resistance path for gas transport caused by the excessive nanoclay agglomeration [101]. During the cell growth process, a relative lower diffusivity of blowing agent in the polymer matrix can maintain gas in the system for cell growth instead of diffusing it away. When the foaming time was long, the polymer-clay-gas system was running out of blowing agent. Combined with the effect of cell coalescence, the foam density increased. An attempt was undertaken to foam the PMMA nanocomposite made by the dry blending method, which have even higher diffusivity coefficient of CO_2 gas in PMMA-nanoclay matrix [101]. As shown in Table 2, for each different nanoclay load, the resultant foams had higher densities. This confirmed the explanation that the increased foam density was due to the higher CO_2 diffusivity. When the nanoclay load increased from 5 wt. % to 2 wt. %, the foam densities of the samples using the two different methods became closer because the morphology of the nanocomposite became similar.

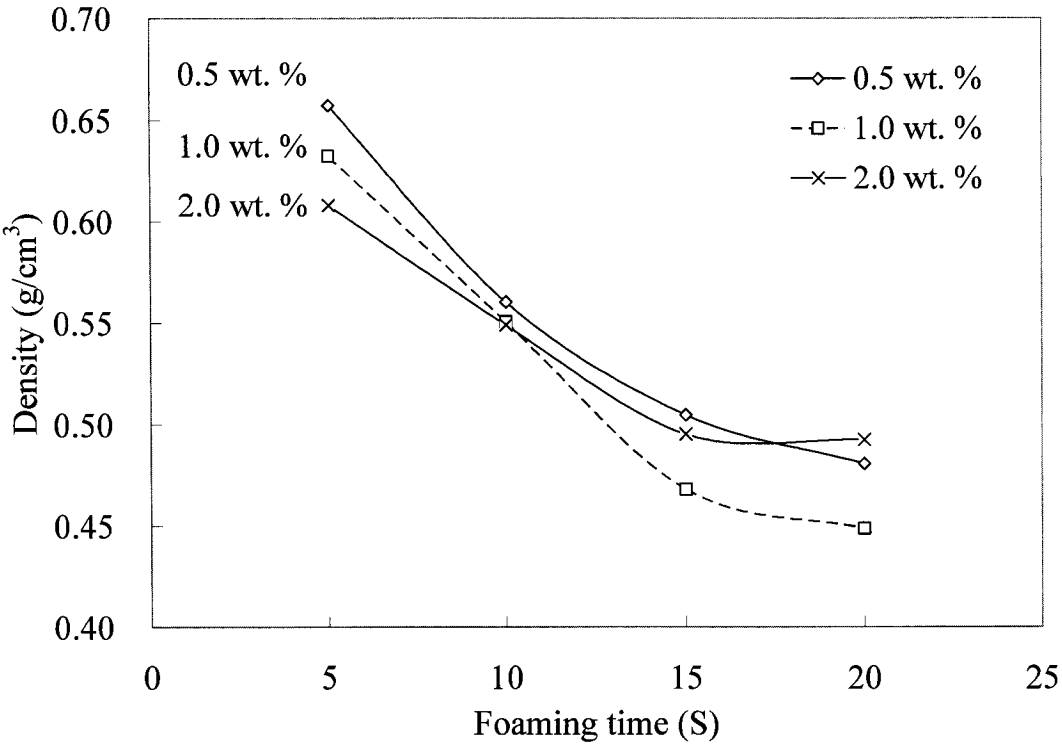

Figure 15 Foam density of PMMA nanocomposite foam as functions of foaming time with nanoclay content of 0.5 wt. %, 1.0 wt. %, and 2.0 wt. %

Table 3: Foam Density and Mechanical properties of the PMMA nanocomposite foams made by Solvent Co-precipitation method and Dry blending method. The foaming temperature was 60 °C and the foaming time was 5 seconds.

	Solvent Co-precipitation			Dry blending		
Nanoclay % wt.	0.5%	1%	2%	0.5%	1%	2%
Foam Density (g/cm^3)	0.560	0.550	0.549	0.612	0.572	0.549
Elastic Modulus (GPa)	0.46	0.35	0.29	0.33	0.33	0.32
Tensile Strength (Mpa)	12.49	5.35	5.53	7.74	6.78	7.18
Elongation	3.70%	1.70%	2.53%	2.42%	2.18%	1.97%

4.3.7 Mechanical Properties of PMMA Nanocomposite Foams

Figure 16 shows representative stress-strain curves of the PMMA nanocomposite foams processed in a 60 °C hot bath for 5 seconds. It is clear that the foam sample with 0.5 wt. % nanoclay has superior mechanical properties. In order to compare the effect of the nanoclay on the mechanical properties, the elastic modulus, the tensile strength, and the elongation at break are plotted as functions of the foam density in Figure 17. Best-fit lines for the data points were plotted by software to show the trend. The fit lines in Figure 17 indicated that the mechanical properties of the foamed material were proportional to the foam density, which are consistent with the behaviors of the pure PMMA foams [105]. The microcellular foams made of PMMA nanocomposite with 0.5 wt % exhibited an improved elastic modulus, tensile strength, and elongation at break when compared with pure PMMA foams of the same foam density. With higher nanoclay load, the elastic modulus, tensile strength, and elongation at break decreased gradually. These results are not surprising because the mechanical properties of the foam greatly depend on those of the unfoamed polymer matrix. The nanoclay reinforced the polymer matrix and therefore increased the mechanical properties of the nanocomposite foam. However, for the nanocomposite foam with higher nanoclay load, the excessive nanoclay deteriorated the modulus, strength, and ductility of the foam. It is expected that nanocomposite with less agglomeration and exfoliated morphology would produce foam materials with better mechanical properties. It is also noticed that even for the nanocomposite foam with 0.5 wt. % nanoclay load, the elastic modulus and tensile strength tend to be decreasing closely to the

pure PMMA foams in the lower relative density region. This is possibly due to the polymer-clay interfaces acting as nucleation sites during the foaming process. Once the gas bubbles started to nucleate at these spots, the bonding between the reinforced nanoclay and the polymer chain were weakened and therefore the mechanical properties of the foams tended to decrease. Furthermore, the mechanical properties of the nanocomposite foams made by the dry blending method were also observed. Unsurprisingly, they did not give significant improvement in mechanical properties for all the samples with different nanoclay content because of the inferior mechanical properties of the unfoamed composite.

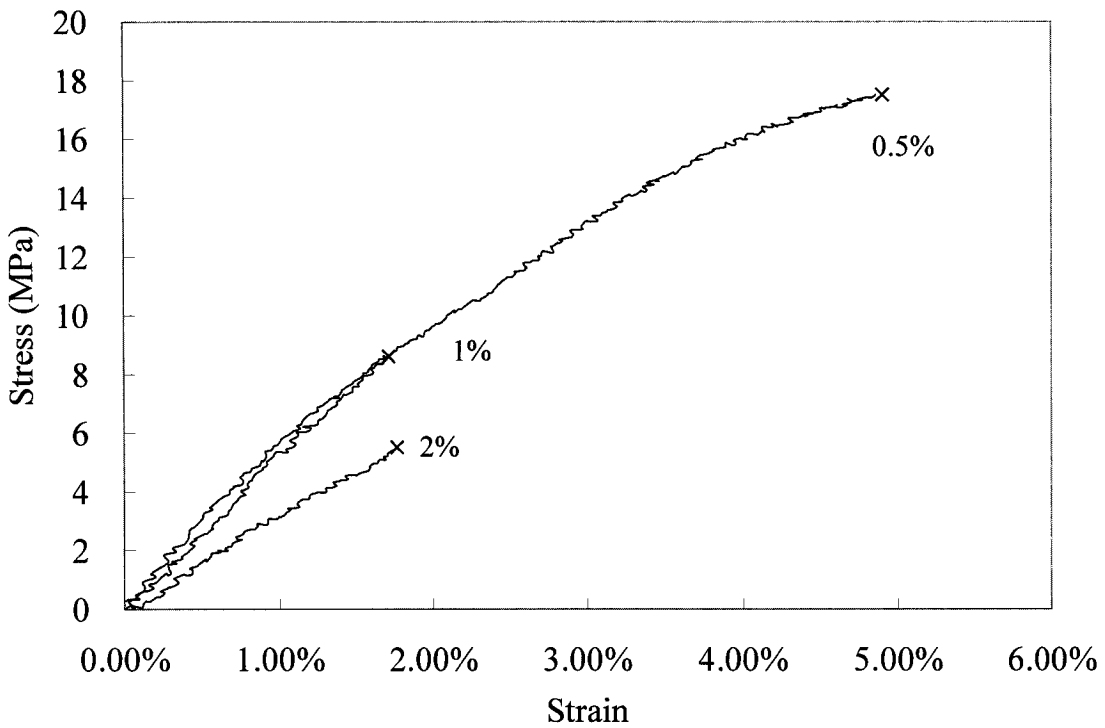

Figure 16 Engineering stress-strain curves of PMMA nanocomposite foams with C20A of 0.5 wt. %, 1 wt. %, 2 wt. %. The samples were foamed at 60 °C and for 5 seconds.

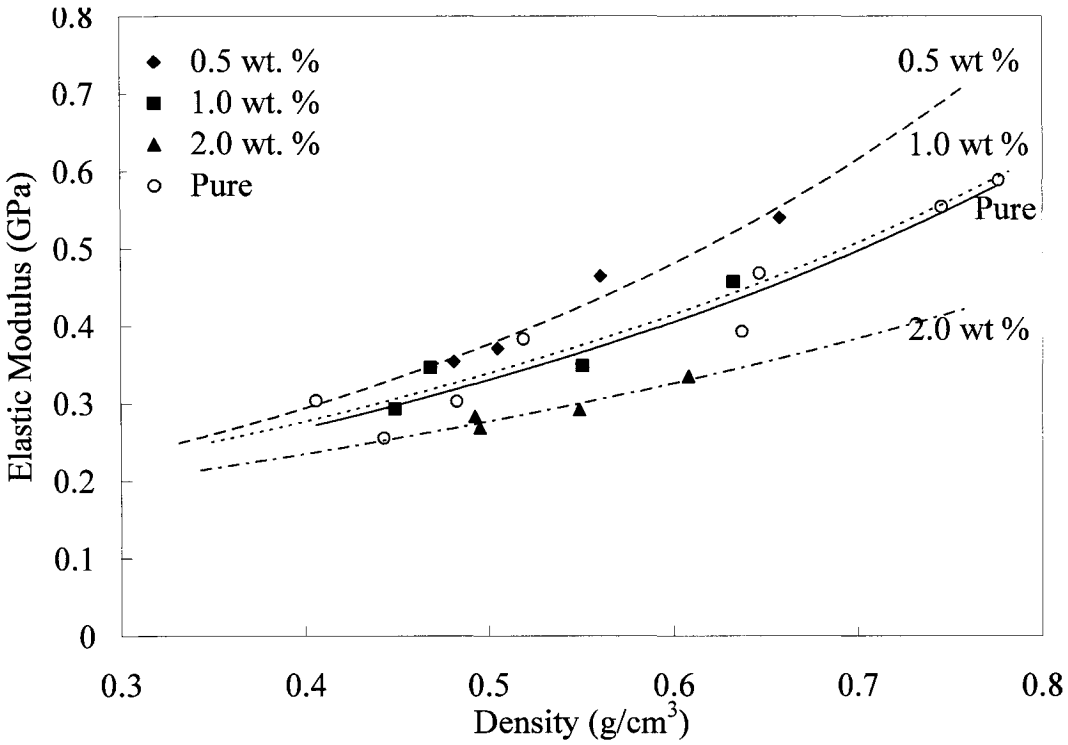
0.5 wt. %
1.0 wt. %
2.0 wt. %
Pure
0.5 wt %
1.0 wt %
Pure
2.0 wt %
Elastic Modulus (GPa)
Density (g/cm3)
0
0.1
0.2
0.3
0.4
0.5
0.6
0.7
0.8
0.3
0.4
0.5
0.6
0.7
0.8

(a)

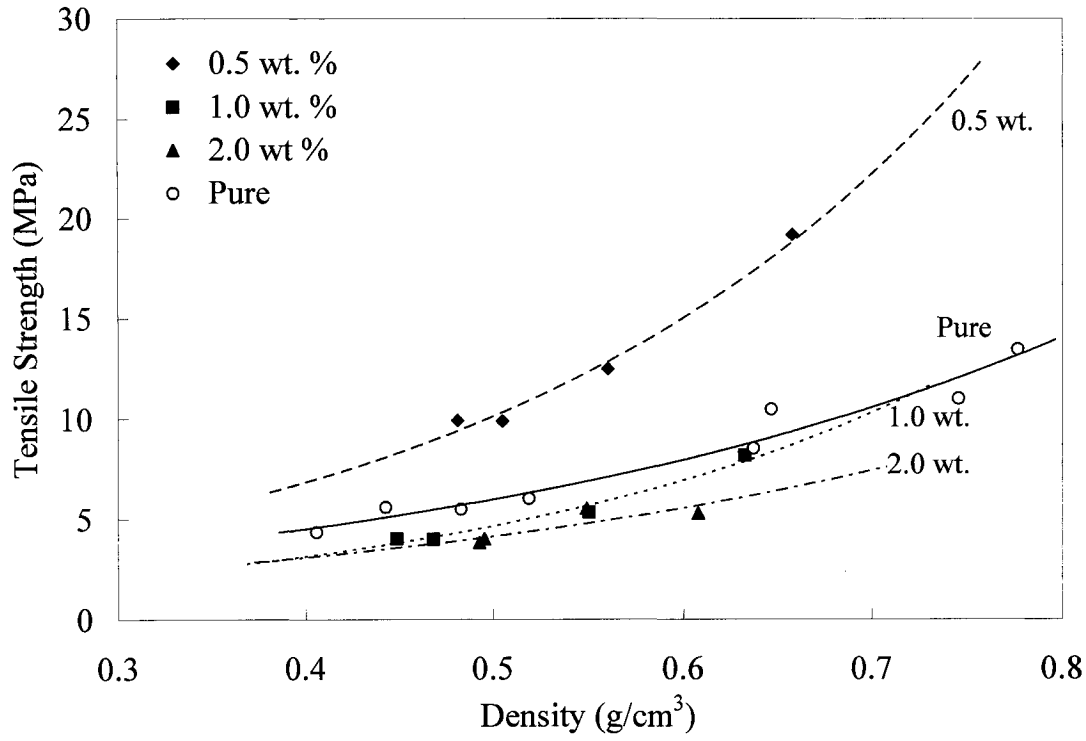
0.5 wt. %
1.0 wt. %
2.0 wt %
Pure
0.5 wt.
Pure
1.0 wt.
2.0 wt.
Tensile Strength (MPa)
Density (g/cm3)
0
5
10
15
20
25
30
0.3
0.4
0.5
0.6
0.7
0.8

(b)

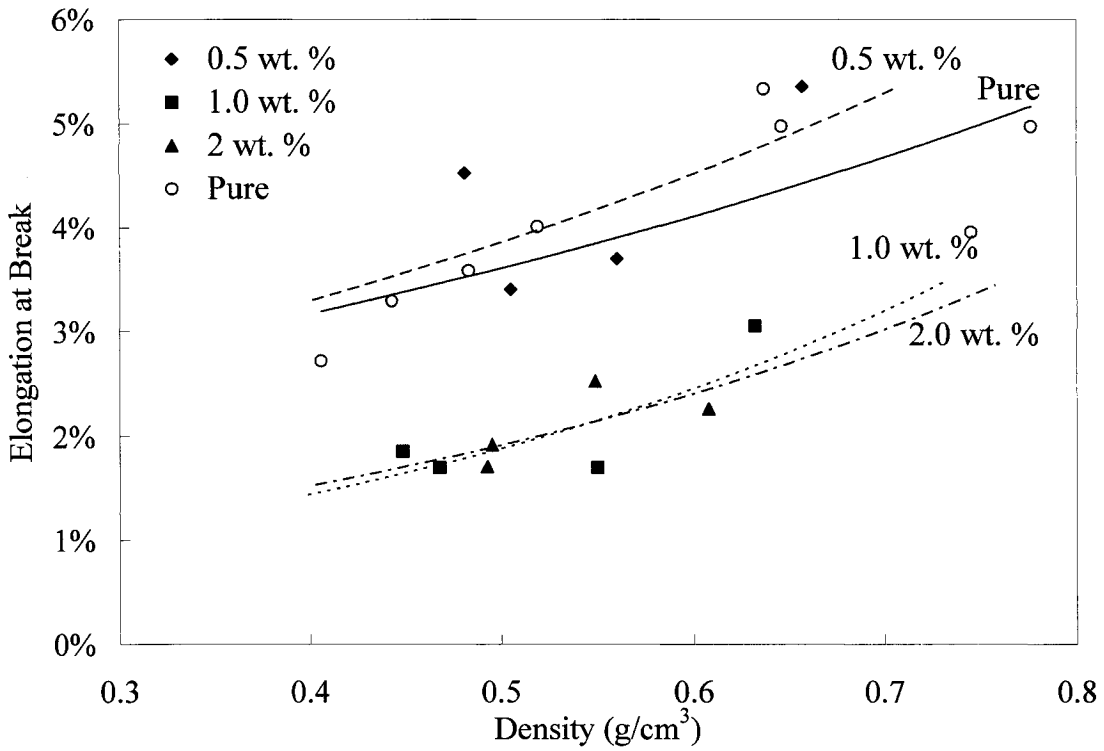

(c)

Figure 17 Mechanical properties of PMMA nanocomposite foams as functions of foam density: (a) Elastic modulus, (b) Tensile Strength, and (c) Elongation at break. The data for the pure PMMA foams were from work reported by Fu et al. [105]

4.4 Conclusions

PMMA Microcellular foams were prepared using a two stage batch method. The cell density was found to increase with a higher saturation pressure and foam temperature. When foam time was increased, the cell density initially increased and then dropped down due to cell coalescence. The average cell size increased with longer foam times and higher foam temperatures. As a consequence of the cell structure change, the density and mechanical properties of the foam changed. The mechanical properties of PMMA microcellular foams can be directly linked to the processing conditions such as foaming time, saturation pressure and foaming temperature. The elastic modulus, tensile strength and elongation at break decreased with increasing the foaming time, saturation pressure and foaming temperature.

The elastic modulus of PMMA microcellular foams is closely related to foam density and show great agreement with theoretical value. The tensile strengths of microcellular foams in this study fit the theoretical values in the low relative density region. The tensile strengths were greater than the theoretical model in a higher relative density region. These results confirm that foams with a finer cell structure have an advantage in mechanical properties against foams with a relatively coarse cell structure. For some of the foaming conditions, higher elongation at break of the microcellular PMMA foam can be obtained compared with the unfoamed PMMA.

By altering the foaming conditions, the mechanical properties of microcellular PMMA foam can be controlled. In order to get a foam material with a lower weight to reduce the cost,

some mechanical properties such as modulus, strength or ductility may decrease. Therefore, the desired combination of the material density and mechanical properties can be selected according to the application requirements by carefully selecting the foaming conditions.

PMMA-Clay nanocomposite with nanoclay load as small as 0.5 wt. %, prepared using the solvent co-precipitation method, exhibited improved mechanical properties. Comparing with neat PMMA samples, the elastic modulus increased by 25%, the tensile strength increased by 54%, and the elongation at break increased by 97%. However, the mechanical properties of PMMA nanocomposites with higher nanoclay content dropped down close to that of the samples made with the dry blending method. The increased amount of nanoclay deteriorated the mechanical properties.

The foam density is governed by the combined effect of cell nucleation, cell growth, and cell coalescence. As a nucleation agent, the nanoclay in PMMA matrices created a large amount of heterogeneous nucleation sites during subcritical CO_2 gas foaming. The heterogeneous nucleation increased the cell density and then decreased the foam density when the foaming process time was short. Another effect of nanoclay on the foaming process is an increased CO_2 diffusion coefficient in the PMMA nanocomposite. For the processes with a longer foaming time, most of the CO_2 gas diffused out of the polymer matrix because of the increased CO_2 diffusivity. As a result, the amount of gas that can be used in cell growth declined and an increased foam density was obtained. In order to greatly reduce weight and material consumption, both the nanoclay content and the foaming time should be carefully considered in processing.

The mechanical properties of the microcellular PMMA nanocomposite foams were found to be greatly dependent on the mechanical properties of the unfoamed nanocomposites. The nanocomposite foams with 0.5 wt. % nanoclay content showed optimized mechanical properties within the foam density range tested in this study. However, the improvement of mechanical properties in low density range is relatively smaller because the gas nucleation weakened the reinforcement effect of the nanoclay particles. The mechanical properties of the PMMA nanocomposite foams made by the solvent co-precipitation method showed preponderant mechanical properties than the ones made by dry blending method.

Nanoclay as a nucleation agent and reinforcement filler can be used to improve the mechanical properties of the PMMA microcellular foams. The nanoclay content and the dispersion quality acted as important parameters in foam processing together with the other processing conditions such as foaming time, foaming temperature, and saturation pressure.

Chapter 5: Processing, Characterization, and Mechanical Properties of Rotational Molded PP and LDPE Foams

5.1 Introduction

Rotational molding is becoming an increasingly important foaming process for both researchers and industries. Foamed polymer parts made with rotational molding provide a high stiffness with a reduced weight as well as a high thermal isolation. They also have the potential to be used in acoustic absorption applications. In this chapter, the rotational mold foaming process designed in Chapter 3 is applied to produce polypropylene (PP) and low density polyethylene (LDPE) foams. The effects of processing time, particle size of both the polymer and the CBAs are also investigated. Finally, the mechanical properties of the obtained fine cell polymer foams are examined using compression tests.

5.2 Experimental

5.2.1 Experimental Materials

PP (Microthene FP800-00) supplied by Equistar was selected for the rotational mold foaming experiments. It was supplied in a powder form. The average particle size was 20 μm and the particle size distribution was 5 – 50 μm. Pelleted polypropylene Pro-Fax PF814 was supplied by Basell Polyolefins. LDPE Sclair 31E pellets were supplied by Nova Chemicals.

The chemical blowing agents (CBAs) selected for rotational mold foaming are Celogen

AZ2992 (Azodicarbonamide) and Celogen OT (p,p'-oxybis(benzenesulfonylhydrazide)) supplied by Crompton. The Celogen AZ2992 is a yellow to yellow-orange powder with an average particle size of 2 – 12 μm. Its decomposition temperature is 205-213 °C and the gas evolution rate is 210 – 220 cm^3/g. The Celogen OT is a white powder with a decomposition temperature of 160 °C and a gas evolution rate of 120-125 cm^3/g. In order to study the effect of the particle size of the CBAs, a pellet form blowing agent Endex ABC 2750 supplied by Endex International was used. The process temperature of Endex ABC 2750 is 148 – 315 °C according to the manufacturer.

5.2.2 Foam Processing

Rotational mold foaming, as described in Chapter 3, was used to process PP and LDPE foams. During the process, the oven was preheated to a temperature beyond both the melting temperature and decomposition temperature. A pre-calculated amount of polymer and CBA were mixed together and charged in the mold. Afterwards, the mold was closed and fixed to the hollow shaft. The mold was then inserted into the oven by pushing the movable worktable, and the power supply of the DC motor was activated to drive the rotation of the mold. The speed of rotation was controlled by adjusting the voltage of the power supply of DC motor. With the increase in temperature inside the mold, the polymer began to melt and a uniform mixture of polymer and CBA was obtained. The temperature inside the mold continued to increase, and the CBA began to decompose when the temperature was higher than the decomposition temperature. The gas generated by the CBA

was the nucleation site of bubbles. As the CBA kept decomposing, the bubbles grew and some of them met each other. The generated gas increased the pressure in the melted polymer. Because of the vent hole, the rotational foaming was operated in atmospheric pressure. The difference in pressure was the driving force of the cell growth. The foaming time was carefully selected in order to balance a good expansion and avoid cell coalescence. After the material was fully expanded, the mold was then removed from the oven and cooled using cold water. After the material inside the mold was fully cooled, the mold was opened and the foamed part was taken out.

The blowing agent used for PP was Celogen AZ2992 and the blowing agent used for LDPE was Celogen OT, due to the different melting temperatures of PP and LDPE. In order to study the effect of the particle size of CBAs, Endex ABC 2750 in pellet form was used together with LDPE. The oven temperature was 450 °C and the rotational speed was 36 rpm. The processing time used to process the PP foam ranged between 35 -55 minutes; the processing time used to process LDPE foam was 35 minutes. In order to obtain foams with two times expansion, the weight of the polymer samples loaded in the mold was half the solid weight of the same volume of polymer material. CBAs were premixed with the polymer particles. The calculations of the amounts of the polymer and CBAs are presented in the Appendix B.

5.2.3 Mechanical Testing

The cell structure of these foams was characterized using an optical microscope, and digital images were taken using a digital microscope eyepiece and a scanner. ImageJ software from the National Institutes of Health (NIH) in the U.S. was used to analyze the cell structure.

The mechanical properties of the porous materials were evaluated with a compression test using an Instron 4482 machine with a 100 KN load cell at room temperature. The samples were cut into circular disks with a thickness of 12 mm. The sample surfaces were smoothed using a fine grade file before testing. The strain rate of testing was 5.0 mm/min and the strain was calculated from the displacement of the crosshead. Five specimens were prepared and tested for each different test.

5.3 Results and Discussions

5.3.1 The Effect of Processing Time on the Foam Morphology

Polypropylene foams were successfully produced using the rotational mold foaming setup. The geometry of the foams was cylindrical, which is the same form as the inner surface of the mold. The cross-sections of the samples are shown in Figure 18. The samples in Figure 18 were made of Microthene FP800-00 PP and the blowing agent used was Celogen AZ2992. Both the PP and the CBA were in powder form. In Figure 18, picture (a) was taken of a sample with a processing time of 35 minutes; picture (b) was taken of a

sample with a processing time of 45 minutes and a sample processed in the rotational mold machine for 55 minutes is depicted in picture (c). All the other processing parameters were kept the same.

The sample with processing time of 35 minutes was hollow inside. The sample processed for 45 and 55 minutes comprise fully filled foam structure, as shown in Figure 18. As discussed in previous sections, the foam cell nucleation and cell growth in the mold start when the chemical blowing agent decomposition begins. The expansion of the polymer totally depends on the gas generated when the CBA decomposes. Figure 4 showed a temperature curve inside the mold as a function of time. The temperature inside the mold was higher than the start decomposition temperature only a certain time t after the processing started. Therefore, the actual foaming time is the processing time minus t. When the foaming time was short, the blowing agent was not fully decomposed and the foam was just partially expanded. If the samples were cooled down and taken out before the foam fully expanded, they were termed under-foamed.

In all the three pictures of Figure 18, it can be noticed that the cell sizes in the outer sections are larger than the ones in the inner sections. The statistical cell sizes for the three samples are presented in Figure 19. For the under-foamed sample shown in picture (a), a very fine cell structure was observed near the inner surface of the hollow portion. In picture (b), the cell structure near the center of the samples is also good. However, in picture (c), the cell sizes of near the center of the samples are much bigger. The cell sizes near the outer surface of all the three samples are bigger than the cell sized inside. This can be explained by

the heat transfer behavior in the mold. During the process, the heat is transferred from the mold to the samples, from outside to the inside. Therefore, cell nucleation and cell growth near the outer edge of the samples starts earlier than at the inside of the samples. Consequently, the actual foaming time of the outside of the sample is longer than the inside samples. Also, the temperature near the mold wall is always higher than that in the middle. The lower viscosity and increased activity due to the high temperature also promotes cell growth and cell coalescence. A longer foaming time and a higher temperature results in a relatively coarse cell structure, which is true for both gas foaming and rotational foaming, because of cell growth and cell coalescence.

Generally, a fine cell structure is desired for better mechanical properties and thermal isolation properties. The foaming time must be regulated to avoid coarse foam structures. Thus, comparing the three different types of samples, the samples processed for 45 minutes have an optimized structure and are called well-foamed. The samples processed for 55 minutes have a relatively coarser cell sizes. Therefore, they were designated as over-foamed samples.

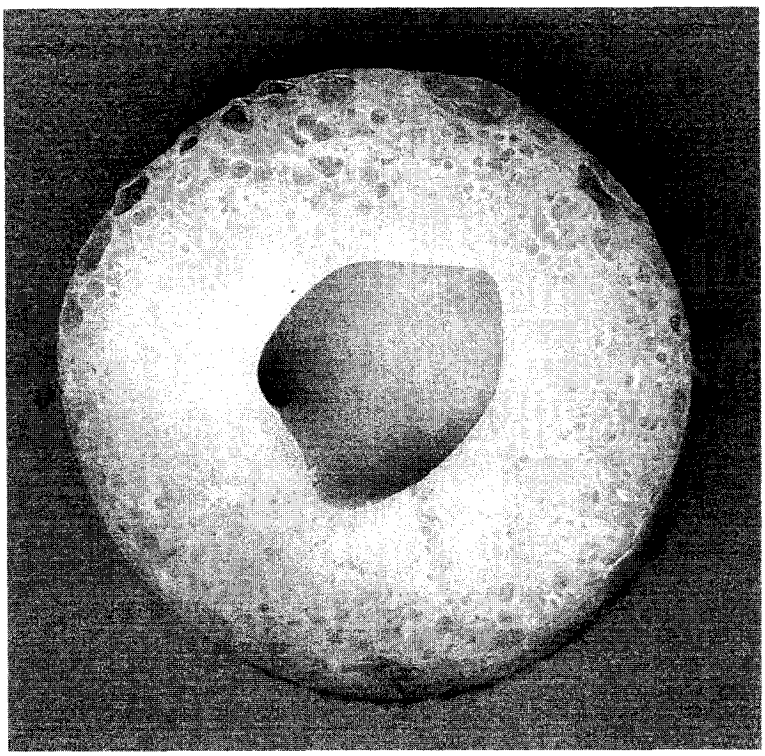

(a)

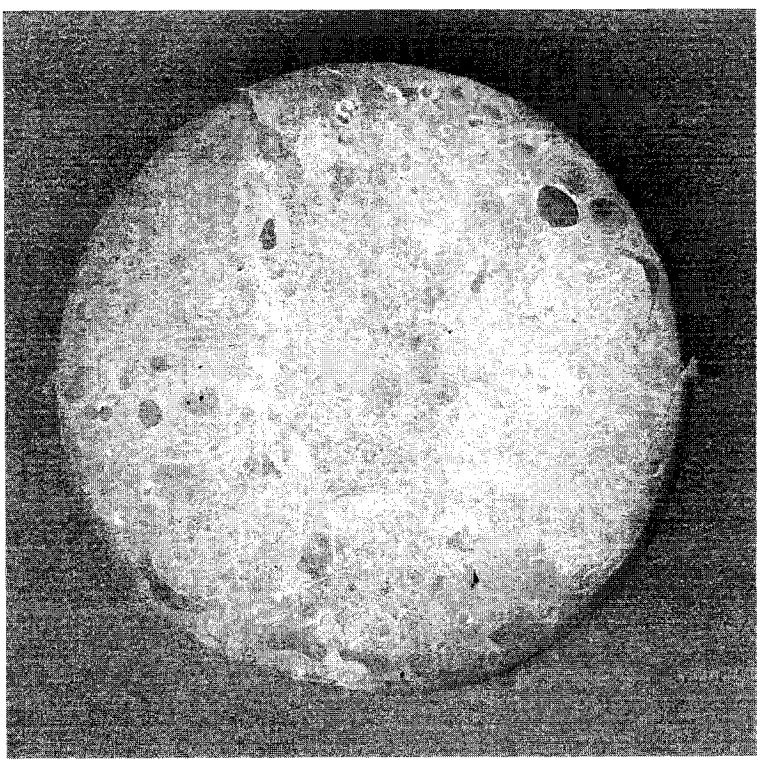

(b)

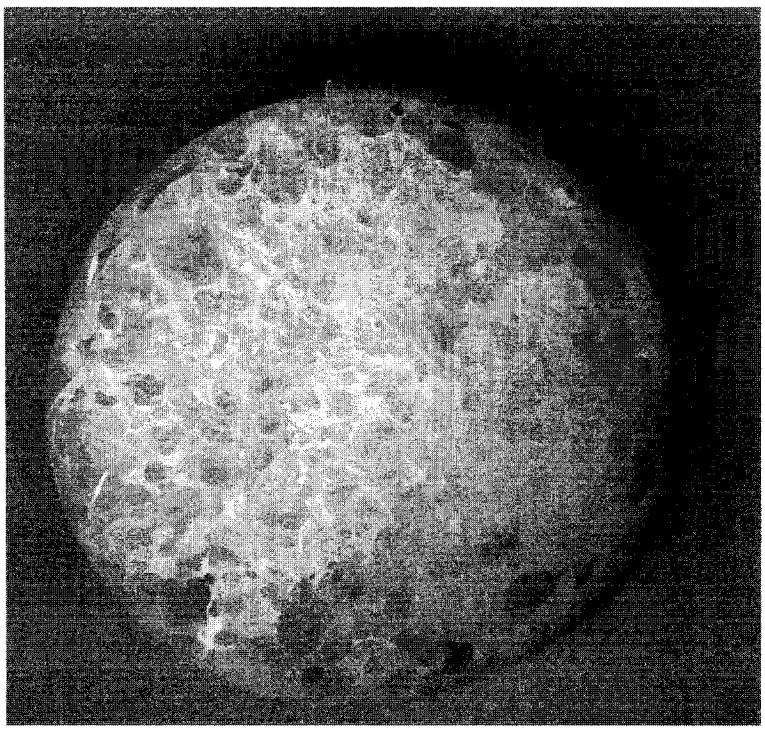

(c)

Figure 18 PP foam produced by rotational mold foaming process: (a) under-foamed, (b) well-foamed and (c) over-foamed.

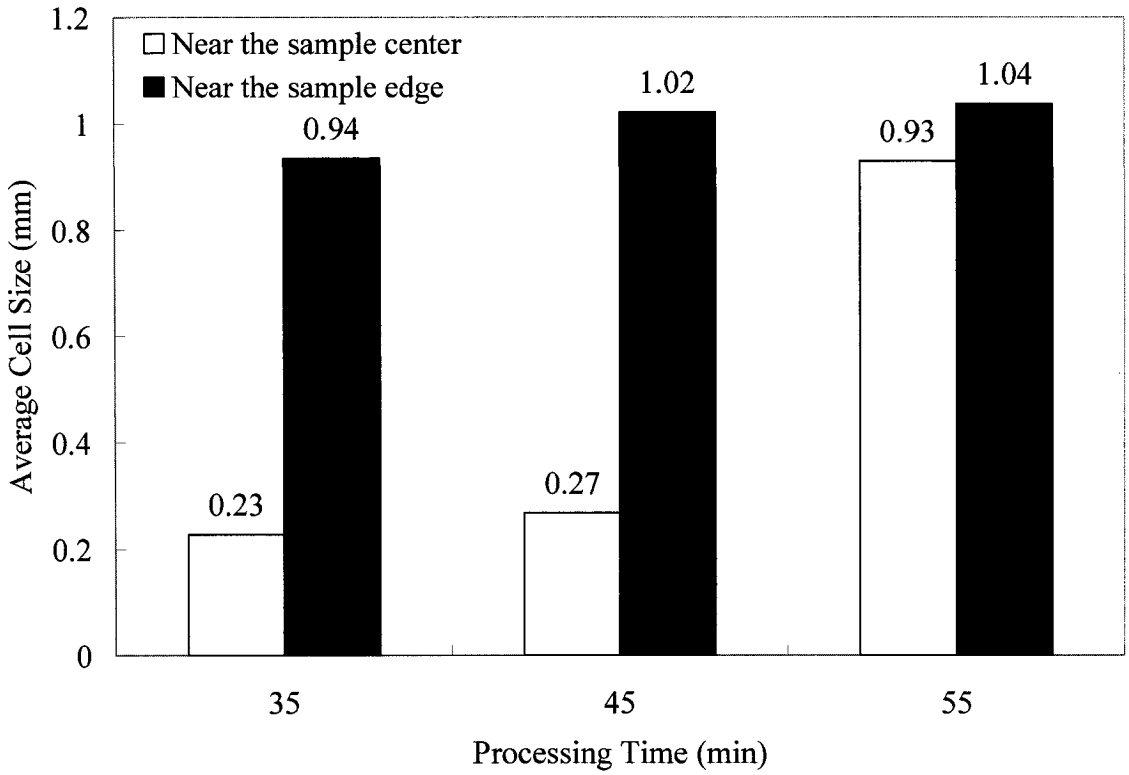

Figure 19 Average cell sizes of the PP foams made with rotational molding

5.3.2 Effects of the Particle Sizes on the Foam Morphology

The formation of a uniform polymer/CBA solution is very crucial for the uniformity of the foam structure. In order to study the effect of the particle size of polymers, both PP (PF814) and LDPE (31E) in pellet form were used in rotational mold foaming. The CBA selected for the PP was Celogen AZ2992 and the CBA for the LDPE was Celogen OT because its lower decomposing temperature matched better with the melting temperature of the LDPE. Both of these CBAs were in powder form. Since the processing temperature of the LDPE and its CBA was lower, the required processing time was shorter. The processing time for the LDPE was 30 minutes, whereas the processing time for the PP was 45 minute. All the other processing conditions were the same, as described in experimental section.

The foam made of pelleted PP exhibited a fully filled foam structure. However, the cell structure of the foam was quite coarse and non-uniform. The average cell size was greater than 1 mm. On the other hand, the foam made from pelleted LDPE exhibited a relatively fine and uniform cell structure with an average cell size on the order of 100 -300 μm. The reason for this difference is mainly due to the different melt viscosity. The melt flow rate of PF 814 PP is 2.49 g/10 min and the melt flow rate of 31E LDPE is 11.5 g/10 min according to the specification sheets of the manufacture. For the polymers with higher melt flow rates, which have lower viscosity when they were melted, the CBA powder was relatively easily mixed with the melted polymer and formed a good polymer/CBA solution. Since the rotational

angular speed was slow, the shear stress in the melted polymer was also low. As a result, the CBA powder could not enter melted polymers with lower melt flow rates, which generally have higher viscosity when they are melted, and therefore the mixture of the CBA and polymer was not uniform. This directly resulted in a non-uniform foam structure. Therefore, a fine powder form polymer is suggested for processing foams using rotational molding process if polymers with low melt flow index are used.

Pellet form CBA was also used to examine the effect of the particle sizes. Using 31E LDPE and Endex ABC 2750 CBA in pellet form without grinding, foaming experiments were conducted with the rotational foaming setup. The results were compared with the samples made from 31E LDPE and powder form Celogen OT. In both cases, the processing time was 30 minutes, the oven temperature was 450 °C and the rotational speed was 36 rpm. As shown in Figure 20 (b), the pellet form CBA failed to generate a uniform foam structure. Although some small cells were observed, some large bubbles in the foam were found. Again, the non-uniformity was due to the fact that the mixture of polymer and CBA was of poor quality. Therefore, CBAs in a fine powder form are always recommended to obtain a fine, uniform foam structure.

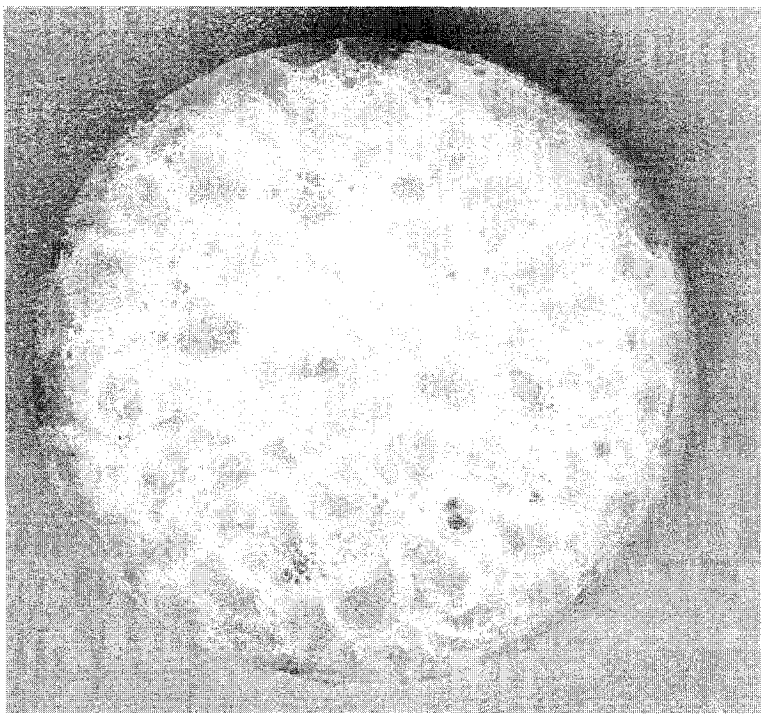

(a)

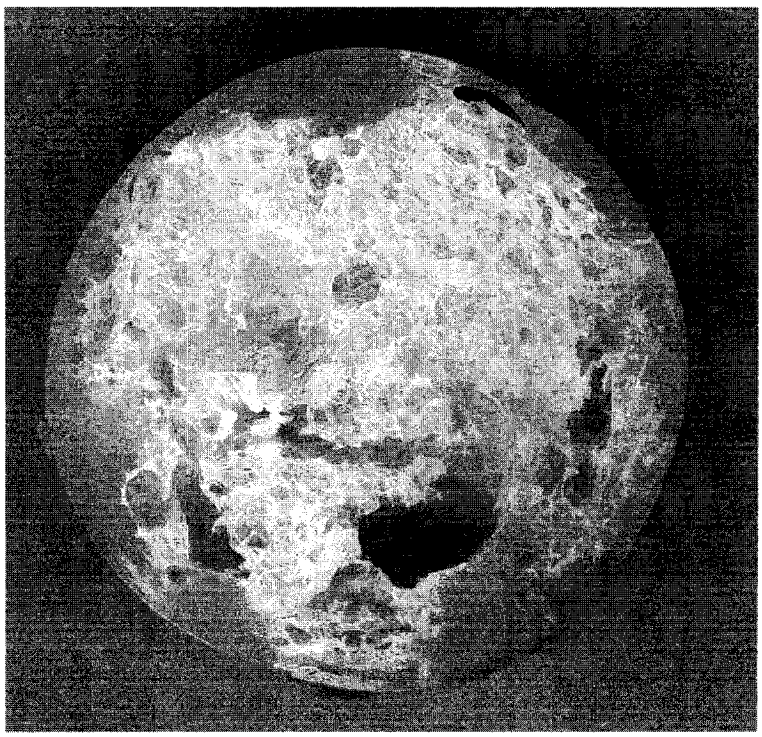

(b)

Figure 20 LDPE foams produced with rotational molding: (a) powder form CBA, and (b) pellet form CBA

5.3.3 Mechanical Properties

The typical engineering stress-strain curves of the LDPE and PP foams are presented in Figure 21. In order to make a fair comparison, the selected foam samples have the same density of 0.45 g/cm^3. As a reference, the compression stress-strain curve of microcellular PMMA foam with same density is also plotted in Figure 21.

The stress-strain curve of PP foam, which is quite similar to the curve of PMMA foam, shows three regions: the linear elasticity region, the plateau region and the densification region. In the linear region, the cell walls are subject to bending and stretching. The deformation response of the cell wall is also linear or close to linear. In the plateau region, the cells are collapsing due to the yielding or breaking of the cell walls. The stress increased slowly while the strain was increasing in this region. Finally in the densification region, the cell walls are contacted to each other and becoming rather solid. Therefore, the slope of the curve is much higher than the initial linear elasticity region and close to the solid PP modulus.

The plateau region presented in Figure 21 is very significant for energy absorption applications. The area under the curve represents the energy absorption capacity, which is commonly noted as toughness. The elongation at break of the solid PP used in this experiment was 15% according to the specification sheet of the manufacture. Although the modulus of pure PP is higher, its toughness is limited by its small elongation at break. However, the PP foam was in the plateau region when the strain is 15%. It started to be

densified at a strain of approximately 50%. Obviously, the toughness of PP foam is much higher than that of pure PP. The reason for the improvement of the energy absorption capacity is the progressively collapsing dissipation of a large amount of energy under the compression deformation. It should be noted that the improved energy absorption capacity is accompanied by a weight reduction of the material, which is of great significance to automobile and airspace applications.

No plateau region was observed in the stress-strain of LDPE foam. The linear elastic region ended when the strain was about 60% and was immediately followed by a densification region. As described before, the plateau of the brittle polymer foams and the plastic polymer foams were induced by the yielding or breaking of the cell wall. However, the LDPE material used in this study was very ductile. The elongation at break of the LDPE was as long as 725%. That means that the PP material was still in the elastic region before the densification region and that there was no cell wall yielding or breaking during the mechanical test. Therefore, the improvement in the energy absorption capacity of the LDPE foam material was limited.

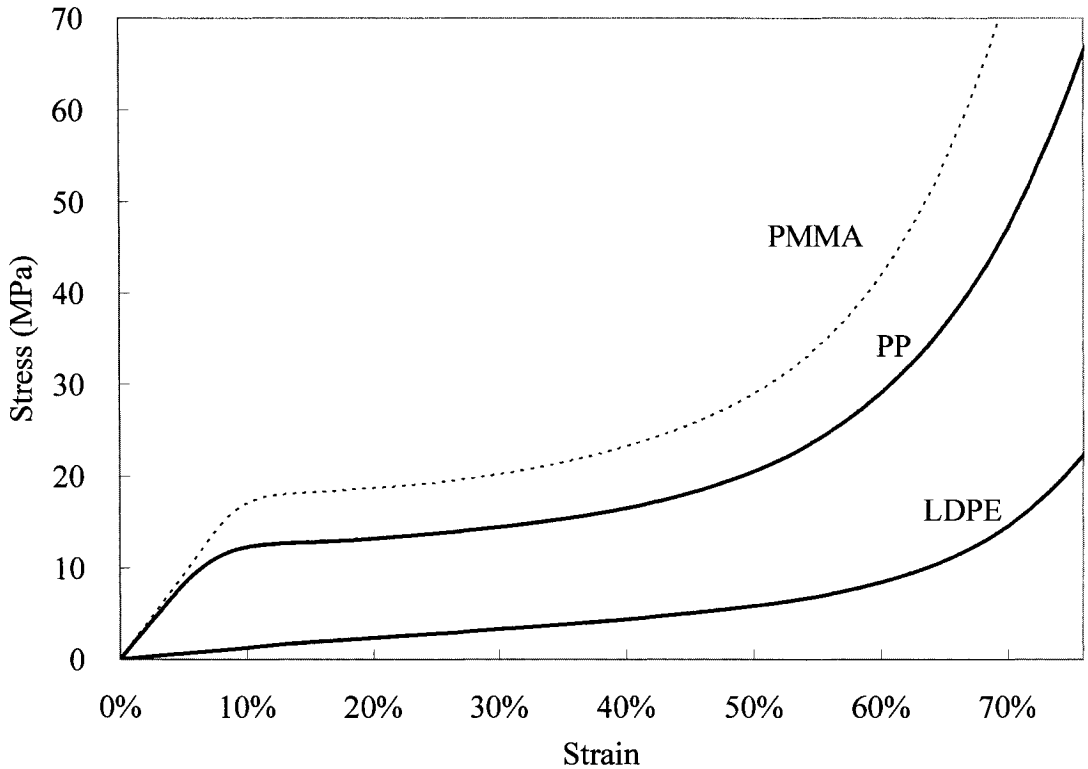

Figure 21 Stress-Strain curve of the LDPE and PP foam produced with rotational molding

5.4 Conclusions

Fine cell PP and LDPE foams were successfully produced using a rotational mold foaming process. The processing time, the size of the polymer and CBA particles and the melt flow rate were found to be the most parameters to be carefully controlled during the process.

A processing time that is too short results in under-foamed parts, which have a hollow portion inside. Conversely, a processing time that is too long causes over-foamed parts, which have a relatively coarse foam structure. A well-selected processing time can produce fully filled foam parts with fine, uniform cell structures inside. The cell sizes near the outside surface of the parts are larger then those that near the core because of the longer actual foaming times and higher temperature near the edge. Fine CBA particles are always recommended for rotational mold foaming in order to produce a fine and uniform cell structure. For the polymers that have a high viscosity when they are melted, a fine powder form polymer is required. On the other hand, for polymers that have a low viscosity when they are melted, the pellet form polymer particles can be directly used in rotational mold foaming.

The mechanical properties of the foams produced from rotational molding were examined in a compression test. The stress-strain curve of PP foam, which was made of a relatively brittle material, shows a plateau region because of the cell wall yielding or breaking. By contrast, the stress-strain curve of LDPE foam, which was made of a ductile

material, has only a linear elastic region and densification region without a plateau. The plateau region of such foams can be used in energy absorption applications. This result implies that the energy absorption capacity of brittle material can be improved by foaming the material. Most human-made or natural materials with a high modulus are relatively brittle which limits their toughness. This type of material can be converted into relatively "ductile" materials through a foaming process to obtain superior energy absorption propertes.

Chapter 6: Processing, Characterization, and Acoustic Properties of Opened Cell PMMA Foam

6.1 Introduction

Opened or partially opened cell porous materials such as urethane/polyurethane foams, glass wool, fibers are commonly used for sound absorption and transmission control. They can be used to absorb airborne noise or to optimize the transmission loss and damping in multilayer systems. It is well known that the microstructure of a material is a result of the processing parameter set during the fabrication of the material. Consequently, if one wants to efficiently optimize sound absorption for a given porous material, the most important manufacturing process parameters responsible for the micro-structural properties of the material involved in the acoustic absorption must be controlled. To do so successfully, the connections between the processing parameters, their effects on the micro-structure and sound absorption indicators such as sound absorption coefficient must be investigated and understood. It is necessary to know which different processing parameters have what kind and degree of influence on the microstructure of the material, and in turn on the macroscopic parameters involved in the acoustic performance of the material.

In this chapter, the effects of processing parameters on sound absorption performance of polymeric open cell PMMA foams are investigated. This work presents a processing technology to manufacture open-cell PMMA materials for acoustic applications using a gas

foaming/particulate leaching method and a constrained foam molding process. A parametric study is conducted by altering the processing parameters such as foaming temperature, size and percentage of foaming agent which affect the cell morphologies and consequently determine the macroscopic properties controlling the acoustical efficiency of the material. The acoustic performance is then controlled by adjusting the processing parameters with respect to the inner structure of the material.

6.2 Experimental

6.2.1 Materials

Poly(methyl-methacrylate) (PMMA) with a M_w=108,500 and M_n=56,700 was supplied by Canus Plastics. The samples were dried at a temperature of 90 °C for at least 24 hours in vacuum oven before usage. NaCl was supplied by Fisher Scientific. The blowing agent used was carbon dioxide obtained from Praxair, Inc.

6.2.2 Processing Opened Cell Acoustic Foam

Microcellular PMMA foams were processed in a two stage batch process in a prior study [105]. Because of the closed cell structure and the integral skin of the foam samples made with this method, their acoustic absorption performances were poor. A gas-foaming/particulate leaching method was then used to make open-cell foam for acoustic applications as shown in Figure 22. The strategy adopted here to produce the opened cell structure is termed the Inhomogeneous Domains strategy. It is achieved by introducing salt (NaCl) particles into the

polymer domain (PMMA) to promote open cell mechanism. Some of the process parameters were determined based on the results of the two stage batch process [105].

PMMA pellets were ground into small granules using a grinder (Bel-Art Scienceware MicroMill grinder) and sieved to a diameter of less than 250 μm. NaCl was sieved to various diameter ranges for different experiments. The PMMA and NaCl were then mixed together evenly in weight ratios varying from 70:30 to 90:10. The mixture was compression molded into 1.5 mm thick panels with a hydraulic heated press machine from Caver Inc for 4 minutes using 5 tons of force. The temperature of the hot pressing plates was 180 °C. The dimensions of the samples were 58 mm × 160 mm. The obtained samples were foamed using a three step batch process as shown in Figure 23. In the first stage, the polymer samples were saturated in a highly pressurized CO_2 chamber at a pressure of 5.7 MPa and at room temperature for 3 days. In the second stage, a constrained mold foaming process was employed in order to produce big enough samples with a good surface finish to fit the acoustic test machine. The saturated samples were foamed using a hydraulic heated press. A mold with a thickness of 4.5 mm and a dimension of 60mm × 180mm was preheated in the hydraulic heated press machine before use. The saturated samples were foamed in the preheated mold using the hydraulic press machine. The temperatures of the hydraulic heated press machine were 60 °C, 80 °C, 100 °C respectively for different experiments. Finally, the samples were taken out of the heated press machine after they were cooled down to room temperature. The thickness of the foamed samples varied from 2.2 mm to 3.5 mm. The foamed samples were then leached in water to remove the NaCl. The leaching solution was changed several times during the leaching

procedure. An $AgNO_3$ solution was used to evaluate the leaching procedure taking advantage of the fact that Cl^- ion in the water generates white precipitate with the present of Ag^+ ion. If no white precipitate was observed when the $AgNO_3$ solution was dropped into the leaching solution sample, the foamed samples were considered to be completely leached.

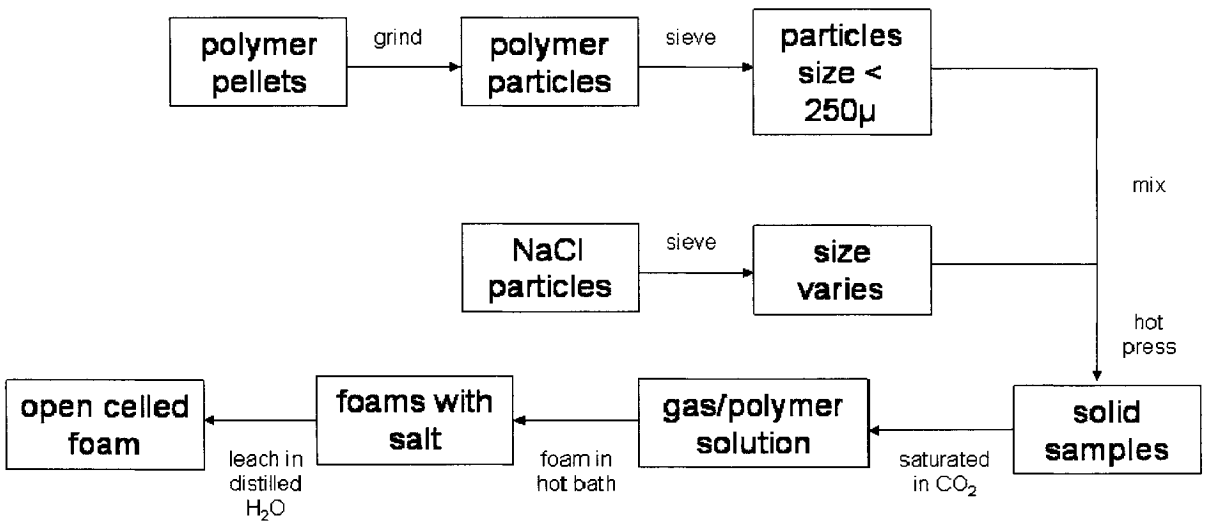

Figure 22 Schematic of the gas-foaming/particulate leaching method for opened cell foam process.

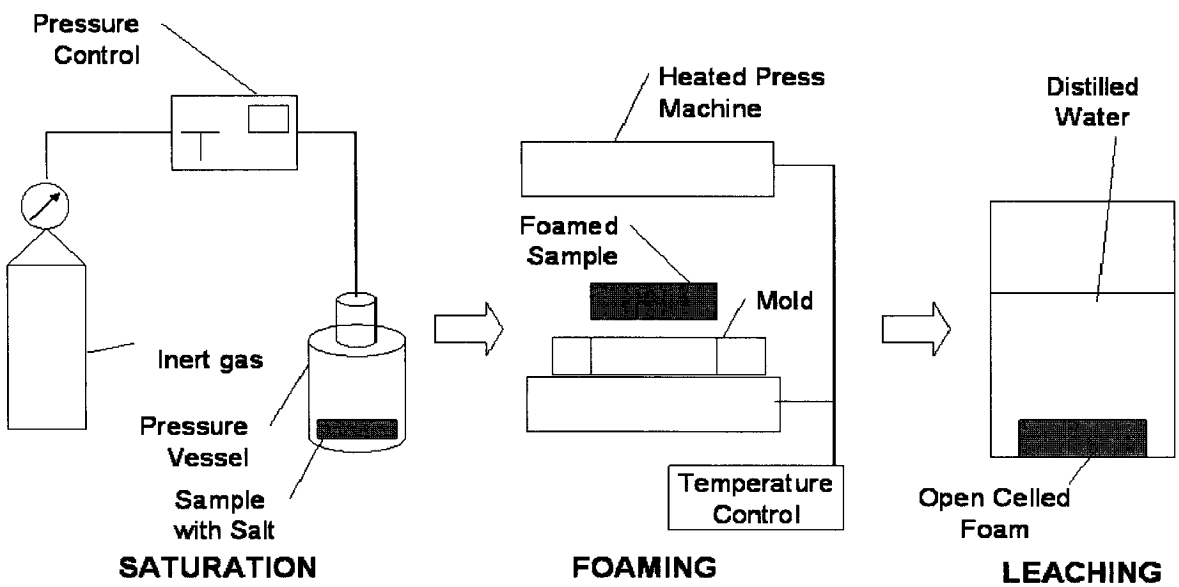

Figure 23 Three stage batch foaming for opened cell foam

6.2.3 Sample Characterization

The samples were air dried for 24 hours before being tested. By comparing the weights of the samples before and after leaching, the weight of the residual NaCl was evaluated to be small and negligible. The porosity of polymer matrices was calculated using the measured volume and weight of the matrices according to the following equation:

$$porosity = 1-[(weight/volume)/\rho_{polymer}] \times 100\% \quad (6.1)$$

The cell structure of these foams was characterized using optical microscope. The samples were cooled in liquid nitrogen before being fractured to produce a surface with minimum plastic deformation. ImageJ software from the U.S. National Institutes of Health (NIH) was then used to analyze the cell structure.

The mechanical properties of the porous materials were evaluated by compression test using an Instron 4482 machine with a 100 KN load cell at room temperature. The samples were cut into square pieces with a dimension of 10 mm by 10 mm and a thickness of 2.5 mm. The sample surfaces were smoothed using a fine grade file before testing. The strain rate of testing was 1.0 mm/min. The strain was calculated from the displacement of the crosshead. Five specimens were prepared and tested for each different experiment.

An acoustic absorption test was performed by the Groupe d'Acoustique et de Vibrations de l'Université de Sherbrooke (GAUS), Sherbrooke, QC, Canada. An impedance tube with a diameter of 44.44 mm was used. Results are presented in the frequency range [100Hz -4100 Hz]. The sound absorption measurements were performed in the case where the PMMA

samples are backed by a rigid termination. The measurements of the sound absorption coefficient were performed following the standard ASTM E1050-86 [106]. The results of the acoustic test are presented here are with the permission of GAUS.

6.3 Results and Discussion

6.3.1 Effect of Foaming Temperature on Foam Morphology and Acoustic Absorption Properties

To examine the effect of the foaming temperature input on the produced material microscopic and macroscopic properties of the produced material in turn, on its acoustic performance, PMMA samples were foamed at different temperatures. The temperatures considered were 60 °C, 80 °C, and 100 °C. The pressure used for gas-foaming was set to 5.2 MPa (810 psi). All other parameters were kept constant while foaming the samples in different temperatures.

Table 4 describes the properties of the PMMA samples considered. In each sample composition, the percentage of the PMMA polymer and that of the NaCl used are given as well as the size of their particles.

Normal incidence sound absorption coefficients associated with samples A, B and C are presented in Figure 24. During these measurements, the samples were backed by a rigid impervious wall.

Table 4: PMMA samples considered to investigate the effect of foaming temperature on the sound absorption coefficient.

PMMA ID FOAMED AT 5.2 MPA	COMPOSITION : 20% PMMA <250μM + 80% NACL <500μM	DENSITY (KG/M^3)	POROSITY
SAMPLE A	FOAMED AT 60°C	365	0.688
SAMPLE B	FOAMED AT 80°C	411	0.649
SAMPLE C	FOAMED AT 100°C	468	0.600

Table 5: Effect of gas foaming temperature on average cell sizes and airflow resistivity of produced PMMA samples.

PMMA ID FOAMED AT 5.2 MPA	AVERAGE SMALL PORE SIZES (μM)	AVERAGE LARGE PORE SIZES (μM)	AIRFLOW RESISTIVITY σ ($N.S.M^{-4}$) (COURTESY OF GAUS)
SAMPLE A: FOAMED AT 60°C	9	290	194882
SAMPLE B: FOAMED AT 80°C	24	300	450308
SAMPLE C: FOAMED AT 100°C	30	310	OVER-RANGE

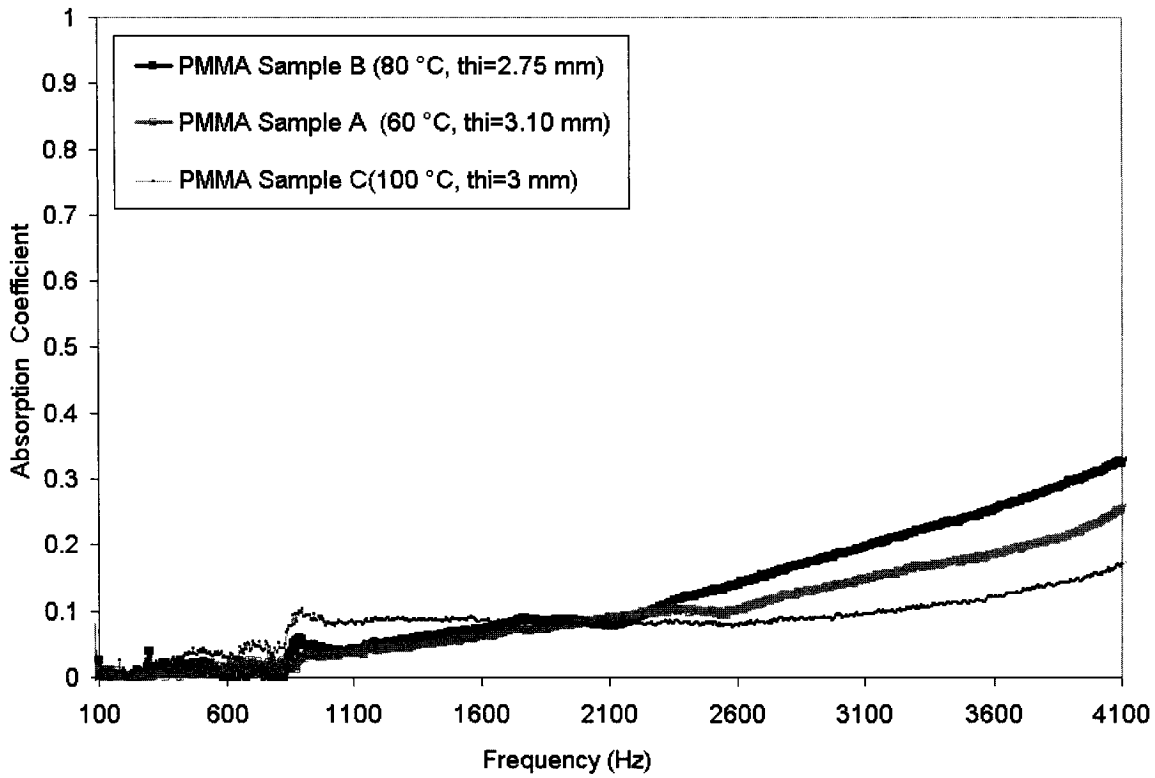

Figure 24 Absorption coefficient for PMMA samples foamed at three different temperatures (Courtesy of GAUS)

In the inhomogeneous domain strategy adopted in this work to fabricate open cell PMMA foams, two different cell sizes (large and small) were produced in the samples. In Table 5, the average of cell sizes produced in PMMA samples A, B and C are presented as well as the airflow resistivity measurements following the standard ASTM C 522-80 [106]. In the case of sample C the material was so highly resistive that the airflow measurement was not possible. Based on the results in Table 5, the foaming temperature was mainly affecting the small cells and their growth. The average size of the small cells was thus increased by increasing the foaming temperature.

Although sample C presents the largest two types of pores (30 μm for small pores and 310 μm for large pores), its porosity was the lowest compared to samples A and B. This result correlated well to the measured airflow resistivity of samples. The lowest airflow resitivity was associated with the sample A with the higher porosity. The lowest porosity and higher airflow resistivity associated to sample C foamed at 100°C was attributed to the cell coalescence and sample shrinkage caused by the higher foaming temperature.

Based on the results shown in Figure 24, it is clear that better sound absorption performance was obtained in the case of PMMA sample B (foamed at 80°C) followed by the case of sample A (foamed at 60°C). The porosities calculated according to Equation (6.1) were listed in Table 4. They indicate that the porosity of the samples decreased when the temperature increased. Although sample B is less porous than sample A, its acoustic performance is better. A good sound absorbing material is not only dictated by the present open porosity, but also by the size and number of interconnected open-cell populations.

6.3.2 Effect of Foaming Agent Particle Size on Foam Morphology and Acoustic Absorption Properties

As stated in the samples processing section, the NaCl particles were used as foaming agent and introduced into the polymer domain to promote mainly open cell structures. To investigate the effect of NaCl particle sizes on the produced sample microcellular properties, as well as its sound absorption coefficient, samples were fabricated with different NaCl particle sizes. In Table 6, the fabricated PMMA samples with three different NaCl particle sizes (<250 μm, <500 μm, >500 μm) are described. While in Table 7, the average cell sizes of produced samples are compared. The airflow resistivity measurements associated with the samples are also shown in Table 7. In the case of sample E, the material was so highly resistive that the airflow measurement was not possible with the equipment.

Analyzing the results of Table 6 and Table 7, one may note that the sizes of small cells were almost unaffected by the NaCl particle size modification. An increase of salt particle sizes only increased the size of the large pores. It is important to emphasize here that the average size of the large pores is very close to the particle size of NaCl used. This provides an efficient control of the desired average large pore sizes and, consequently the targeted opened cell porosity.

Following these results, any NaCl particle sizes modification will mainly affects the size of the large cells and, consequently the porosity and flow resistivity of sample. In fact, the sample E obtained using salt particle sizes higher than 500 μm presented the highest porosity

and the lowest airflow resistivity compared to the two other samples with different NaCl particles sizes.

In terms of acoustic performance, the absorption coefficients associated with samples A, D and E are presented in Figure 25. Due to the small thickness of the produced PMMA samples, stack of three layers were used instead of single layers in the comparison.

Following the results of Figure 25, it is clear that the sound absorption performance associated with sample E foamed with a NaCl particle size > 500 μm is better than those foamed with lower NaCl particle sizes. This result is logical since this sample presents the highest porosity (0.728) and the lowest airflow resistivity (173287 N.s.m-4) which are generally the most important parameters in determining the acoustic performance of a material.

Table 6: Description of PMMA samples used to investigate the effect of NaCl particle sizes on the sound absorption coefficient.

PMMA ID (FOAMED AT 5.2 MPA AND 60°C)	COMPOSITION: 20% PMMA <250μM + 80% NACL	DENSITY (KG/M^3)	POROSITY
SAMPLE A:	NACL <500μM	365	0.688
SAMPLE D:	NACL <250μM	332	0.716
SAMPLE E:	NACL >500μM	318	0.728

Table 7: Effect of NaCl particle sizes on average cell sizes and airflow resistivity of produced PMMA samples

PMMA ID (FOAMED AT 5.2 MPA AND 60°C)	AVERAGE SMALL PORE SIZES (μM)	AVERAGE LARGE PORE SIZES (μM)	AIRFLOW RESISTIVITY σ ($N.S.M^{-4}$) (COURTESY OF GAUS)
SAMPLE A: NACL <500μM	9	290	265751
SAMPLE D: NACL <250μM	10	240	OVER-RANGE
SAMPLE E: NACL >500μM	9	500	173287

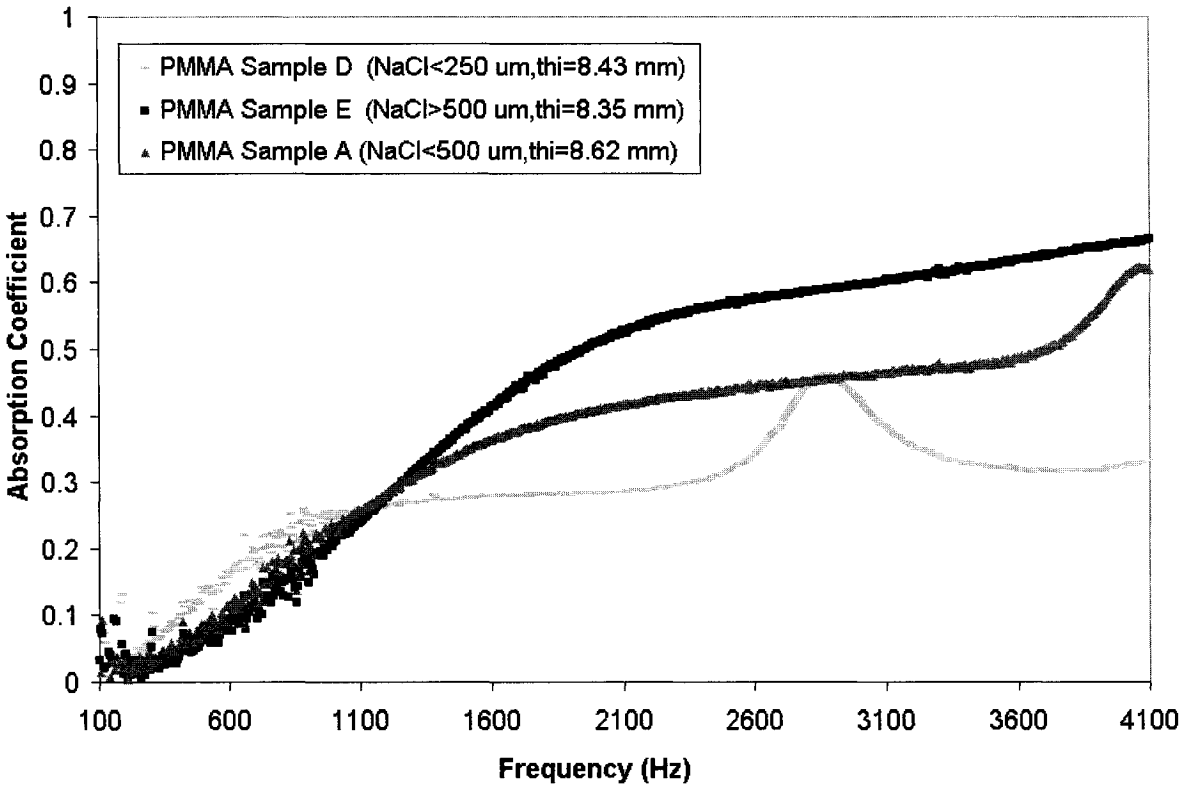

Figure 25 Absorption coefficient for PMMA samples A, E, and D, foamed with three different NaCl particle sizes. (Courtesy of GAUS)

6.3.3 Effect of Foaming Agent Content on Foam Morphology and Acoustic Absorption Properties

The investigation of the gas foaming temperature effect and the foaming agent particle size effect revealed that better sound absorption performance was obtained at a temperature of 80 °C, and with higher NaCl particle sizes. These two processing parameters were thus retained in the following study into the effect of different foaming agent contents on the sound absorption performance of the produced samples. Since NaCl content of less than 70% produced samples that are less porous, only NaCl content higher than 70% were investigated. Three different percentages of NaCl foaming agent were considered: 70%, 80%, and 90 %. The PMMA polymer involved in the composition of the each sample was consequently affected, and the corresponding PMMA polymer contents were 30%, 20% and 10%. The PMMA samples produced were denoted sample F, sample G and sample H. The porosity and density associated with each PMMA sample are listed in Table 8.

Analysing the results of Table 8, one may note that an increase of NaCl content during the foaming of PMMA samples caused an increase in porosity and a decrease in airflow resistivity. The NaCl particle sizes affected only the large cells while the small cells were unchanged by altering NaCl particle size. Therefore the more is the NaCl content, the more is the number of large open cells in the sample which resulted in higher porosity, lower airflow resistivity and density.

It was noticed that when samples were produced with different NaCl content, in addition

to the resulting thin samples (2 to 3 mm), the sample H (90%NaCl) was almost too brittle to be handled. To perform the necessary measurements was very difficult. Consequently, only one layer of produced samples was considered in the sound absorption coefficient measurements.

Following the results of Figure 26, the PMMA sample H with the highest porosity (0.845), lowest airflow resistivity (30 500 $N.s.m^{-4}$) and lower density (182 Kg/m^3), did not present the best absorption performance compared with the other two samples. It was the PMMA sample F with the lowest porosity (0.711) and the highest airflow resistivity (141113 $N.s.m^{-4}$) that presented better absorption performance. It was explained that sound absorption dissipation takes place generally in open-cell porous material. In fact, increasing the NaCl content will increase the number of large cells. Large cells which contribute to the open porosity of the material are mainly linked to thermal dissipation taking place in the porous medium. However, sound absorption in open cell porous media is mainly attributed to viscous dissipation. Since thermal dissipation is dominated by viscous dissipation, the sound absorption performance of a porous material is primarily controlled by the small opened cell population density and distribution. Consequently, increasing the porosity by increasing the number of large cells by increasing the NaCl content in the sample is not a good strategy to obtain a highly acoustic absorbent material. Moreover, increasing the percentage of NaCl to achieve a higher porosity is unfortunately also associated with weaker mechanical properties as it will be shown in the next section. The increase of large cells should be used with precaution to achieve certain porosity; more effort should be focused on the small open cells population. Increasing the porosity by increasing the number of small pores is a much preferred strategy.

It is shown that in Figure 27, when three layers of PMMA samples F and G are compared, the absorption of PMMA sample F is better than that of sample G, except at frequencies higher than 3200 Hz. This can be explained by the fact that when stacking three layers, since the sample F is more resistive than sample G, more wave reflections at higher frequencies take place at the interstices between layers in the case of sample F.

Table 8: Description of PMMA samples used to investigate the effect of NaCl content on the sound absorption coefficient.

PMMA ID (FOAMED AT 5.2 MPA AND 80°C)	COMPOSITION: PMMA <250μM + NACL >500μM	DENSITY (KG/M^3)	POROSITY
SAMPLE F	70% NACL + 30% PMMA	338	0.711
SAMPLE G	80% NACL + 20% PMMA	275	0.765
SAMPLE H	90% NACL + 10% PMMA	182	0.845

Table 9: Effect of NaCl content on average cell sizes and airflow resistivity of produced PMMA samples.

PMMA ID (FOAMED AT 5.2 MPA AND 80°C)	AVERAGE SMALL PORE SIZES (μM)	AVERAGE LARGE PORE SIZES (μM)	AIRFLOW RESISTIVITY σ ($N.S.M^{-4}$) (COURTESY OF GAUS)
SAMPLE F: 70% NACL	21	660	141113
SAMPLE G: 80% NACL	27	730	87623
SAMPLE H: 90% NACL	23	670	30500

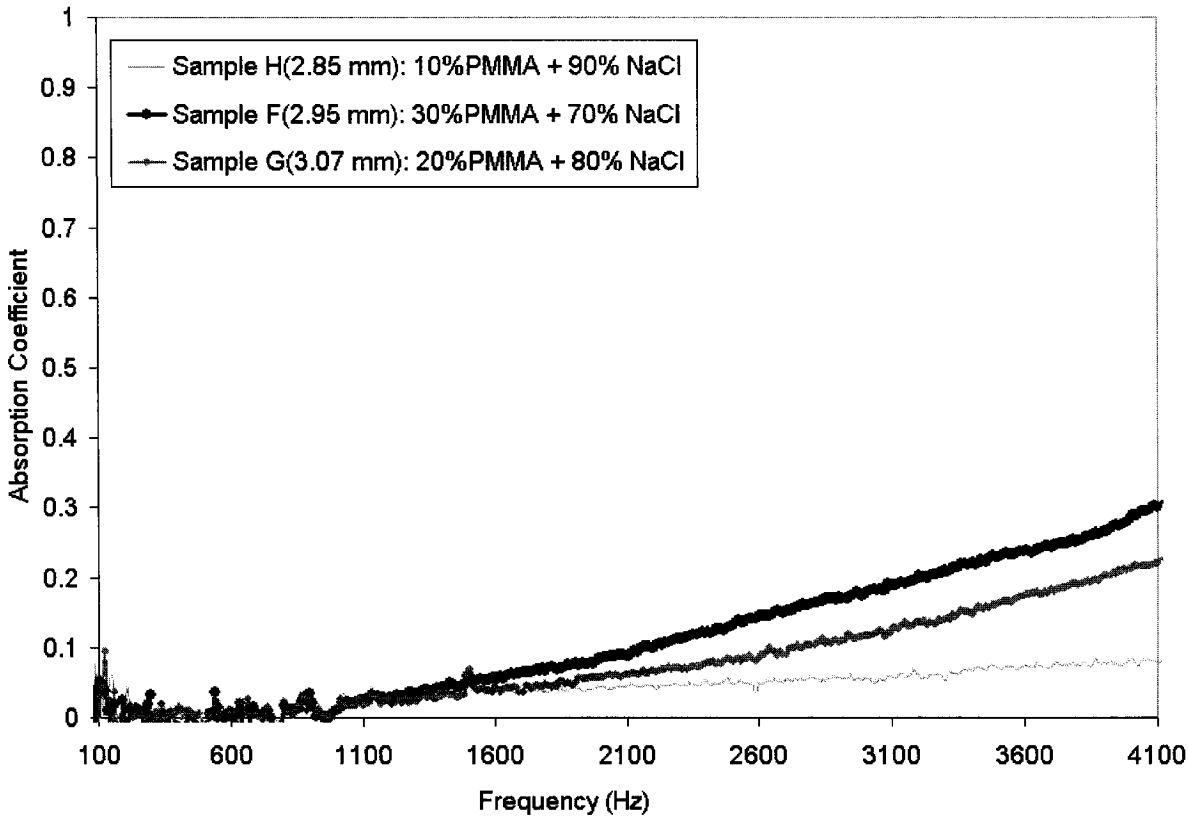

Figure 26 Absorption coefficient for PMMA samples F, G, and H, foamed with three different NaCl content. (Courtesy of GAUS)

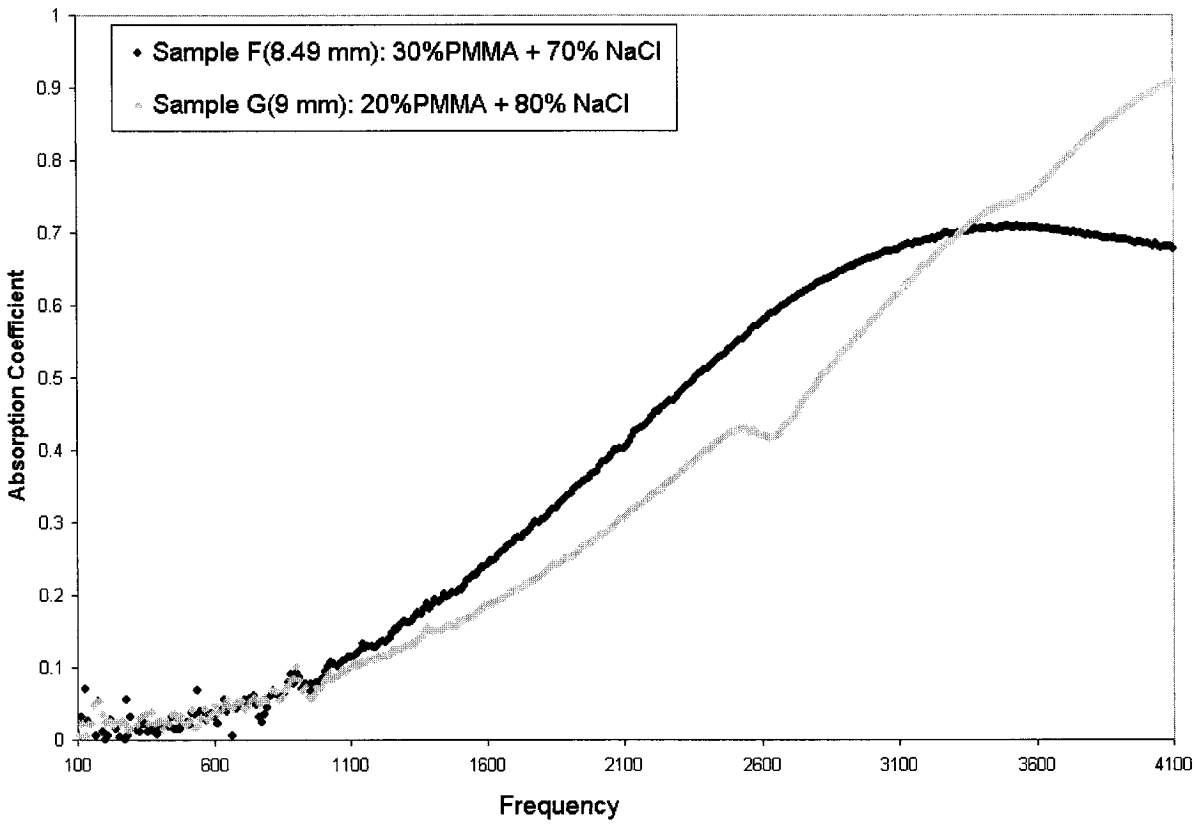

Figure 27 Absorption coefficient for PMMA samples F(70%NaCl) and G(80% NacL). (Courtesy of GAUS)

6.3.4 Mechanical Properties

Finally, the mechanical properties of the open cell foam were examined to verify their integrity under stress. The results of the compression tests are shown in Figure 4. A typical compression stress-strain curve was consists of three regions: linear elasticity region, plateau region and densification region, which agree with the compression response of traditional foams reported in literature [104]. In the linear region, the cell walls are subject to bending and stretching; in the plateau region, the cells progressively collapse, and finally, in the densification region, the cell walls connect to each other and becoming rather solid. As shown in the Figure 28, foam samples with a higher porosity and a lower density are weaker according to the compression test. The modulus, yield stress and yield strain is lower for the foams with higher porosity. When the weight percentage of NaCl is as high as 90%, the porosity of the foam sample can reach 85%. However, the resultant foam samples were too weak to perform mechanical testing.

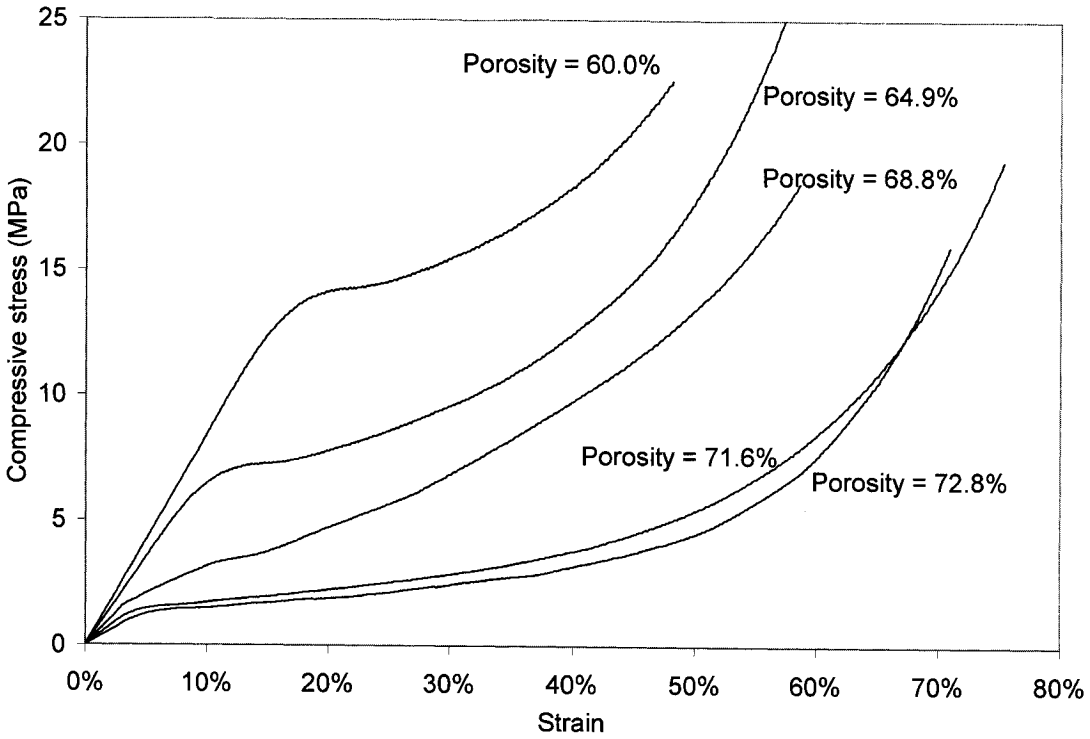

Figure 28 Stress-Strain curve of the compression test results for the opened cell foams with different porosity measurements

6.4 Conclusions

In this chapter, opened cell PMMA foams were obtained through a gas foaming/particulate leaching method. The resultant PMMA foams have a rigid frame and two different types of cells: large cells created by NaCl particles and small cells created by nucleation and growth of CO_2 induced by thermodynamic instability. The resultant samples had a thin thicknesses (from 2 to 3 mm) which made them interesting candidates as sound absorbing materials when spaces is limited such as for the core foams of headliners in automotive applications.

The morphology and the sound absorption of the PMMA foams were investigated under certain controlled processing parameters such as the gas foaming temperature, NaCl particle size and the percentage of the NaCl content. With an increase in the foaming temperature, it was found that the average cell sizes of the small cells increased also. By contrast, the average cell sizes of the large cells were not significantly changed while the temperature was increased. The increase in temperature of foaming also led to an increase in density and decrease in porosity. The best sound absorption performance is associated to PMMA sample B foamed at the temperature of 80 °C.

When different NaCl particle sizes were investigated, it was found that the average large cell sizes increased when the average NaCl particle size was increased. The average size of the small cells are unaffected by changing the NaCl particle sizes, but the increase in NaCl particle size was accompanied by an increase in porosity and decreases in airflow resitivity

and density. The best sound absorption coefficient performance was associated with the PMMA sample foamed using the higher NaCl particle sizes which was greater than 500μm.

The investigation of different NaCl content showed that a PMMA sample with a porosity as high as 85% can be obtained. With an increase of NaCl percentage, an increase of porosity and decreases the airflow resistivity and density associated with the produced PMMA samples. The best sound absorption performance was not obtained with PMMA sample with the highest porosity, but was associated with PMMA sample with the lowest porosity and lowest NaCl content.

In this investigation of mechanical properties, the typical compression stress-strain behavior of PMMA foams accords with the compression response of traditional foams reported in literature. It was found that PMMA foam samples with a higher porosity were weaker in compression tests. An optimized porosity should be selected according to the application requirements concerning acoustic properties and mechanical properties.

Chapter 7: Finite Element Analysis for Foam Elastic Properties

7.1 Introduction

The properties of foam materials depend on the material from which they are made of, their relative density, and their internal geometrical structure. In order to understand how the properties can be optimized for a given application, it is important to link the physical properties of cellular solids to their density and microstructure. Experimental results indicated that the Young's modulus of the cellular solids is related to their density by [104]:

$$\frac{E_f}{E_p} = C\left(\frac{\rho_f}{\rho_p}\right)^n \tag{7.1}$$

where E_p and ρ_p are the Young's modulus and density of the solid from which the foam is made of, and E_f and ρ_f are the Young's modulus and density of foams. The constant C and n depend on the microstructure of the solid material. Experimental evidence suggested that n is close to 2 for opened cell foams. However, the complex dependence of C and n on microstructure is not well understood, and this remains a problem in predicting and optimizing the elastic properties of cellular solids.

Many computational methods and increased computational power now exist to simulate the properties of structures with a reasonable extent of complexity [107, 108]. In this chapter, finite element method (FEM) was used to study the elastic response of both opened and closed cell foams. Unit cell model was studied analytically before FEM analysis to evaluate

the FEM result. The elastic responses predicted by FEM were also compared with experimental data.

7.2 FEA Model Description

The geometry of the model for the opened cell foam is shown in Figure 29. This model is made of a uniformly spaced array of cubic cells. These cells are connected by intersecting aligned struts. All the cell edges have the same length of L. The connecting struts also have the same length L. The cross sections of all the struts are square and have a constant area of A. The width of the square cross section is t_c. The unit cell is defined as a single cubic with six connecting struts in x, y and z directions. The multi-cell model consists of various number of unit cells that are duplicated and spread out in x, y and z directions.

The geometry of the model for the closed cell foam is shown in Figure 30. In order to simulate the morphology of closed cell microcellular PMMA foams, a cubic foam model containing sphere cells is suggested because the cell shapes of the closed cell microcellular PMMA foams are mainly sphere or ellipse and the cell walls are relatively thick. The maximum number of cells that can be used in this model is nine due to the limited computing capacity of computers. It may cause some error in the finite element analysis due to the insufficient scale of model structure.

In the finite element analysis, one end of the model was fixed and test pressure forces were applied on the other end. A linear static analysis was conducted to study the elastic behaviors of the foams. The strain of the foams was calculated based on the deformation of the

model. The elastic modulus of the foams was obtained by dividing the stress by the strain.

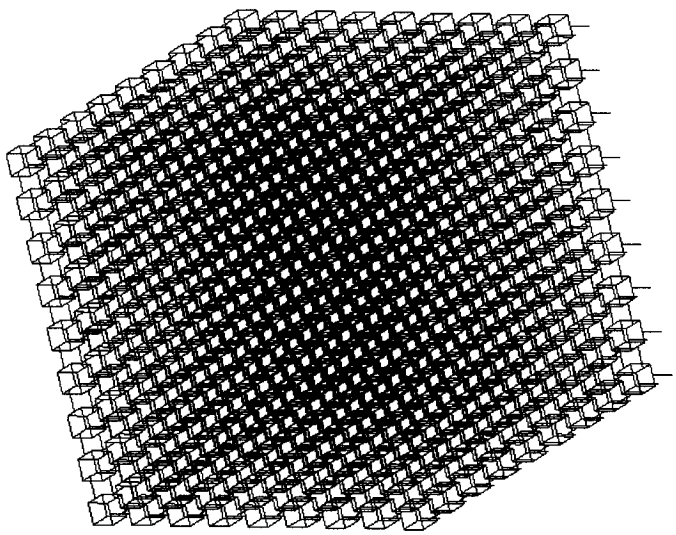

(a)

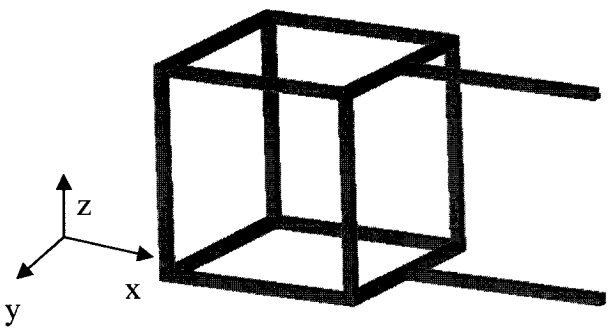

(b)

Figure 29 Finite element model for opened cell foams: (a) three dimensional open cell model with 729 cells and (b) a unit cell of the model

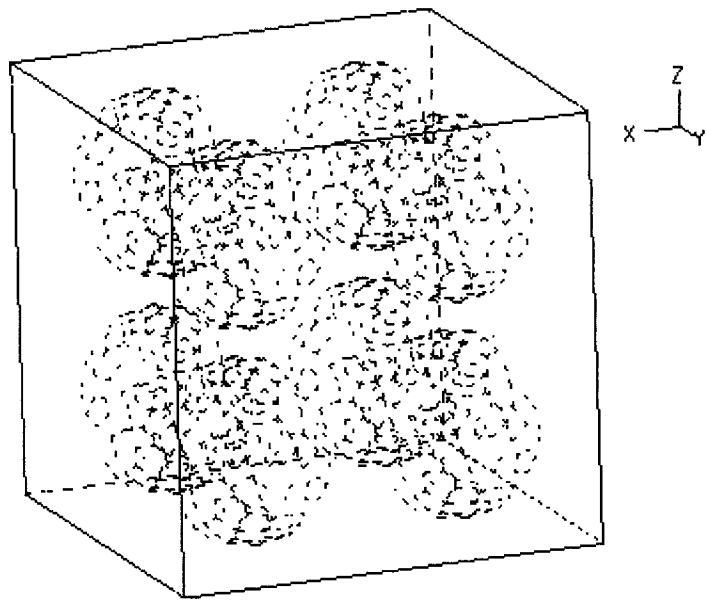

Figure 30 Finite element model for closed cell foams

7.3 Analytical Solution for the Unit Cell Model

The deformation of the unit cell is considered first. The unit cell described in the previous section is fixed on the left hand side and the compression forces *2F* is applied from the right hand side on the two struts in the direction of x-axis. The deformation of the unit cell can be solved using the Euler-Bernoulli Beam theory. The total deformation is considered to be the combination of the bending deflection of the beams perpendicular to the forces and the compressive deformation of the beams parallel to the forces:

$$\Delta L = \Delta L_B + \Delta L_C \tag{7.2}$$

where ΔL, ΔL_B and ΔL_C are the total deformation, bending deflection and compressive deformation of the unit cell in x-axis respectively.

From thin beam theory, the deflection of the beam perpendicular to the forces with simple supported ends is:

$$\Delta L_B = \frac{FL^3}{48E_pI} \tag{7.3}$$

where F is the force applied on the beam, E_p is the elastic modulus and I is the moment of inertia. For square cross-sectional beam,

$$I = \frac{t_c^4}{12} \tag{7.4}$$

Therefore,

$$\Delta L_B = \frac{FL^3}{4E_pt_c^4} \tag{7.5}$$

The compressive deformation of the unit cell ΔL_C consists of the compressive deformation of the struts in the cubic ΔL_{C1} and that of the connecting struts ΔL_{C2}. For both cases, we have:

$$\sigma = E_f \varepsilon \tag{7.6}$$

where σ is the stress and ε is the strain. Consider the deformation of the struts parallel to the forces in the cubic due to the compression ΔL_{C1}, Equation (7.6) becomes:

$$\frac{F/2}{t_c^2} = E_p \frac{\Delta L_{c1}}{L} \Rightarrow \Delta L_{c1} = \frac{FL}{2t_c^2 E_p} \tag{7.7}$$

Using the same method, the deformation of the connecting struts parallel to the forces due to the compression ΔL_{c2} is given by:

$$\Delta L_{c2} = \frac{FL}{t_c^2 E_p} \tag{7.8}$$

Therefore, the total deflection of the unit cell is:

$$\Delta L = \frac{FL^3}{4E_p t_c^4} + \frac{3FL}{2t_c^2 E_p} \tag{7.9}$$

The Young's modulus of the foam is:

$$E_f = \frac{2F/A}{\Delta L / L_L} = \frac{F}{\Delta L \cdot L} = \frac{E_p}{\frac{L^4}{4t_c^4} + \frac{3L^2}{2t_c^2}} \tag{7.10}$$

Or

$$\frac{E_f}{E_p} = \frac{1}{\frac{L^4}{4t_c^4} + \frac{3L^2}{2t_c^2}} \tag{7.11}$$

For long thin beam, $L >> t_c$, therefore:

$$\frac{E_f}{E_p} = \frac{1}{\frac{L^4}{4t_c^4} + \frac{3L^2}{2t_c^2}} \approx \frac{4t_c^4}{L^4} \tag{7.12}$$

The expansion ratio can be calculated by:

$$\varphi = \frac{\rho_f}{\rho_p} = \frac{18t_c^2 L - 16t_c^3}{(2L)^3} = \frac{9t^2 L - 8t_c^3}{4L^3} \tag{7.13}$$

For long thin beam,

$$\varphi = \frac{\rho_f}{\rho_p} = \frac{9t_c^2 L - 8t_c^3}{4L^3} \approx \frac{9t_c^2}{4L^2} \tag{7.14}$$

By comparing Equation (7.12) and Equation(7.14), we can write:

$$\frac{E_f}{E_p} = C\left(\frac{\rho_f}{\rho_p}\right)^2 \tag{7.15}$$

where, C=0.79

So the relationship between the Young's modulus of unit cell foams and the expansion ratio can be expressed as:

$$\frac{E_f}{E_p} = 0.79\left(\frac{\rho_f}{\rho_p}\right)^2 \tag{7.16}$$

Note that this derivation is under the assumptions: (1) There is only one cell and no affection from other cells; (2) The struts have simple support ends; (3) The length of the struts are much greater than the thickness; and (4) The strain is small.

From Equation (7.9) and Equation (7.12), we can see that, under the assumption of long thin beam, the bending deformation of the struts are much greater than their compression deformation. Therefore, the edge bending becomes the primary mechanism of the compression behavior.

The analytical solution of the multi-cell cell models, for both opened cell and closed cell foam, are more complex. Therefore, a numerical analysis was employed in these cases.

7.4 Finite Element Analysis

7.4.1 Opened Cell Foam

For opened cell model, four models with 1 cell, 27 cells, 196 cells and 729 cells were considered. For each model, five different foam densities were studied. An existing commercial finite element analysis software ADINA 8.1 was used.

First, the 1 cell model was studied using FEM and compared with analytical solution. The geometry, loads and boundary conditions of this model is exactly same as the one used in the analytical solution. Each cell struts was divided into two beam elements. There are totally 28 elements in this model. This mesh density was proven to be accurate enough for beam element [109]. The deformation of a unit cell is shown in Figure 31. Foam density was changed by altering the ratio of t_c and L. The calculation of relative density is the same as the one in the analytical solution, which is given by Equation (7.13).

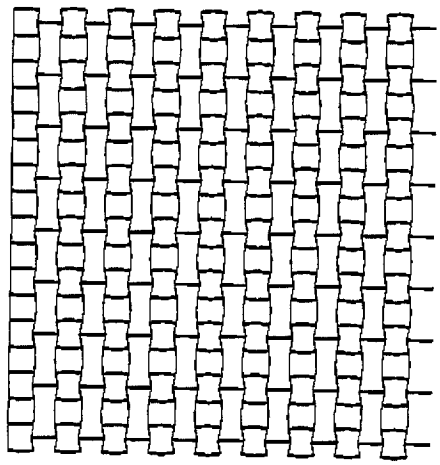

(a)

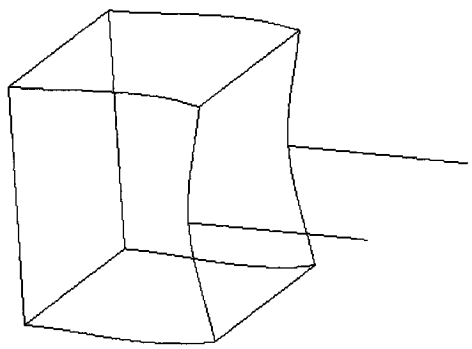

(b)

Figure 31 Deformed finite element model for opened cell foams: (a) front view of the three dimensional open cell model with 729 cells and (b) a unit cell of the model

Table 10: FEM results of unit cell model: (a) unit cell model, (b) 27 cells model, (c) 196 cells model and (d) 729 cells model

t/L	E_f/E_p	ρ_f/ρ_p	$(\rho_f/\rho_p)^2$	C
0.2	8.62E-03	7.40E-02	5.48E-03	0.64
0.1	7.13E-04	2.05E-02	4.20E-04	0.59
0.05	4.85E-05	5.38E-03	2.89E-05	0.60
0.02	1.27E-06	8.84E-04	7.81E-07	0.61
0.01	7.99E-08	2.23E-04	4.97E-08	0.62
			Average C:	0.61

(a)

t/L	E_f/E_p	ρ_f/ρ_p	$(\rho_f/\rho_p)^2$	C
0.2	5.74E-03	7.40E-02	5.48E-03	0.95
0.1	4.11E-04	2.05E-02	4.20E-04	1.02
0.05	2.66E-05	5.38E-03	2.89E-05	1.09
0.02	4.31E-08	2.23E-04	4.97E-08	1.15
0.01	2.70E-09	5.60E-05	3.14E-09	1.16
			Average C:	1.08

(b)

t/L	E_f/E_p	ρ_f/ρ_p	$(\rho_f/\rho_p)^2$	C
0.2	4.99E-03	7.40E-02	5.48E-03	1.10
0.1	3.63E-04	2.05E-02	4.20E-04	1.16
0.05	2.36E-05	5.38E-03	2.89E-05	1.22
0.02	6.13E-07	8.84E-04	7.81E-07	1.28
0.01	3.83E-08	2.23E-04	4.97E-08	1.30
			Average C:	1.21

(c)

t/L	E_f/E_p	ρ_f/ρ_p	$(\rho_f/\rho_p)^2$	C
0.2	4.86E-03	7.40E-02	5.48E-03	1.13
0.1	3.52E-04	2.05E-02	4.20E-04	1.19
0.05	2.29E-05	5.38E-03	2.89E-05	1.26
0.02	5.93E-07	8.84E-04	7.81E-07	1.32
0.01	3.71E-08	2.23E-04	4.97E-08	1.34
			Average C:	1.25

(d)

The FEM results of unit cell model are presented in Table 10. The Young's modulus predicted by the Finite Element Analysis is slightly lower than that predicted by the analytical solution. One reason is that the bending moments applied on the two ends of the struts are neglected in the analytical solution; the other reason is that the bending of the cell edges parallel to the forces, which was also neglected in the analytical solution, was taken into consideration in the finite element analysis. Both the analytical and the FEM results are lower by 30%-40% than the experimental result because both these two analysis are based on a single cell where the interaction between cells were neglected.

The analysis of multi-cell models was similar with that of the unit cell model. The boundary condition applied in the multi-cell model is to fix all the degree of freedom of the vertexes at the left hand side. The compression forces are applied on the connecting struts. Again, each strut is divided into two beam elements. There are 864 beam elements in 27-cell model, which is a three by three by three array of unit cell; There are 7,488 elements in 196-cell model, which is a six by six by six array of unit cell; and there are 25,596 elements in 729-cell model, which is a nine by nine by nine array of unit cell. The deformed 729-cell finite element model is shown in Figure 31 from the top view.

As shown in Table 10, the relationship between foams' Young's modulus and expansion ratio still comply with Equation (7.1). The average C of each model is 1.08, 1.21, and 1.25. These models are used to verify the convergence in Figure 32. It is observed that when the cell number reached 729, the constant C approached to a stable value. Therefore, a further increase of model scale is not required and 729 cells are considered to be enough for analysis. The

result of finite element analysis can be written as:

$$\frac{E_f}{E_p} = 1.25\left(\frac{\rho_f}{\rho_p}\right)^2 \tag{7.17}$$

The Young's moduli predicted by multi-cell models are all higher than those predicted by the unit cell model. By increasing the number of cells, the predicted Young's modulus also increases, which shows that the interaction between cells increased the modulus of the foam structure. Therefore to simulate the real behavior of a foam structure accurately, a large scale of model in the Finite Element Analysis is necessary.

Comparing to the experimental result reported by Gibson and Ashby [104], the difference between the predicted Young's modulus by FEM and the experimental value is quite small, as shown in Figure 33. The error is mainly due to the difference between the finite element model and the real foam structure, the imperfection of the skeleton solid and the random distribution of cell size and density. The experimental data from the opened cell foam in Chapter 6 are also presented here. The elastic moduli of the open celled foams made by particulate leaching/gas foaming method are lower than those from the FEM prediction and Gibson's model. The difference may attribute to the slipping between the polymer and the residual NaCl.

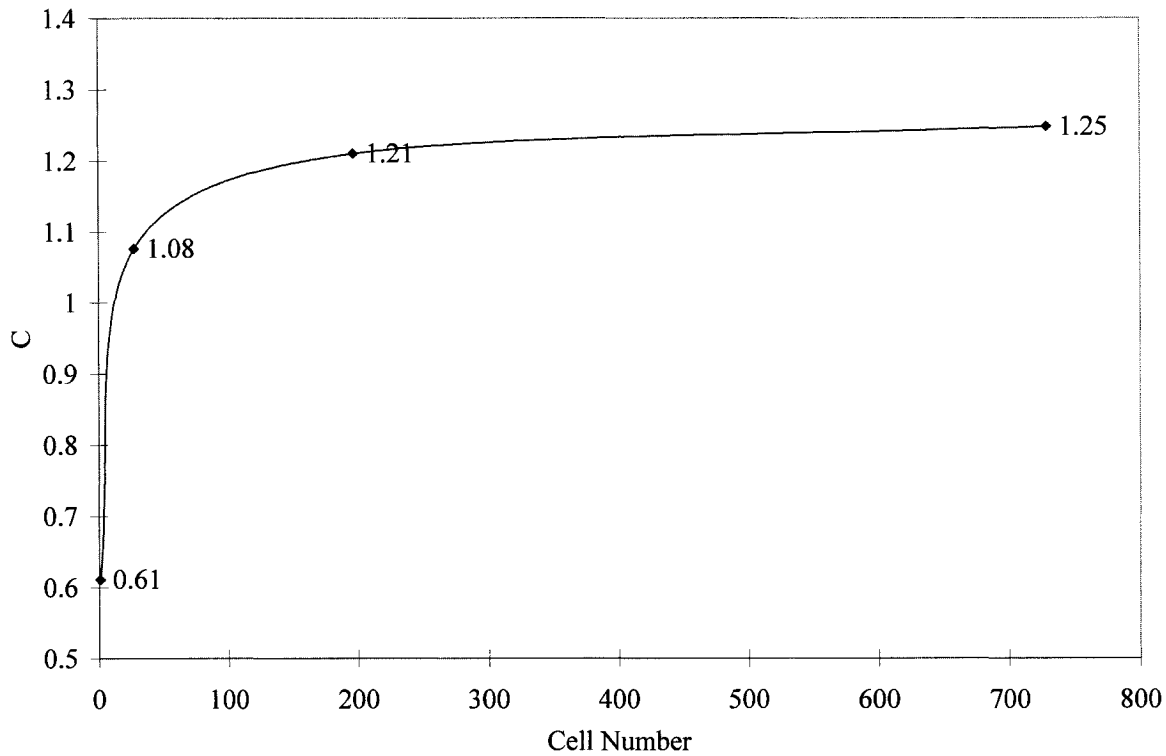

Figure 32 Convergence of C in different model scale

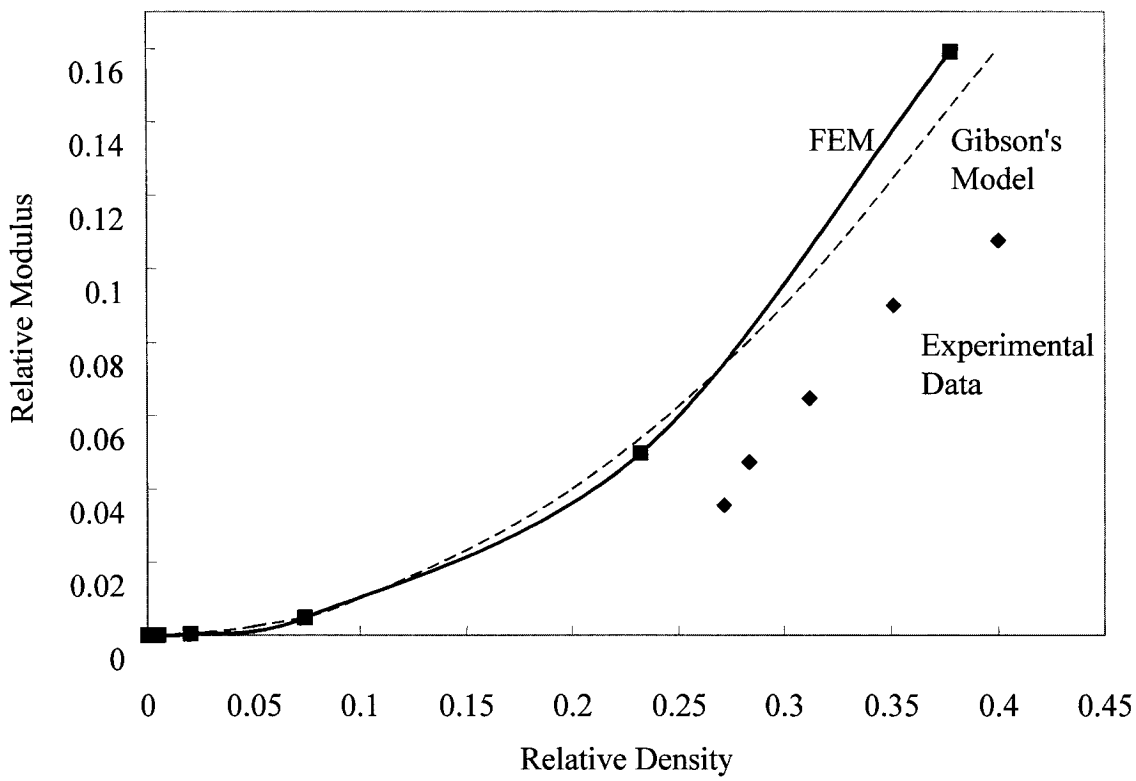

Figure 33 Comparison between FEM results and experimental data for opened cell foams.

7.4.2 Closed Cell Foam

The elastic response of closed cell foams was also simulated using the finite element analysis. The element type used to analysis this foam model is three-dimensional solid. The model was divided into four-node elements. Totally about 7400 elements was obtained by discretization in the closed cell FEM model. The number of element was slightly changed depending on the diameter of the cells. The relative density of the model was changed by altering the diameter of the cells. Comparing to the opened cell model, the closed cell FEM model applies to foams which have higher relative densities. In this study, the relative density ranged from 0.55 to 0.75. The relative density of the FEM model can be calculated according to the geometry of the model:

$$\frac{\rho_f}{\rho_p} = 1 - \frac{4\pi D_s^3}{3L^3} \tag{7.18}$$

where D_s is the diameter of each cell and L is the length of the cubic model. All the degree of freedoms in translation and rotation were fix at one side of the cubic. A pressure load was applied on the other side. The quantity of the pressure load was equivalent to the stress in the foam model and would be used in calculating the elastic modulus. Figure 34 showed the deformed finite element model for close cell foams.

In the small strain region, the elastic responses of the tension and compression were identical to each other according to the FEM result. The cell walls that are perpendicular to the load are subjected to bending and the cell walls that are parallel to the load are subjected

to compression or tension. The air pressure is very small and is neglected here. Similar to the opened cell foams, the relative density was found to be the most important parameter that affects the elastic modulus of the closed cell foams. The predicted relative elastic moduli are plotted against the relative density in Figure 35. The elastic modulus of the FEM model showed a great agreement with experimental results. The Gibson's model given by Equation (3.14) for the relative elastic modulus of closed cell foam is also plotted in Figure 35 as a reference. The possible sources of error include: insufficient model scale, the non-uniformity of the real foams, the irregular geometry of the real cells and the air pressure.

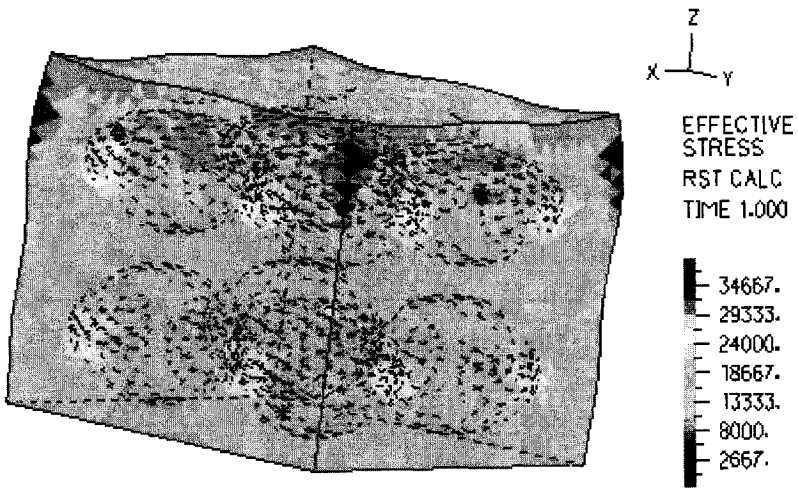

Figure 34 Deformed finite element model for closed cell foams

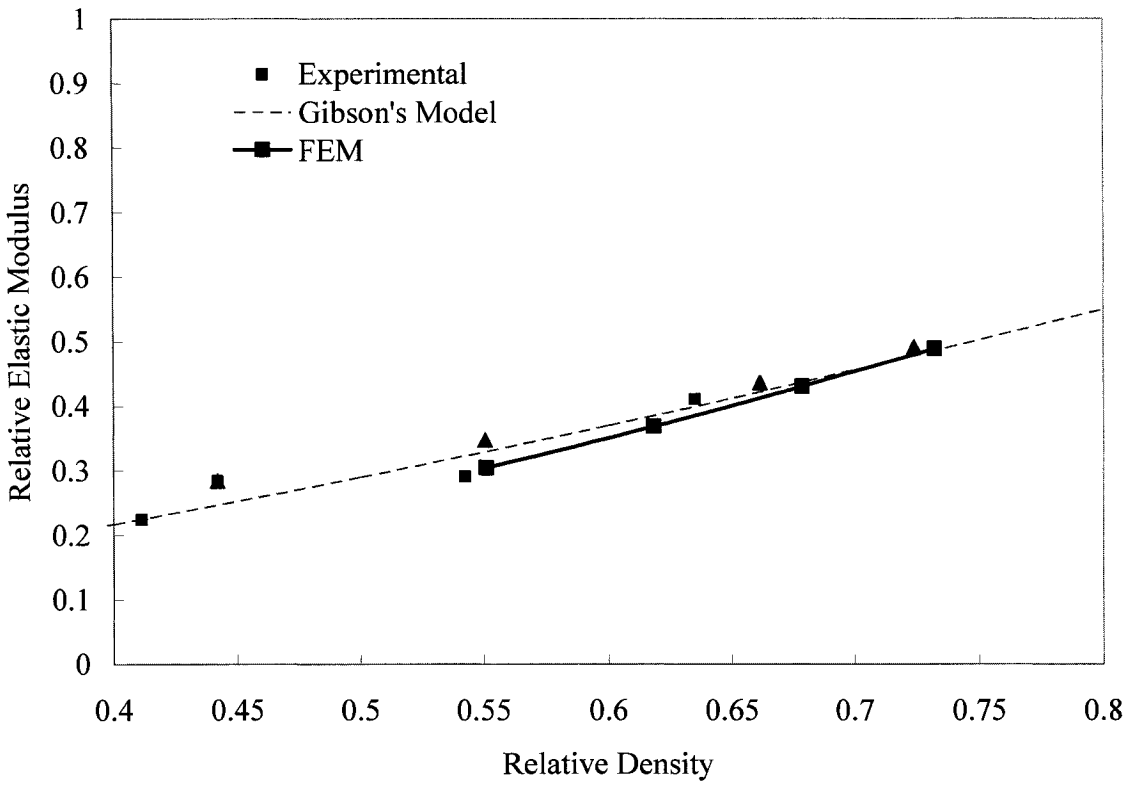

Figure 35 Comparison between FEM results and experimental data for closed cell foams.

7.5 Conclusions

An analytical method and a finite element method were used to evaluate the Young's modulus of three-dimensional models for opened cell foams. From the result of both the analytical method and the numerical method, The Young's modulus of the foam is expressed as a function of its relative density. So for the low density open cell foam material, the Young's modulus can be simply given as a function of the relative density and the Young's modulus of the original skeleton material.

For the low density open cell foam material, the linear elastic behavior is primarily due to the bending of cell walls. Therefore, the mechanical properties of foam material can be improved by increasing the bending stiffness of the cell walls. For high density foam structure, the longitudinal compression or tension deformation plays an important role in the linear elastic behavior of the open cell foam structure.

The interaction between cells increases the foam modulus. The accuracy is improved by increasing the scale of the models. In the further study on the properties of the foam material using Finite Element Analysis, a large scale FEM model is necessary.

The elastic response of closed cell foams was also investigated using the FEM with an 8-cell cubic model. Similar to the opened cell foams, the elastic modulus of the closed cell foams can be given as a function of the relative density. The predicted elastic response showed a great agreement with the experimental data.

Chapter 8: Conclusions

The main findings of this research are:

1. Microcellular PMMA foams with various foam densities, cell densities and average cell sizes can be produced using a batching process by controlling the processing parameters such as foaming time, foaming temperature and saturation pressure. The elastic modulus, tensile strength and elongation at break in tension increases by decreasing the foaming time, saturation pressure and foaming temperature, corresponding to the changes in foam morphology.
2. A great agreement is observed in elastic modulus between the experimental results of the microcellular foams and the existing theoretical model based on conventional foams. However, the tensile strengths of the microcellular foams are superior to the conventional foams. An empirical model is proposed to predict the tensile strength of microcellular foams. A higher elongation at break of the microcellular PMMA foam can be obtained compared with the unfoamed PMMA if the foaming conditions are well selected.
3. The mechanical properties of PMMA/clay nanocomposite can be enhanced by nanoclay. The PMMA nanocomposites with a nanoclay loading of 0.5 wt. %, prepared using the solvent co-precipitation method, exhibited optimal mechanical properties. Compared with neat PMMA samples, the elastic modulus increased by

25%, the tensile strength increased by 54%, and the elongation at break increased by 97%.

4. In microcellular foam processing, Nanometer scaled clay can be used as both a reinforcement filler and a nucleation agent. By creating a large amount of heterogeneous nucleation and increasing the diffusivity of the CO_2 in PMMA, the cell morphology of the foams are affected by nanoclay. The nanocomposite foams with 0.5 wt. % nanoclay content shows improved mechanical properties within the foam density range tested in this study.
5. Fine celled PP and LDPE foams were successfully produced using a rotational mold foaming process. The processing time and material particle sizes, including both the polymer and the blowing agent, are important processing parameters that affect the quality of the foam.
6. The stress-strain curve of relatively brittle PP polymer foams in compression tests exhibits a plateau region between a linear elastic region and a densification region. However, ductile polymer foam has only a linear elastic region and a densification region. The plateau region greatly improved the material's energy absorption capacity as the area under the curve was significantly increased. Therefore, brittle materials that have high modulus can be converted to "ductile" material through a foaming process in order to obtain an improved energy absorption capacity.
7. Opened cell PMMA foam can be developed with an improved acoustic absorption capacity by employing a particulate leaching method and a constrained molding

process. Two different levels of cell sizes are found in the foam – large cells on the order of 500 μm produced by particulate leaching and small cells on the order of 10-30 μm produced by gas foaming. Morphologies of the foam made by the gas foaming/particulate leaching method can be independently controlled: The size of the large cells can be controlled by the NaCl particle size; the size of the small cells can be controlled by changing the foaming temperature and different weight percentages of NaCl can be used to change the foam porosity.

8. A parametric study conducted by altering the processing parameters shows that the acoustic performance is controlled by adjusting the processing parameters with respect to the inner structure of the opened cell foam. The results of acoustic tests show that understanding and controlling the foam structure through adjusting the processing parameters are crucial for the development of porous materials with optimal acoustical efficiency.
9. Computer simulation using numerical method i.e., finite element analysis is a good means by which to correlate the micro-structural and macroscopic properties. Finite element analysis gives good predictions for both opened cell and closed cell polymeric foams with regards to the elastic response of the foams. Increasing the scale of the FEM model to include greater cell numbers can improve the accuracy of numerical analysis.

Chapter 9: Recommendations

The structure – properties relationships of foam should be further investigated. Currently, the mechanical properties such as modulus, strength were modeled simply as function of relative density. Similarly, the acoustic absorption properties were mainly expressed as foam porosity and air flow resistivity. Some other factors such as cell shape, cell size, and the non-uniformity of them are also greatly affecting the macroscopic properties. Due to the complexity of the geometry of the different foams, accurate analytical model for the structure – properties relationships is hardly reported. Numerical analysis method such as finite element analysis (FEM) is possibly a promising approach to solve this problem in mechanical, acoustic and thermal field. The non-linear behaviour of the microcellular foams is also to be more extensively studied.

A very small amount of nanometer scaled fillers can be used to produce foams with cell sizes as small as micrometer or even nanometer levels and improved mechanical properties. However, producing a well dispersed nanocomposite becomes a new challenging task in foam processing design. Different compounding technology and different types of nanoclay should be investigated to improve the cell uniformity, to enhance the mechanical properties and to produce even finer cell morphology.

Opened cell foams are required in various applications such as acoustic absorption and biomedical materials. However, a lot of the current existing foaming processes produce only

closed cell foams. Particulate leaching technology is suggested to be applied in these processes to obtain foams with opened cell structure.

References

1 Kumar, V.; VanderWel, M.; Weller, J., Seeler K. A. (1994). Experimental characterization of the tensile behavior of microcellular polycarbonate foams, Journal of Engineering Material Technology, 116, 4, 439-445.

2 Shulmeister, V. (1998). Modelling of the Mechanical Properties of Low-Density Foams, PhD thesis, Delft University of Technology.

3 Martini, J.E., Waldman, F. A., Suh, N. P. (1984). Microcellular closed cell foams and their method of manufacture, US Patent 4,473,665.

4 Park, C.B. and Suh, N.P. (1996). Filamentary Extrusion of Microcellular Polymers Using a Rapid Decompressive Element, Polymer Engineering and Science, 36, 1, 34-48.

5 Baldwin, D.F.; Park, C.B. and Suh, N.P., (1996). An Extrusion System for the Processing of Microcellular Polymer Sheets: Shaping and Cell Growth Control, Polymer Engineering and Science, 36, 10, 1425-1435.

6 Colton J. S., Suh, N. P., (1987). Nucleation of microcellular thermoplastic foam with additives: part i: theoretical considerations, Polymer Engineering and Science, 27, 485-492.

7 Colton J. S., Suh, N. P., (1987). Nucleation of microcellular thermoplastic foam with additives: part ii: experimental results and discussion, Polymer Engineering and Science, 27, 493-499.

8 Kumar, V; Suh N.P. (1990). A Process For Making Microcellular Thermoplastic Parts, Polymer Engineering and Science, 30, 1323-1329.

9 Matuana, L. M; Park, C. B; Balatinecz, J. J. (1998). Structures and Mechanical Properties Of Microcellular Foamed Polyvinyl Chloride, Cellular Polymers, 17, 1, 1-16.

10 Baldwin, D. F.; Suh, N. P. (1992). Microcellular Poly (Ethylene Terephthalate) and Crystallizable Poly Ethelene Terephthalate Characterization of Process Variables, ANTEC '92, SPE Tech Paper.

11 Collias, D. I.; Baird, D. G.. (1994). Impact Toughening of Polycarbonate By Microcellular

Foaming, Polymer, 35, 18, 3978-3983.

12 Klempner, D., Frisch, K. C. (1991). Chapter 1, In Handbook of Polymeric Foams and Foam Technology, Hanser Publishers, Munich.

13 Seeler, K. A.; Kumar, V. (1993). Tension-Tension Fatigue of Microcellular Polycarbonate: Initial Results, Journal of Reinforced Plastics and Composites, 12, 3, 359-376.

14 Shimbo, M.; Baldwin, D. F.; Suh, N. P. (1995). Viscoelastic Behavior of Microcellular Plastics with Varying Cell Size, Polymer Engineering and Science, 35, 17, 1387.

15 Guria, K. C.; Tripathy, D. K. (1997). Dielectric Properties of Closed Cell Microcellular Ethylene Propylene Diene Rubbers at Microwave Frequency, International Journal of Polymeric Materials, 37, 1-2, 53-64.

16 Griffith, A.A. Theory of rupture. (1924). Proceeding of the First International Conference of Applied Mechanics. 1, 55-63.

17 Okada, A.; Kawasumi, M.; Usuki, A.; Kojima, Y.; Kurauchi, T.; Kamigaito, O.(1990). Synthesis and properties of nylon-6/clay hybrids, In: Schaefer DW, Mark JE, editors. Polymer based molecular composites. MRS Symposium Proceedings, Pittsburgh, 171, 45-50.

18 Giannelis, E.P. (1996). Polymer layered silicate nanocomposites, Adv Mater, 8, 29-35.

19 Giannelis, E.P., Krishnamoorti, R., Manias, E.(1999). Polymer-silicate nanocomposites: model systems for confined polymers and polymer brushes, Adv Polym Sci,138, 107-47.

20 LeBaron, P.C., Wang, Z., Pinnavaia, T.J.(1999). Polymer-layered silicate nanocomposites: an overview, Appl Clay Sci,15,11-29.

21 Vaia, R.A., Price, G., Ruth, P.N., Nguyen, H.T., Lichtenhan, J. (1999). Polymer/layered silicate nanocomposites as high performance ablative materials, Appl Clay Sci,15, 67-92.

22 Biswas, M.; Ray, S. (2001). Recent Progress in Synthesis and Evaluation of Polymer-Montmorillonite Nanocomposites, Adv Polym Sci,155, 167-221.

23 McNally, T.; Murphy, W. R.; Lew, C.T.; Turner, R.J.; Brennan, G. P. (2003). Polyamide-12 layered silicate nanocomposites by melt blending, Polymer, 44, 2761-2772.

24 Tseng, C.R.; Wu, J.Y.; Lee, H.Y.; Chang, F.C. (2002). Preparation and characterization of

polystyrene-clay nanocomposites by free-radical polymerization, J. Appl. Polym. Sci., 85, 1370-1377.

25 Wan, C.; Qiao, X.; Zhang, Y. (2003). Effect of Different Clay Treatment on Morphology and Mechanical Properties of PVC-Clay Nanocomposites, Polym. Test., 22, 453-461.

26 Wang, H.; Zeng, C.; Elkovitch, M.; Lee, L.J.; Koelling, K.W. (2001). Processing and properties of polymeric nano-composites, Polym. Eng. Sci., 41(11), 2036-2046.

27 Du, J.; Zhu, J.; Wilkie, C.A.; and Wang, J. (2002). An XPS investigation of thermal degradation and charring on PMMA clay nanocomposites, Polym. Deg. Stab., 77, 377-381.

28 Gilman, J.W. (1999). Flammability and thermal stability studies of polymer-layered silicate (clay) nanocomposites. Appl Clay Sci,15, 31-49.

29 Bourbigot, S.; LeBras, M.; Dabrowski, F.; Gilman, J,W,; Kashiwagi T. (2000). PA-6 clay nanocomposite hybrid as char forming agent in intumescent formulations, Fire Mater, 24:201-8.

30 Bharadwaj, R.K. (2001). Modeling the barrier properties of polymer-layered silicate nanocomposites, Macromolecules, 34, 9189-9192.

31 Chang, J.H.; An, Y.U. (2002). Nanocomposites of polyurethane with various organoclays: Thermomechanical properties, morphology, and gas permeability, J. Polym. Sci. B: Polym. Phys., 40, 670-677.

32 Xu, R.; Manias, E.; Snyder, A.J., Runt, J. (2001). New biomedical poly(urethane uera)-layered silicate nanocomposites. Macromolecules,34, 337-9.

33 Messersmith, P.B.; Giannelis, E.P. (1995). Synthesis and barrier properties of poly(1-caprolactone)-layered silicate nanocomposites. J Polym Sci, Part A: Polym Chem, 33, 1047-57.

34 Yano, K.; Usuki, A.; Okada, A.; Kurauchi, T.; Kamigaito, O. (1993). Synthesis and properties of polyimide-clay hybrid. J Polym Sci, Part A: Polym Chem, 31, 2493-8.

35 Kojima, Y.; Usuki, A.; Kawasumi, M.; Fukushima, Y.; Okada, A.; Kurauchi, T.; Kamigaito, O. (1993). Mechanical properties of nylon 6–clay hybrid. J Mater Res, 8, 1179-84.

36 Kumar, S.; Jog, J.P.; Natarajan, U. (2003). Preparation and characterization of poly(methyl

methacrylate)-clay nanocomposites via melt intercalation: The effect of organoclay on the structure and thermal properties, J. Appl. Polym. Sci., 89, 1186-1194.

37 Fu, X.; Qutubuddin, S. (2001). Polymer-clay nanocomposites: Exfoliation of organophilic montmorillonite nanolayers in polystyrene, Polymer, 42, 807-813.

38 Ma, J.; Qi, Z.; Hu, Y. (2001). Synthesis and characterization of polypropylene/clay nanocomposites, J. Appl. Polym. Sci., 82, 3611-3617.

39 Alexandre, M.; Dubois, P. (2000). Polymer-layered silicate nanocomposites: preparation, properties and uses of a new class of materials, Materials Science and Engineering, 28, 1-63.

40 Manninen, A. R.; Naguib, H. E.; Nawaby, A. V.; Liao, X.; Day, M. (2005). The effect of clay content on PMMA-clay nanocomposite foams Cellular Polymers, 24, 2, 49-70.

41 Koros, W. J.; Paul, D. R. (1978). CO_2 Sorption in Poly(Ethylene Terephthalate) Above and Below The Glass Transition, J Polym Sci Polym Phys Ed, 16, 1947-1963.

42 Colton, J.S., Suh, N.P. (1987). Nucleation of Microcellular Foam: Theory And Practice Polym. Eng. Sci., 27, 7, 500-3.

43 Youn, J.; Suh. N. P. (1985). Processing of Microcellular Polyester Composites, Polym. Composite., 6, 3, 175-180.

44 Ramesh, N. S.; Rasmussen, D. H., Campbell G. A. (1991). Numerical and experimental studies of bubble growth during the microcellular foaming process, Polymer Engineering and Science, 31, 1657.

45 Venerus, D. C. (2001). Diffusion-induced bubble growth in viscous liquids of finite and infinite extent, Polymer Engineering and Science, 41, 8, 1390-1398.

46 Venerus, D. C. (2002). Modeling Diffusion-Induced Bubble Growth in Polymeric Liquids, Foams 2002, 169-173.

47 Venerus, D. C.; Yala, N.; Bernstein, B. (1998). Analysis of diffusion-induced bubble growth in viscoelastic liquids, J. Non-Newtonian Fluid Mech., 75, 55-75.

48 Shafi, M. A.; Lee, J. G. and Flumerfelt, R. W. (1996). Prediction of cellular structure in free expansion polymer foam processing, Polymer Engineering and Science, 36, 14, 1950-1959.

49 Martini, J.E.; Waldman, F. A. ; Suh, N. P. (1984). Microcellular closed cell foams and their method of manufacture, US Patent 4,473,665.

50 Goel, S. K.; Beckman, E. (1994). Generation of microcellular polymeric foams using supercritical carbon dioxide. I: effect of pressure and temperature on nucleation, Journal of Polymer Engineering and Science, 34, 14, 1137.

51 Handa, Y. P.; Zhang, Z. (2000). A new technique for measuring retrograde vitrification in polymer-gas systems and for making ultramicrocellular foams from the retrograde phase, Journal of Polymer Science: Part B: Polymer Physics, 38, 5, 716-725

52 Handa, Y. P.; Zhang, Z.; Wong, Z.; Wong, B. (2001). Solubility, diffusivity, and retrograde vitrification in PMMA-CO2, and development of sub-micron cellular structures, Cellular Polymer., 20, 1, 1-16.

53 Arora, K. A.; Lesser, A. J.; McCarthy, T. J. (1998). Compressive behavior of microcellular polystyrene foams processed in supercritical carbon dioxide, Polym. Eng. Sci., 38, 2055.

54 Arora, K. A., Lesser, A. J., McCarthy, T. J. (1998). Preparation and characterization of microcellular polystyrene foams processed in supercritical carbon dioxide, Macromolecules, 31, 4614.

55 Wang, J.; Cheng, X.; Yuan, M.; He, J. (2001). An investigation on the microcellular structure of polystyrene/LCP blends prepared by using supercritical carbon dioxide, Polymer, 42, 19, 8265-75.

56 Stafford, C. M.; Russell, T. P.; McCarthy, T. J. (1999). Expansion of polystyrene using supercritical carbon dioxide: effects of molecular weight, polydispersity, and low molecular weight components, Macromolecules, 32, 22, 7610-6.

57 Mizumoto, T.; Sugimura, N.; Moritani, M.; Sato, Y.; Masuoka, H. (2000). CO_2-induced stereocomplex formation of stereoregular poly(methyl methacrylate) and microcellular foams, Macromolecules, 33, 18, 6757-63.

58 Nawaby, V.; Yamamoto, Y.; Handa, P. (2002). Kinetic Study on PMMA-CO2 System by Raman Spectroscopy, SPE ANTEC paper. San Francisco, USA

59 Baldwin, D. F.; Park, C. B.; Suh, N. P. (1996). Microcellular processing study of poly(ethylene terephthalate) in the amorphous and semicrystalline states. Part I: Microcell

nucleation, Polym. Eng. Sci., 36,1437.

60 Baldwin, D. F.; Park, C. B.; Suh, N. P. (1996). Microcellular processing study of poly(ethylene terephthalate) in the amorphous and semicrystalline states. Part II: Cell growth and process design, Polym. Eng. Sci., 36,1446.

61 Handa, P.; Wong, B.; Zhang, Z.; Kumar, V.; Eddy, S.; Khemani, K. (1998). Some thermodynamic and kinetic properties of the system PETG-CO2, and morphological characteristics of the CO2-blown PETG foams, Polym. Eng. Sci., 39, 1, 55-61.

62 Park, C. B.; Cheung L. K. (1997). Study of cell nucleation in the extrusion of polypropylene foams, Polym. Eng. Sci., 37, 1.

63 Doroudiani, S.; Park, C.B.; Kortschot, M.T. (1996). Effect of Crystallinity and Morphology on the Microcellular Foam Structure of Semicrystalline Polymers, Polymer Engineering and Science, 36, 21, 2645-2662.

64 Liu, S. J.; Tsai, C. H. (1999). Experimental study of foamed polyethylene in rotational molding, Polymer Engineering and Science Vol. 39, 1776.

65 Liu, S. J.; Yang, C. H. (2001). Rotational molding of two-layered polyethylene foams, Advances in Polymer Technology, 20, 2, 108-115.

66 Liu, G.; Park, C. B.; Lefas, J. A. (1998). Production of low-density LLDPE foams in rotational molding, Polym Eng Sci, 38, 12, 1997-2009.

67 Pop-Iliev R.; Liu,F.; G. Liu; Park, C.B. (2003). Rotational Foam Molding of Polypropylene with Control of Melt Strength, Advances in Polymer Technology, 22, 4, 280–296.

68 Fischer, H. (2003). Polymer Nanocomposites: From Fundamental Research to Specific Applications, Materials Science and Engineering: C, 23, 6-8, 15, 763-772

69 Brindly, S.W.; Brown, G. (1980). Crystal structure of clay minerals and their X-ray diffraction. London: Mineralogical Society.

70 Ray, S. S.; Okamoto, M. (2003). Polymer/layered silicate nanocomposites: a review from preparation to processing Progress in Polymer Science, 28, 11, 1539-1641.

71 Lee, D. C.; Jang, L. W. (1996). Preparation and Characterization of PMMA-Clay Hybrid

Composite by Emulsion Polymerization, Journal of Applied Polymer Science, 61, 1117-1122.

72 Qu, X.; Guan, T.; Liu, G.; She, Q.; Zhang, L. (2005). Preparation, Structural Characterization, and Properties of Poly(methyl methacrylate)/Montmorillonite Nanocomposites by Bulk Polymerization, Journal of Applied Polymer Science, 97, 348–357

73 Li, Y.; Zhao, B.; Xie, S.; Zhang, S., (2003). Synthesis and properties of poly(methyl methacrylate)/montmorillonite (PMMA/MMT) nanocomposites, Polymer International 52, 892–898

74 Okamotoa, M.; Moritaa, S.; Taguchia, H.; Kima, Y. H.; Kotakaa, T.; Tateyamab, H. (2000). Synthesis and structure of smectic clay/poly(methyl methacrylate) and clay/polystyrene nanocomposites via in situ intercalative polymerization, Polymer, 41, 3887–3890.

75 Hwu, J. M.; Jiang, G. J.; Gao, Z. M.; Xie, W.; Pan, W. P. (2002). The Characterization of Organic Modified Clay and Clay-Filled PMMA Nanocomposite, Journal of Applied Polymer Science, 83, 1702–1710

76 Wanga, G.; Wangb, C.; Chen, C. (2005). The disorderly exfoliated LDHs/PMMA nanocomposite synthesized by in situ bulk polymerization, Polymer, 46, 5065–5074

77 Park J. H.; Jana, S. C. (2003). The relationship between nano- and micro-structures and mechanical properties in PMMA–epoxy–nanoclay composites, Polymer, 44, 2091–2100

78 Zeng, C.; Han, X.; Lee, L.J.; Koelling, K.W.; Tomasko, D.L. (2003). Polymer-Clay Nanocomposite Foams Prepared Using Carbon Dioxide, Advanced Materials, 15, 1743-1747

79 Mitsunaga, M.; Ito, Y.; Ray, S. S.; Okamoto, M.; Hironaka, K. (2003). Intercalated Polycarbonate/Clay Nanocomposites: Nanostructure Control and Foam Processing, Macromolecular Materials and Engineering, 288, 543-548

80 Nam, P.; Maiti, P,; Okamoto, M.; Kotaka, T.; Nakayama, T.; Takada, M.; et al. (2002) Foam processing and cellular structure of polypropylene/clay nanocomposites. Polym Eng Sci, 42, 1907–18.

81 Wang, K.H.; Lee, Y.H.; Park, C.B., (2004). Optimum Content of Clay for Microcellular LDPE/Clay Nanocomposite Foams Blown with CO_2, SPE, ANTEC Technical Papers, 2510-14.

82 Guo, G.; Wang, K.H.; Park, C.B.; Kim, Y.S; Li, G.. (2004). Effects of Nano-Particles on

Density Reduction and Cell Morphology of Extruded mPE/Wood-fiber/Nano Composites, SPE, ANTEC Technical Papers, 2620-5.

83 Han, X.; Zeng, C.; Lee, L. J.; Koelling, K. W., Tomasko, D. L., (2003). Extrusion of Polystyrene Nanocomposite Foams With Supercritical CO_2, Polymer Engineering and Science, 43, 6,1261-1275.

84 Hilyard, N. C. (ed.) (1982) Mechanics of Cellular Plastics, Macmillan, New York.

85 Hilyard, N. C. and Cunningham, A. (1994). Low Density Cellular Plastics, Chapman & Hall, London.

86 Sun, H.; Sur, G. S.; Mark E.J. (2002). Microcellular foams from polyethersulfone and polyphenylsulfone: Preparation and mechanical properties, European Polymer Journal, 38, 2373-81.

87 Sun, H.; Mark, J.E. (2002). Preparation, characterization, and mechanical properties of some microcellular polysulfone foams, Journal of Applied Polymer Science, 86,1692-701.

88 Donald, E. (1987), 'Basic Acoustics' Harper and Row.

89 Saira, A. (2001). Thermal Conductivity and Noise Attenuation in Aluminium Foams, A dissertation submitted for the degree of Master of Philosophy in Materials Modelling at the University of Cambridge.

90 Lu, T.J.; Hess, A. (1999). Sound Absorption In Metallic Foams, Journal of Applied Physics, 85, 7528-7539.

91 Lu, T. J.; Chen, F.; He, D. P., (2000). Sound absorption of cellular metals with semi-open cells, Journal of the Acoustical Society of America, 108, 4, 1697—1709.

92 Allard, J. F. (1994). Propagation of Sound in Porous Media: Modeling Sound Absorbing Materials, Elsevier Applied Science, New York.

93 Biot, M.A. (1962). Generalized theory of acoustic propagation in porous dissipative media, Journal of the Acoustical Society of America, 34 1254-1264.

94 Biot, M.A. (1956). Theory of propagation of Elastic waves in Fluid Saturated Porous solids, I: low frequency Range. II: Higer frequency range, J. Acoust. Soc. Am. 28, 168-191

95 Johnson, D. L.; Koplik, J. and Dashen, R. (1987). Theory of dynamic permeability and tortuosity in fluid-saturated porous media. J. Fluid Mechanics., 176, 379-402.

96 Balik, C.M. (1996). On the extraction of diffusion coefficients from gravimetric data for sorption of small molecules by polymer thin films, Macromol., 29, 3025-9.

97 Suh, N.P. (1990). The Principles of Design, Oxford University Press, New York.

98 PennEngineering Motion Technologies (1997). Power Transmission Design

99 Kumara, V.; Nadella, K.; Li, W. (2003) Production of thick microcellular thermoplastic sheets, SPE Antec, 1722-24.

100 Domininghas, H. (1993). Plastics for engineers: materials, properties, applications. Carl Hanser Verlag, New York, 265-280.

101 Manninnen, A.; Naguib, H.E.; Nawaby, A.V.; Day, M. (2005). CO_2 Sorption and Diffusion in Polymethyl Methacrylate-Clay Nanocomposites, Polymer Engineering and Science, 45, 7 , 904-914.

102 Kumar, V.; Weller, J. E. (1991). Microcellular polycarbonate-Part I: Experiments on bubble nucleation and growth, SPE Antec, 1401.

103 Wang, J.; Cheng, X.; Zheng, X.; Yuan, M.; He, J. (2003). Preparation and characterization of microcellular polystyrene/polystyrene ionomer blends with supercritical carbon dioxide, Journal of Polymer Science: Part B: Polymer Physics, 41, 4, 368-377

104 Gibson, L. J.; Ashby, M. F., (1999). Cellular Solid: Structure and Properties. Second Edition, Cambridge University Press, Cambridge

105 Fu, J.; Jo, C.; Naguib, H. E. (2005). The Effect of the Processing Parameters on Cellular Structures and Mechanical Properties of PMMA Microcellular Foams, Journal of Cellular Polymers, 24, 4, 177-195.

106 (1986). Standard test method for Impedance and Absorption of acoustical materials using a tube, two microphones and a digital frequency analysis system, ASTM E 1050-86

107 Garboczi, E.J.; Day, A.R. (1995). An algorithm for computing the effective linear elastic properties of heterogeneous materials: three-dimensional results for composites with equal phase Poisson ratios. J. Mech. Phys. Solids, 43, 1349–1362.

108 Poutet, J.; Manzoni, D.; Hage-chehade, F.; Jacquin, C.G.; Bouteca, M.J.; Thovert, J.F.; Adler, P.M. (1996). The effective mechanical properties of random porous media. J. Mech. Phys. Solids, 44, 1587–1620.

109 ADINA R & D, Inc., (2002). ADINA Theory and Modeling Guide

Appendices

Appendix A. Calculation of the Mass of the Material Charged in Rotational Mold Foaming

Polymer and CBAs were charged in the mold of the rotational mold foaming setup before processing. The amount of polymer and CBA depends on the desired expansion ratio φ, the volume of the mold V_m, the density of polymer ρ, and the gas evolution rate R. The density of the obtained foam can be given by:

$$\rho_f = \frac{\rho_p}{\varphi} \tag{10.1}$$

by assuming there is no empty space inside the sample after the processing, the mass of foam is given by:

$$m_f = \rho_f V_m \tag{10.2}$$

The mass of the foam is the sum of the mass of polymer and the mass of gas. Since the mass of gas is small and negligible, the mass of polymer is given by:

$$m_p = m_f - m_g \doteq m_f = \frac{V_m \rho_p}{\varphi} \tag{10.3}$$

The volume of gas that can be generated by CBA:

$$V_g = m_{cba} R \tag{10.4}$$

However, not all the gas can be used in foaming. Some of them escape out of the mold through the vent hole. By noting the percentage of the gas that can be contributed for

foaming is η, the volume of gas that can be used in foaming is:

$$V_g' = m_{cba} R\eta \tag{10.5}$$

The expansion ratio of foam is:

$$\phi = \frac{V_g' + V_p}{V_p} \tag{10.6}$$

where

$$V_p = \frac{m_p}{\rho_p} \tag{10.7}$$

Combing (10.5), (10.6) and (10.7), the minimum required CBA mass for φ times expansion is given by:

$$m_{cba} = \frac{(\varphi - 1) m_p}{R\eta\rho_p} \tag{10.8}$$

Equition (10.3) and (10.8) estimates the mass of polymer and CBA need to be charged in the mold. Experimental results showed these two equations give good estimations for the required material when the η was taken as 50%, which means that approximately half of the gas generated by the CBA was escaped out of the mold.

Appendix B. Mechanical Drawings for the Rotational Mold Foaming Setup

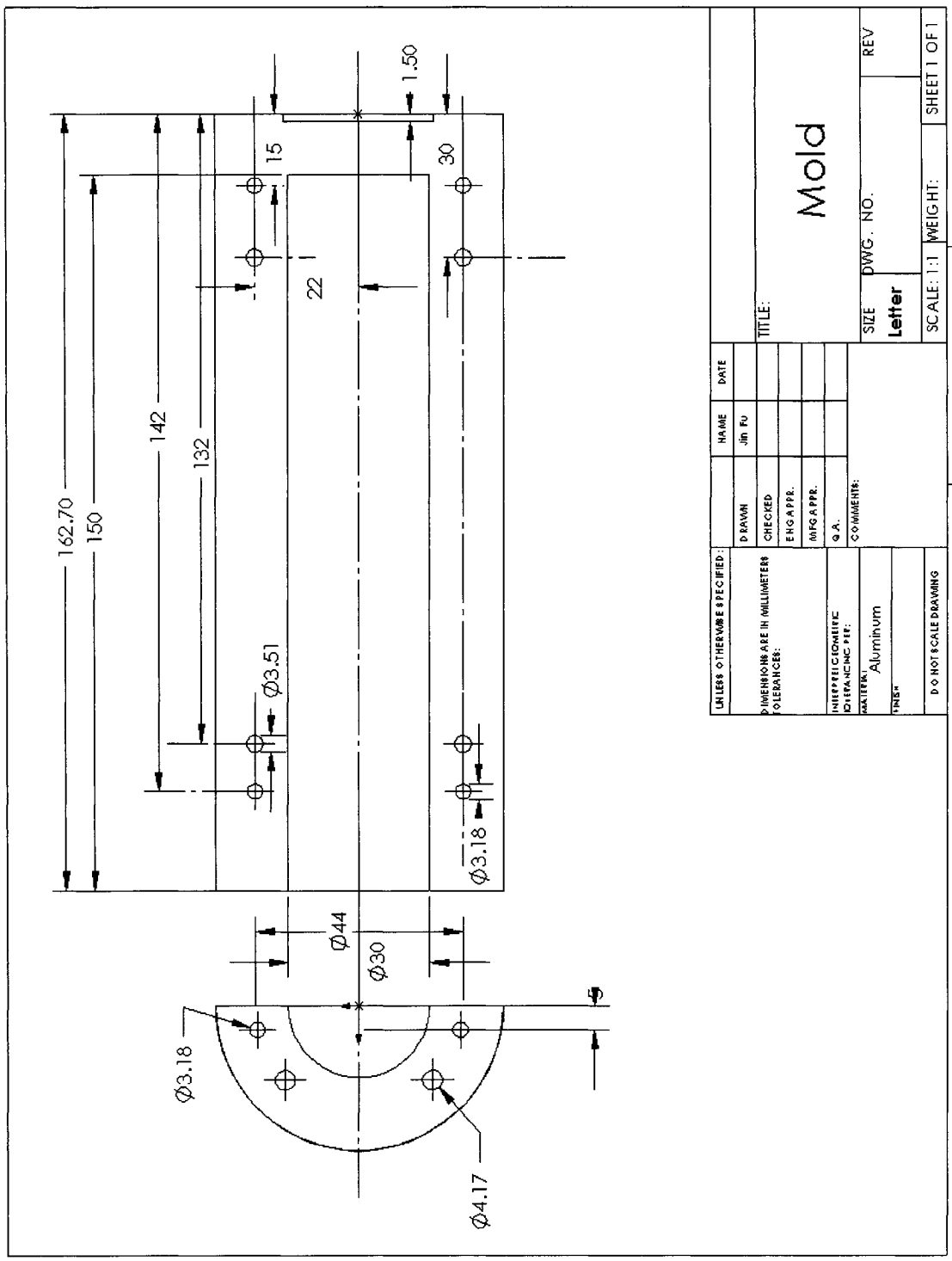
162.70
150
142
132
15
1.50
30
22
Ø3.51
Ø3.18
Ø44
Ø30
Ø3.18
Ø4.17
5
UNLESS OTHERWISE SPECIFIED:
DRAWN
CHECKED
ENG APPR.
MFG APPR.
Q.A.
COMMENTS:
NAME
Jin Fu
DATE
DIMENSIONS ARE IN MILLIMETERS
TOLERANCES:
INTERPRET GEOMETRIC TOLERANCING PER:
MATERIAL
Aluminum
FINISH
DO NOT SCALE DRAWING
TITLE:
Mold
SIZE
Letter
DWG. NO.
REV
SCALE: 1:1
WEIGHT:
SHEET 1 OF 1

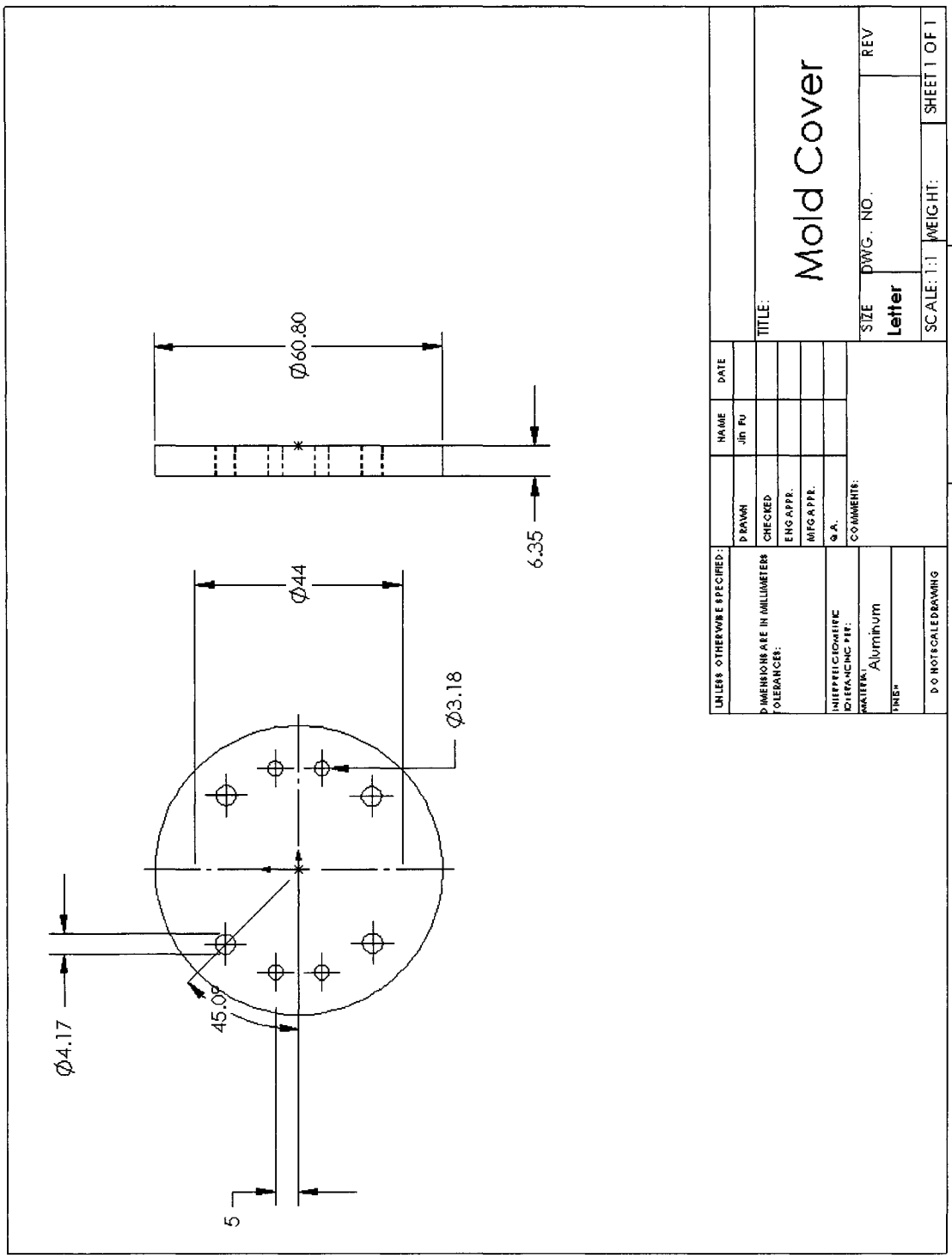
Ø60.80
6.35
Ø44
Ø3.18
Ø4.17
45.00
5
UNLESS OTHERWISE SPECIFIED:
DRAWN
Jin Pu
CHECKED
ENG APPR.
MFG APPR.
Q.A.
COMMENTS:
DIMENSIONS ARE IN MILLIMETERS
TOLERANCES:
INTERPRET GEOMETRIC
TOLERANCING PER:
MATERIAL
Aluminum
FINISH
DO NOT SCALE DRAWING
TITLE:
Mold Cover
SIZE
Letter
DWG. NO.
REV
SCALE: 1:1
WEIGHT:
SHEET 1 OF 1

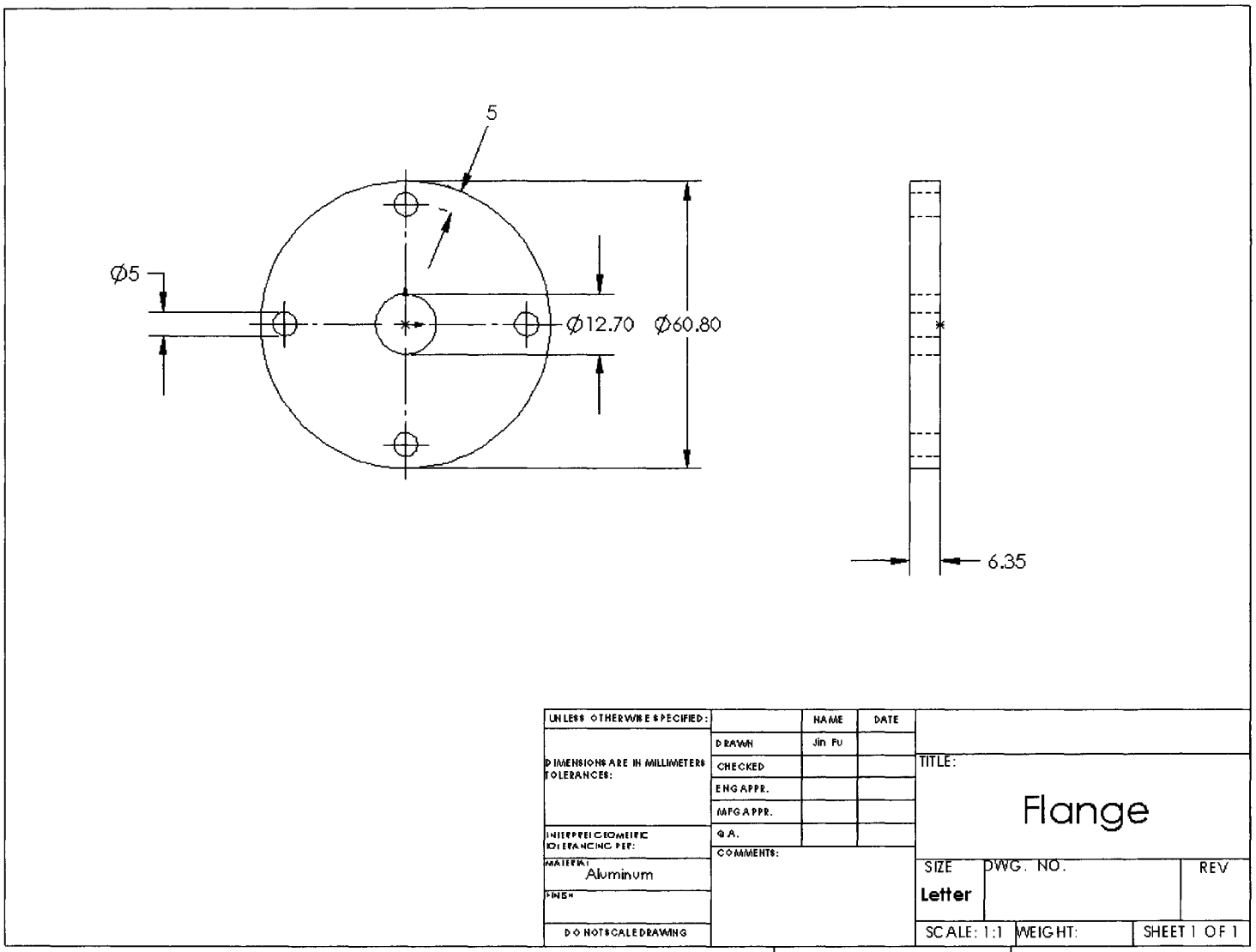
5
Ø5
Ø12.70
Ø60.80
6.35
UNLESS OTHERWISE SPECIFIED:
DIMENSIONS ARE IN MILLIMETERS
TOLERANCES:
INTERPRET GEOMETRIC TOLERANCING PER:
MATERIAL
Aluminum
FINISH
DO NOT SCALE DRAWING
NAME
DATE
DRAWN
Jin Fu
CHECKED
ENG APPR.
MFG APPR.
Q.A.
COMMENTS:
TITLE:
Flange
SIZE
Letter
DWG. NO.
REV
SCALE: 1:1
WEIGHT:
SHEET 1 OF 1
5
4
3
2
1

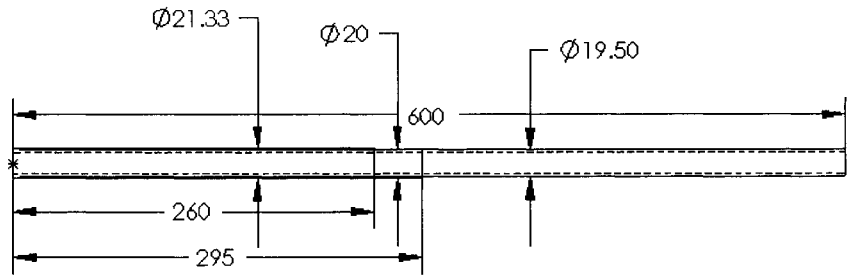

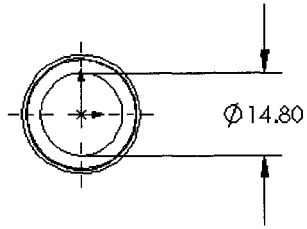

		NAME	DATE
UNLESS OTHERWISE SPECIFIED:			
DIMENSIONS ARE IN MILLIMETERS TOLERANCES:	DRAWN	Jin Fu	
	CHECKED		
	ENG APPR.		
	MFG APPR.		
INTERPRET GEOMETRIC TOLERANCING PER:	Q.A.		
MATERIAL Aluminum	COMMENTS: The scale of the cross section view is 1:1. The scale of the main view is 1:4.		
FINISH			
DO NOT SCALE DRAWING			

TITLE:

Hollow shaft

SIZE	DWG. NO.	REV
Letter		
SCALE: 1:1	WEIGHT:	SHEET 1 OF 1

5 4 3 2 1

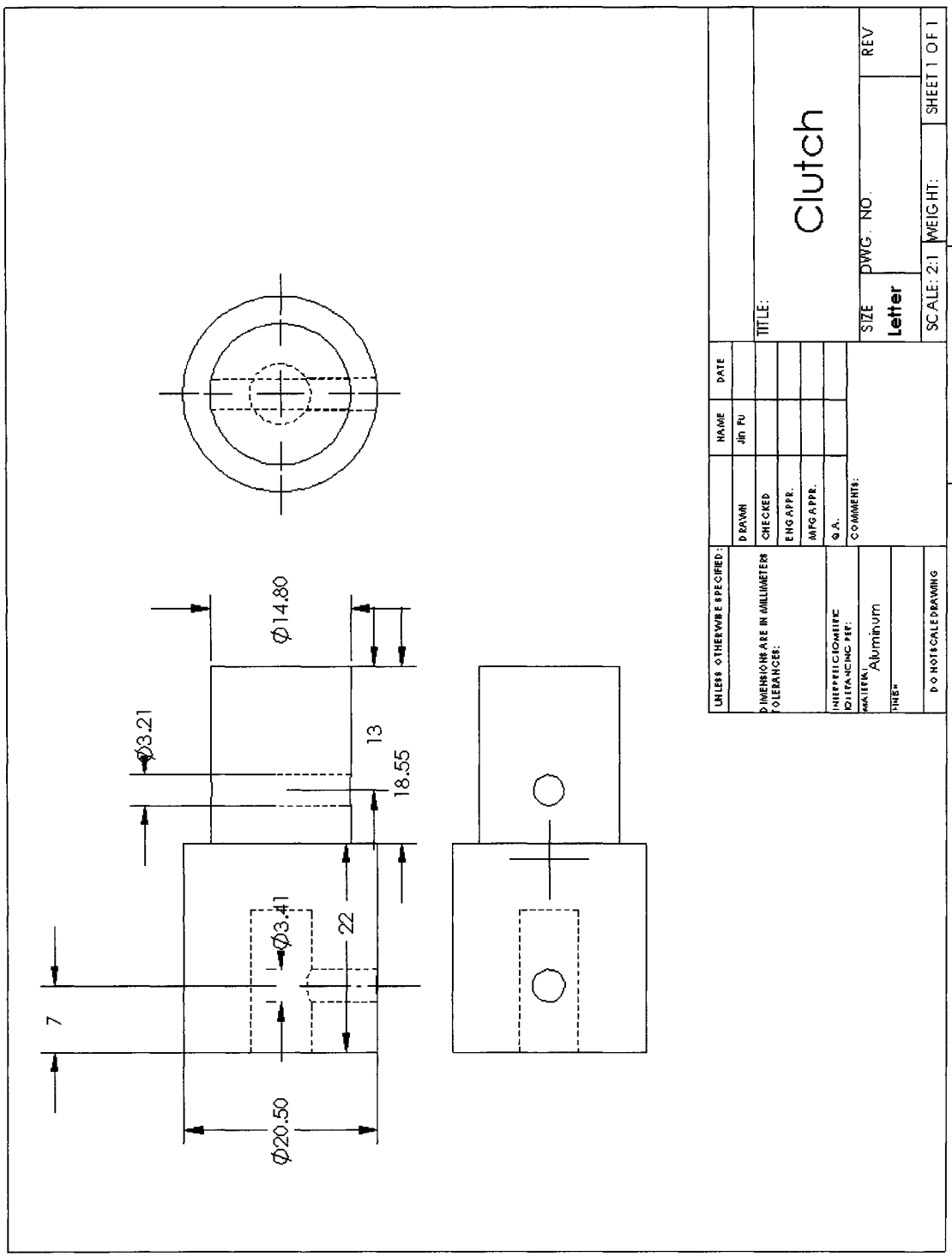
Clutch
Aluminum
Letter
SCALE: 2:1
SHEET 1 OF 1
Φ14.80
Φ3.21
Φ3.41
Φ20.50
13
18.55
22
7

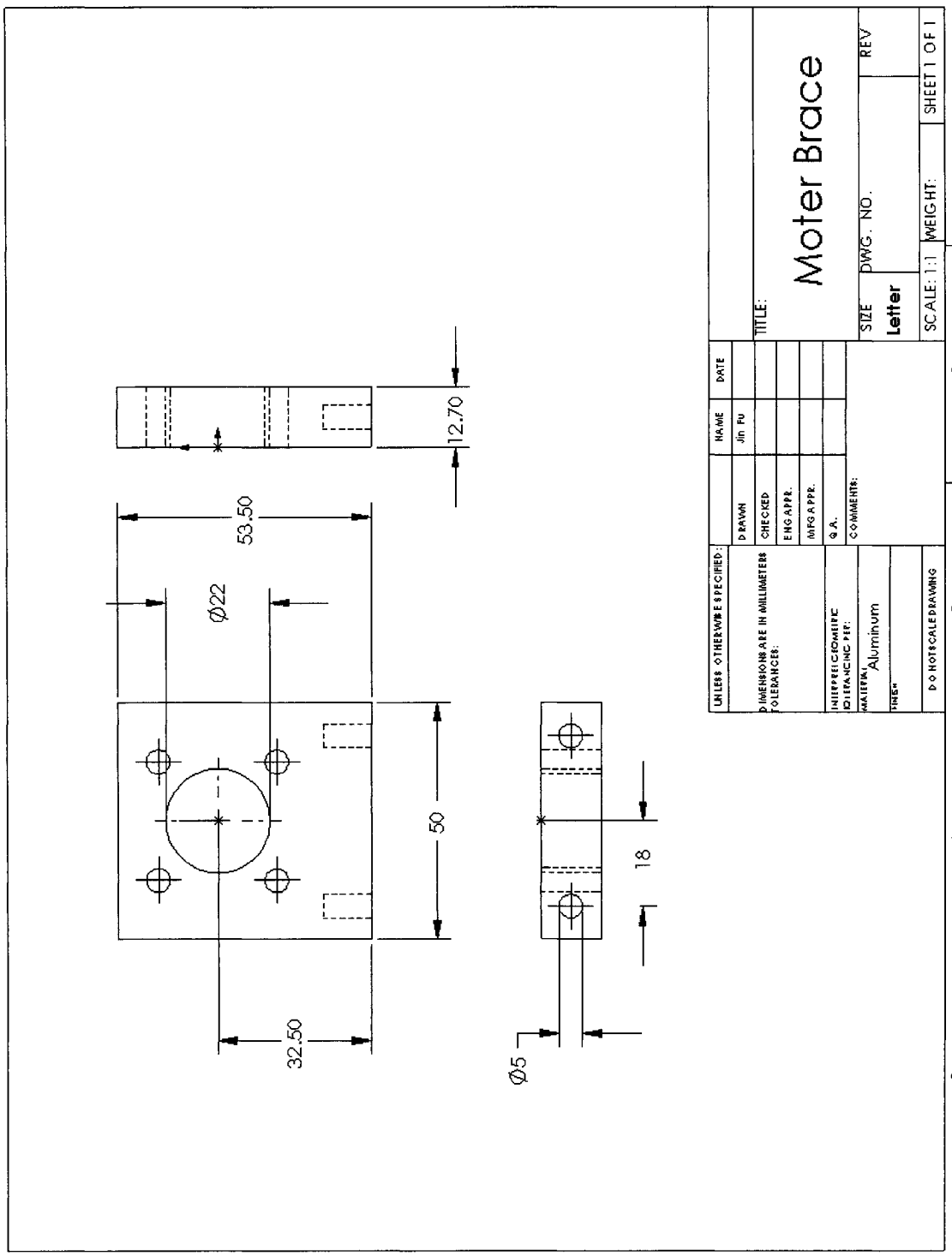
12.70
53.50
Ø22
50
32.50
Ø5
18
UNLESS OTHERWISE SPECIFIED:
DRAWN
CHECKED
ENG APPR.
MFG APPR.
Q.A.
COMMENTS:
NAME
Jin Fu
DATE
DIMENSIONS ARE IN MILLIMETERS
TOLERANCES:
INTERPRET GEOMETRIC TOLERANCING PER:
MATERIAL
Aluminum
FINISH
DO NOT SCALE DRAWING
TITLE:
Moter Brace
SIZE
Letter
DWG. NO.
REV
SCALE: 1:1
WEIGHT:
SHEET 1 OF 1

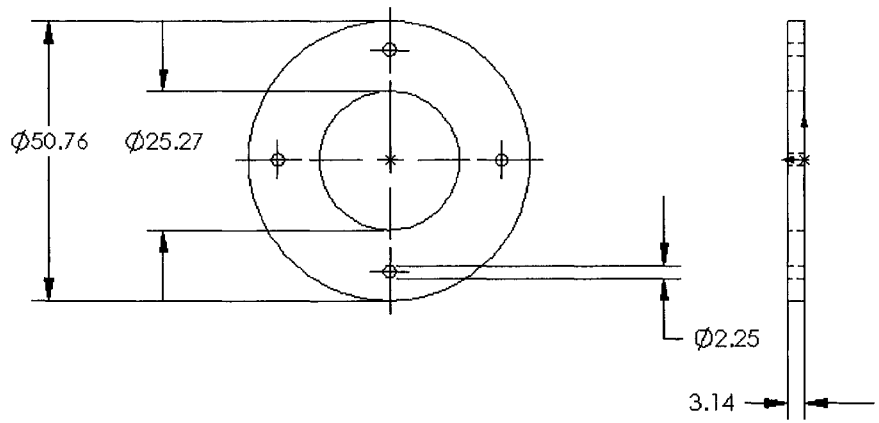

UNLESS OTHERWISE SPECIFIED:		NAME	DATE
DIMENSIONS ARE IN MILLIMETERS TOLERANCES:	DRAWN	Jin Fu	
	CHECKED		
	ENG APPR.		
	MFG APPR.		
INTERPRET GEOMETRIC TOLERANCING PER:	Q.A.		
MATERIAL Copper	COMMENTS:		
FINISH			
DO NOT SCALE DRAWING			

TITLE:

Metal Ring

SIZE	DWG. NO.	REV
Letter		
SCALE: 1:1	WEIGHT:	SHEET 1 OF 1

5 4 3 2 1

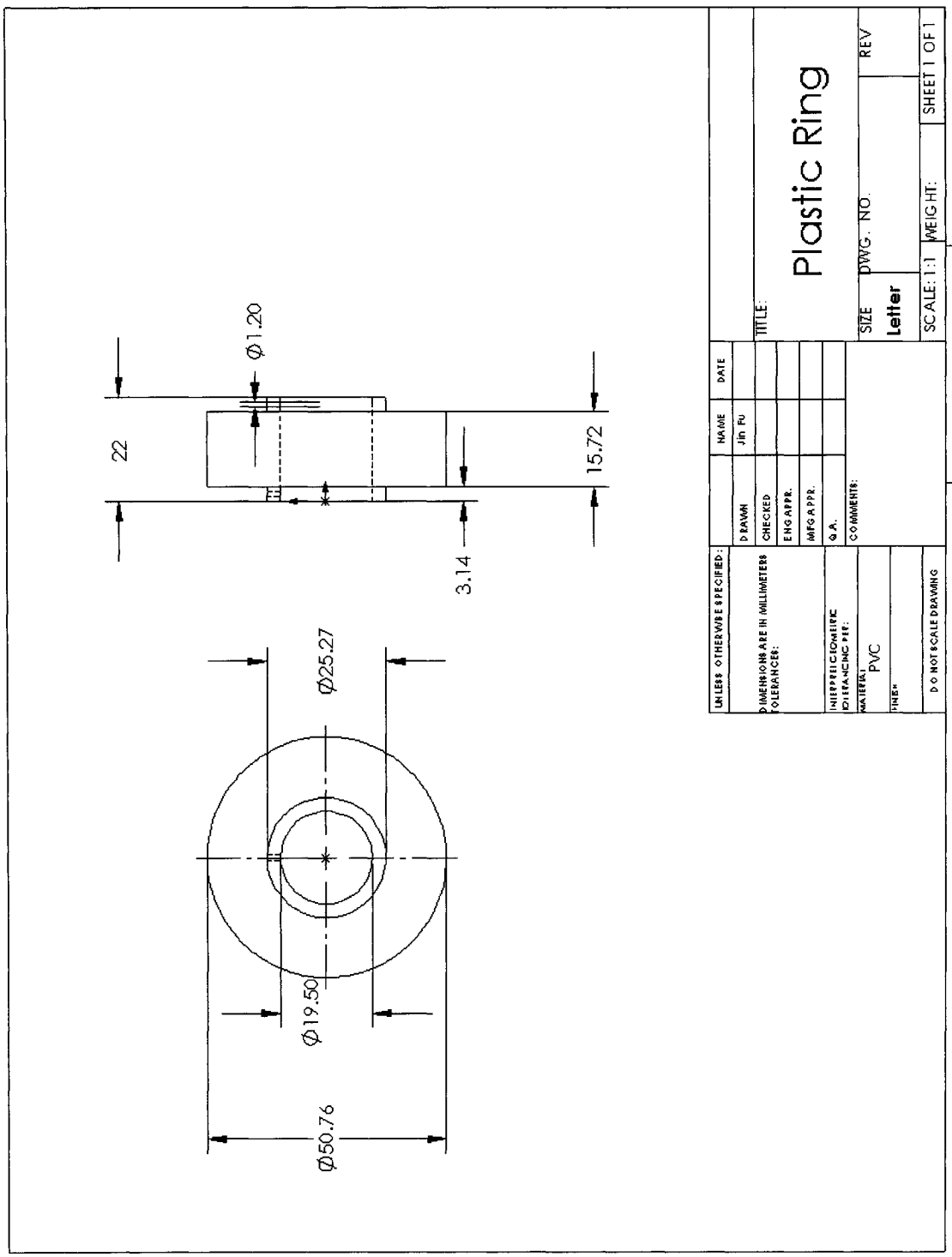
Ø1.20
22
15.72
3.14
Ø25.27
Ø19.50
Ø50.76
UNLESS OTHERWISE SPECIFIED:
DRAWN
CHECKED
ENG APPR.
MFG APPR.
Q.A.
COMMENTS:
NAME
Jin Fu
DATE
DIMENSIONS ARE IN MILLIMETERS
TOLERANCES:
INTERPRET GEOMETRIC
TOLERANCING PER:
MATERIAL
PVC
FINISH
DO NOT SCALE DRAWING
TITLE:
Plastic Ring
SIZE
Letter
DWG. NO.
REV
SCALE: 1:1
WEIGHT:
SHEET 1 OF 1

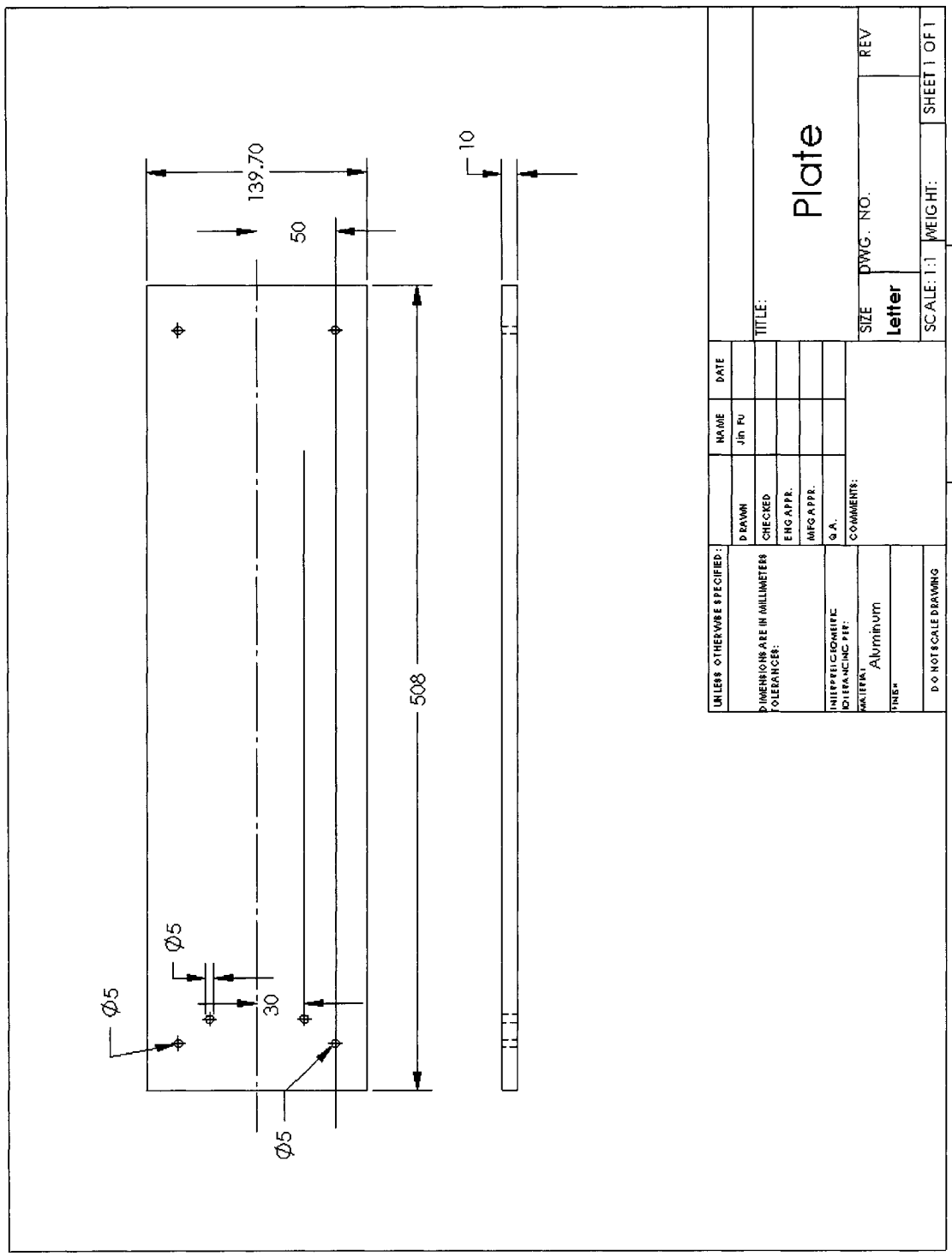
139.70
50
508
10
Ø5
Ø5
30
Ø5
UNLESS OTHERWISE SPECIFIED:
DRAWN
CHECKED
ENG APPR.
MFG APPR.
Q.A.
COMMENTS:
NAME
Jin Fu
DATE
DIMENSIONS ARE IN MILLIMETERS
TOLERANCES:
INTERPRET GEOMETRIC
TOLERANCING PER:
MATERIAL
Aluminum
FINISH
DO NOT SCALE DRAWING
TITLE:
Plate
SIZE
Letter
DWG. NO.
REV
SCALE: 1:1
WEIGHT:
SHEET 1 OF 1
1
2
3
4
5

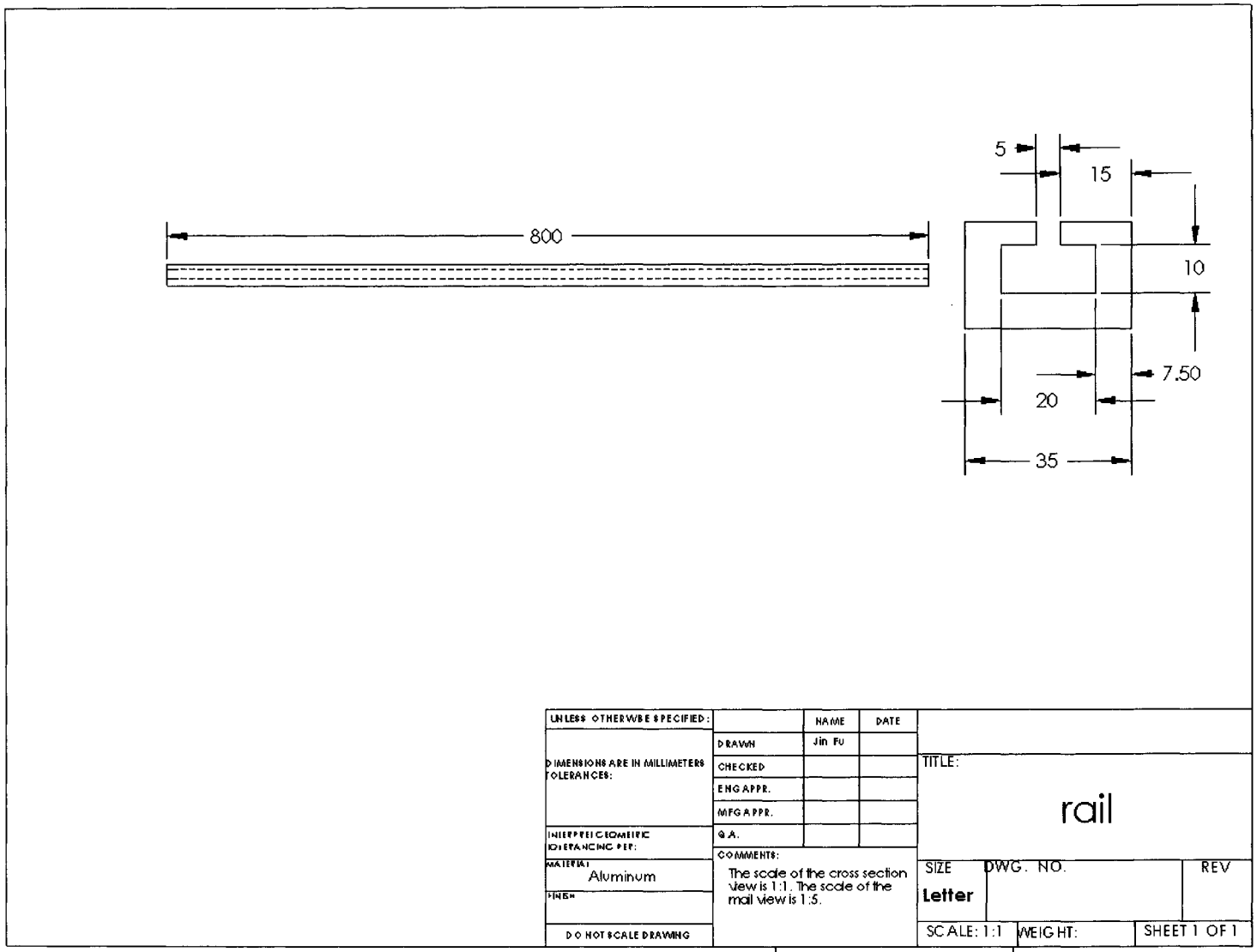

		NAME	DATE
UNLESS OTHERWISE SPECIFIED:			
DIMENSIONS ARE IN MILLIMETERS TOLERANCES:	DRAWN	Jin Fu	
	CHECKED		
	ENG APPR.		
	MFG APPR.		
INTERPRET GEOMETRIC TOLERANCING PER:	Q.A.		
MATERIAL Aluminum	COMMENTS: The scale of the cross section view is 1:1. The scale of the rail view is 1:5.		
FINISH			
DO NOT SCALE DRAWING			

TITLE:

rail

SIZE	DWG. NO.	REV
Letter		
SCALE: 1:1	WEIGHT:	SHEET 1 OF 1

5 4 3 2 1

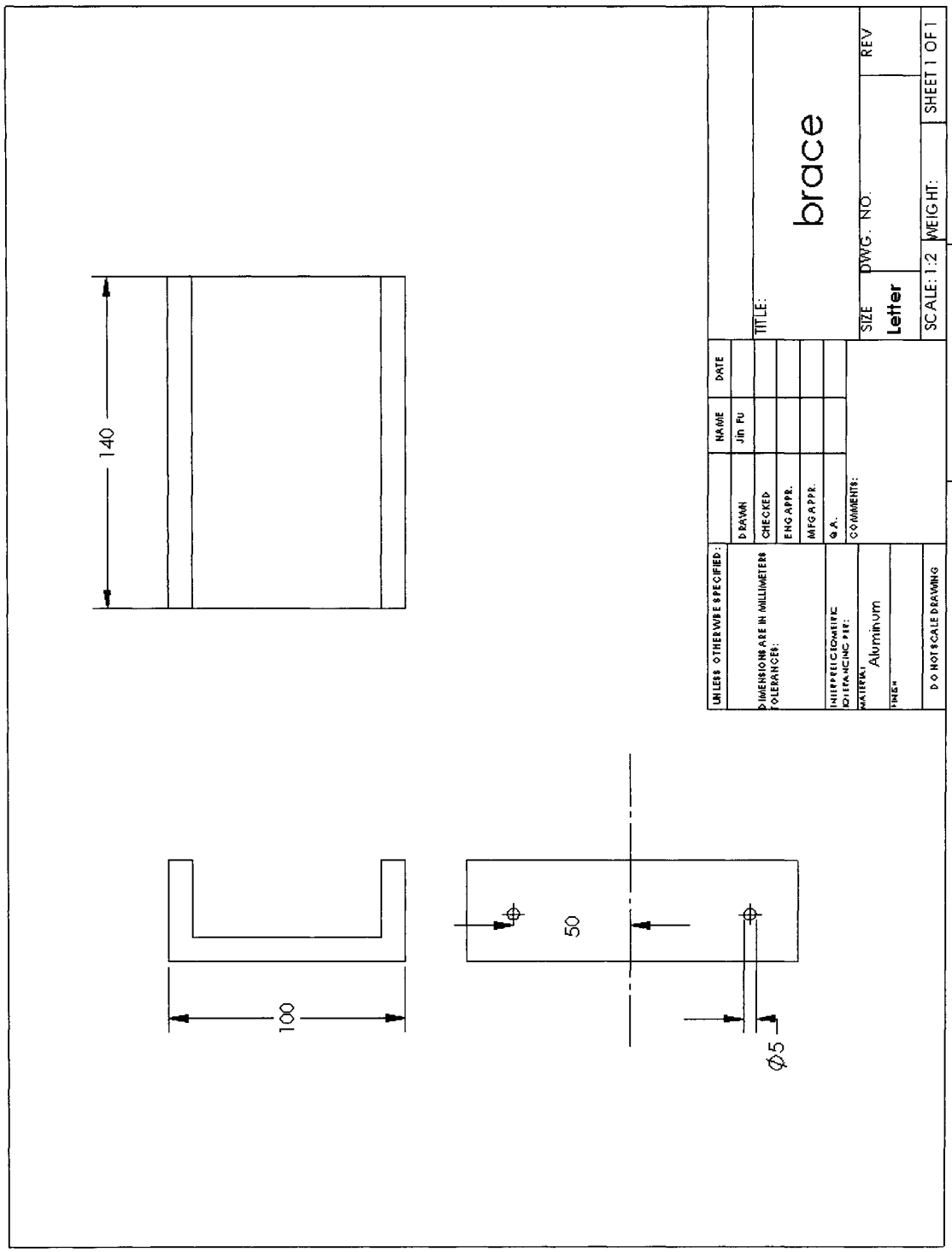
140
100
50
Ø5
UNLESS OTHERWISE SPECIFIED:
DIMENSIONS ARE IN MILLIMETERS
TOLERANCES:
INTERPRET GEOMETRIC
TOLERANCING PER:
MATERIAL
Aluminum
FINISH
DO NOT SCALE DRAWING
DRAWN
CHECKED
ENG APPR.
MFG APPR.
Q.A.
COMMENTS:
NAME
Jin Fu
DATE
TITLE:
brace
SIZE
Letter
DWG. NO.
REV
SCALE: 1:2
WEIGHT:
SHEET 1 OF 1
1
2
3
4
5